DISSERTATION

INVESTIGATION INTO THE MECHANISMS OF SIZE-RESOLVED PARTICLE DRY DEPOSITION ACROSS THREE ENVIRONMENTS

Submitted by

Erin Kathleen Boedicker

Department of Chemistry

In partial fulfillment of the requirements

For the Degree of Doctor of Philosophy

Colorado State University

Fort Collins, Colorado

Summer 2022

Doctoral Committee:

Advisor: Delphine Farmer

A.R. Ravi Ravishankara
John Volckens
Megan Willis

ABSTRACT

INVESTIGATION INTO THE MECHANISMS OF SIZE-RESOLVED PARTICLE DRY DEPOSITION ACROSS THREE ENVIRONMENTS

Airborne particulate matter, or aerosols, have significant impacts on radiative forcing through both their direct - scattering and absorbing light - and indirect effects- acting as cloud condensation nuclei and altering the lifetime of clouds. The magnitude of these effects is largely determined by particle lifetime, which is defined by their rate of removal through wet and dry deposition. Dry deposition, specifically of accumulation mode aerosols (0.1 – 1 μ), is one of the largest sources of uncertainty in global models. The processes that influence deposition are poorly constrained and few comprehensive measurements are available to improve our understanding. Characterizing these mechanisms is vital for predicting spatial and temporal trends in particle dry deposition and lifetime. While there have been improvements in quantifying and understanding dry deposition, large gaps in our knowledge still exist that make predicting the impacts of aerosols on Earth's climate difficult.

To improve understanding of the underlying mechanisms that determine the rate of particle deposition in an environment this dissertation reports size-resolved dry deposition measurements from three distinct environment types. First, we report measurements from a test house which identify dilution and deposition as the most important factors influencing particle concentrations indoors. This analysis also shows that deposition indoor is governed by the same fundamental process that we consider for outdoor environments. Second, we present particle flux and deposition measurements from a Ponderosa pine forest over four seasons where significant enhancement in deposition during the wintertime was observed. This is attributable to changes in interception, caused by changes in plant physiology and

surface structure during the winter that leads to an increase in their ability to uptake particles. Finally, we show particle and black carbon deposition from a low Arctic tundra during snow-cover that are elevated compared to predictions of dry deposition in that region. Incorporating interception into the model parameterizations improved model measurement agreement and provides evidence to suggest that surface structure and microroughness impact deposition even when there is snow-cover.

AKNOWLEDGEMENTS

Throughout my time in graduate school I have received support and encouragement from an amazing group of people. I'd like to thank my mother, Laurie Boedicker, who made science special to me and who gave me all the skills and discipline I needed to pursue this degree. I'd also like to thank my sisters, Sarah, Lauren, and Rachel. Whose friendship has been invaluable, and who have always been there for me (even if I didn't want to talk about HAM Radio). I thank my mother's partner, Roger Saffle, who has taught me so much and who has been an amazing role model. Additionally, I'd like the thank the friends I have made here in the department. You all have made an amazing and supportive community that I don't know what I would have done without. I thank the Farmer Group for being an amazing group of colleagues and friends. We thank the entire HOMEChem science team, including Drs. Atila Novoselac and Steve Bourne for operating the UTest House. We thank Steve Alton of the US Forest Service and the National Center for Atmospheric Research for field site support during SPiFFFY. We thank Fred Helsel, Justin LaPierre, Ross Burgener, Valerie Sparks, and Jimmy and Josh Ivanoff for field site support during ArcticBCADS. Finally, I want to thank my mentor Dr. Delphine Farmer for teaching me how to be a good scientist.

DEDICATION

To my mother Laurie Boedicker, and sisters Sarah, Lauren, and Rachel

Thank you for everything

TABLE OF CONTENTS

INTRODUCTION - DRY DEPOSITION OF ATMOSPHERIC AEROSOLS[1]

Importance Of Particle Dry Deposition

Aerosols, or airborne particulate matter, are the strongest drivers of uncertainties in understanding radiative forcing and climate feedback loops.[1,2] These particles affect climate both directly, by scattering and absorbing radiation, and indirectly, by acting as condensation nuclei (CCN) and affecting the radiative properties of clouds. Scattering has a cooling effect in the atmosphere, the extent of which depends on particle size, while absorption leads to warming of the atmosphere if the particle composition has adequate chromophores, typically through 'brown' and 'black' carbon. Cloud droplets scatter light and enhance the albedo of the planet, and anthropogenic particles tend to enhance the albedo of clouds. These direct and indirect aerosol effects are poorly quantified, and result in the largest uncertainties in model predictions of Earth's climate.[3] The physical size and chemical properties of atmospheric aerosol particles determine the extent of these effects and therefore define their potential to influence the radiative balance of the planet. These properties are not static: atmospheric chemistry can change the chemical and physical properties of aerosol particles. Gas-particle partitioning, coagulation with other particles, and chemical reactions on particle surfaces can all enable changes in composition and chemical properties, including hygroscopicity, volatility, and viscosity. All the different ways that aerosol affects climate, however, depend on their concentrations, which in turn depend strongly on their removal rates. Thus, while these aerosol–cloud–radiation interactions are complex, it is the removal of these particles from the atmosphere that represents the single largest uncertainty in climate.[4,5]

Particles are removed from the atmosphere through wet and dry deposition, both of which are typically considered true sinks in the troposphere (**Figure 0.1**). Dry deposition refers to the removal

[1] Farmer, D. K.; Boedicker, E. K.; DeBolt, H. M. Dry Deposition of Atmospheric Aerosols: Approaches, Observations, and Mechanisms. *Annu. Rev. Phys. Chem.* **2021**. https://doi.org/10.1146/annurev-physchem-090519-034936.

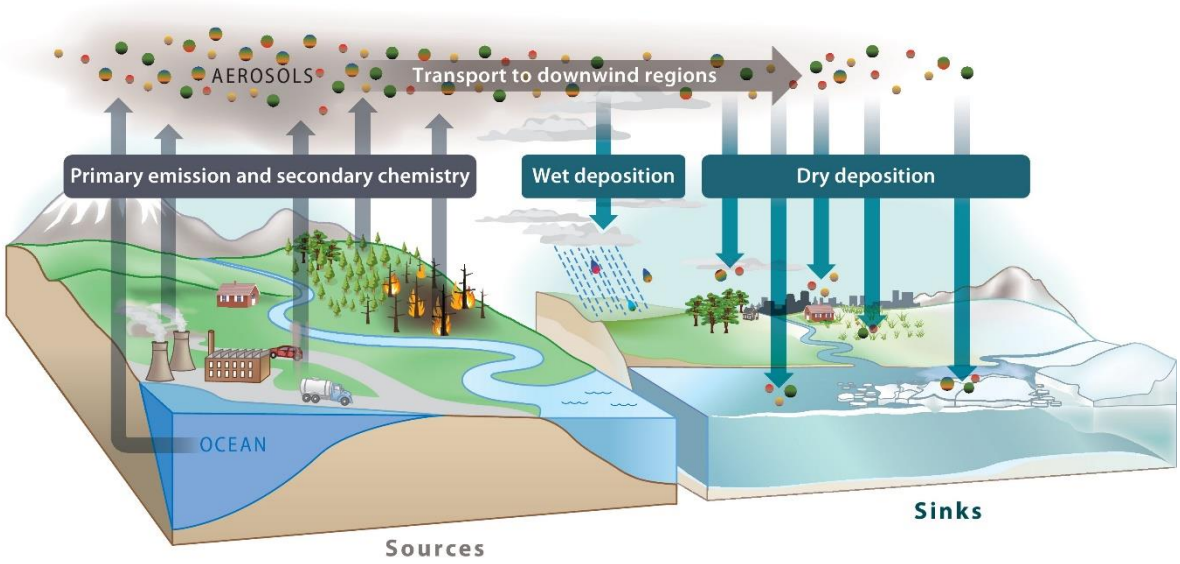

Figure 0.1: Primary emissions and secondary chemistry are key sources of aerosols in the atmosphere. Wet and dry deposition remove particles, determining the lifetime of these aerosols in the atmosphere. Deposition surfaces include forests, grasslands, ice, water, and urban environments, with each surface type removing particles at different size- and turbulence-dependent rates.

of particles by collision with terrestrial or hydrological surfaces by gravitational settling, impaction, interception and/or diffusion (**Figure 0.2**). Wet deposition refers to the scavenging of particles from the atmosphere by solid or liquid water and subsequent removal by precipitation. One nuance in this definition of wet deposition is that cloud droplets can subsequently evaporate and release the particles back into the atmosphere, albeit after potentially substantial aqueous chemical processing. As a result of wet and dry deposition, the lifetime of submicron particles is typically considered about a week in the atmosphere - long enough for intercontinental transport. On a global scale, this lifetime is dominated by wet deposition, but dry deposition is an important lever on aerosol lifetime in the absence of precipitation.

There are serious problems with our current understanding of deposition rates: Current parameterizations are inaccurate[6–11]; measurements are scarce; and, as expected, the rates are very important. For example, Goldstein & Galbally (2007) estimated that wet deposition of secondary organic aerosols (one type of aerosol) was about four times that of dry deposition, but that the uncertainties in organic aerosol lifetimes due to deposition were substantial.[12] As the atmospheric relevance of aerosol-phase reactions, at the surface of or within the aerosol, is often assessed by a comparison of reaction rates versus aerosol lifetimes, this uncertainty in deposition rates also impacts the way we think about aerosol chemical reactivity. The relative importance of these dry deposition processes depends on particle size, with gravitational settling significantly impacting larger (i.e., >10 μm in diameter) particles and diffusion being the main driver for smaller (<300 nm) particles, even though both processes act on all particle sizes.[13] Dry deposition is typically described by the concentration (C) of the species of interest and a deposition velocity, V_{dep}:

$$\text{Deposition Flux} = -V_{dep} \times C \tag{0.1}$$

Deposition velocity is expressed as a rate; for submicron aerosol particles, V_{dep} is typically on the order of 0.1 cm s^{-1}. A downward flux, or deposition, is taken as a negative flux by convention, while an upward or emitting flux is positive. V_{dep} provides a particularly useful metric for comparing results across sites - and

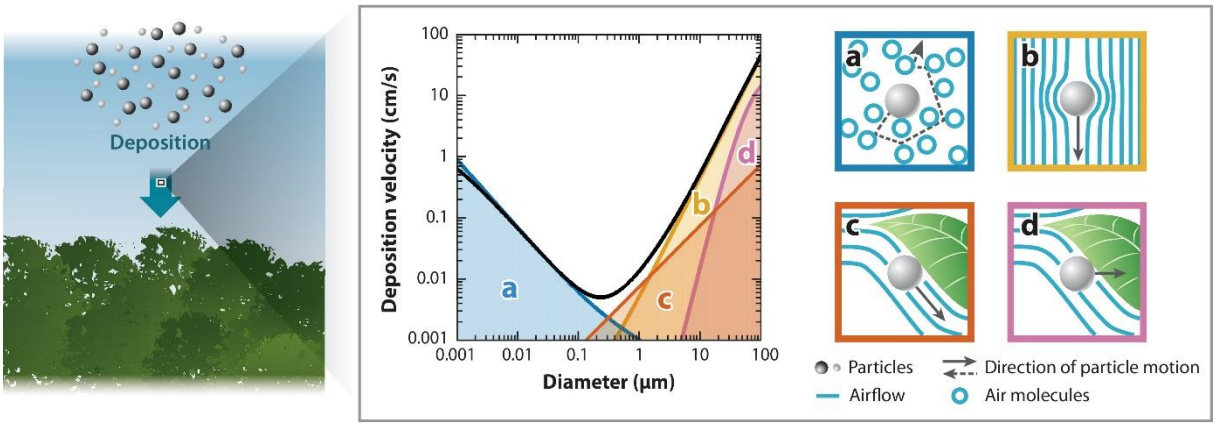

Figure 0.2: Dry deposition velocities of particles are a function of particle diameter and are driven by a combination of processes, including (a) Brownian diffusion (blue), (b) gravitational settling (yellow), (c) interception (orange), and (d) impaction (purple). The relative importance of these processes varies with particle size and surface type, with the graph providing an example of these processes and the total calculated deposition velocity (thick black line) for a conifer forest. The direction of airflow in panels a–d is indicated by solid blue lines; the direction of particle motion is indicated by gray arrows. In the case of Brownian diffusion, particle movement is random, as indicated by the dashed gray arrow. The size of particles relative to gases is not drawn to scale.

for modeling particle removal - because it is independent of ambient concentration. Observation techniques typically measure the flux and concentration of particles and derive the V_{dep}. However, dry deposition is challenging to measure because most measurement techniques rely on micrometeorological techniques, which require careful site selection and either vertical gradients in concentration (difficult to achieve as differences in actual concentration may be on par with or smaller than differences in inlet losses) or particularly fast, sensitive, and selective detectors for eddy covariance (EC) flux measurements. While there are many reasons for the uncertainty in the aerosol impact on climate, they fundamentally stem from our ability to represent the processes that shape the size and concentration of particles in the atmosphere, including aerosol sources and sinks. Lee et al. (2013) found uncertainty in dry deposition velocities of particles in the accumulation mode to be the largest contributor to uncertainty in cloud condensation nuclei (CCN) concentration in global models, which is critical to understanding cloud interactions.[5] CCN are the particles to which water vapor condenses in the atmosphere and form cloud droplets and are typically sub-micron in diameter, but the deposition rates of larger particles are also relevant to climate processes - including dust (100 nm to 100 µm in size). Similarly, Carslaw et al. (2013) found dry deposition of accumulation mode particles to be the largest contributor to uncertainties in the cloud albedo aerosol indirect effect.[2] The results of Carslaw et al. (2013) and Lee et al. (2013) strongly emphasize the need for increased certainty in accumulation mode aerosol dry deposition rates.

Observations of Particle Deposition

There are few recent measurements of aerosol flux, and thus V_{dep} observations, over vegetated surfaces. This lack of observations is primarily due to the challenges inherent in obtaining aerosol flux measurements. We have compiled an extensive list of dry deposition particle measurements, including the studies that report deposition velocities, that have been plotted in **Figure 0.3** to provide a clear visual representation of gaps in our observations. **Figure 0.3** highlights the lack of measurements over the cryosphere and that the bulk of size-resolved particle flux measurements have been collected in the accumulation mode.

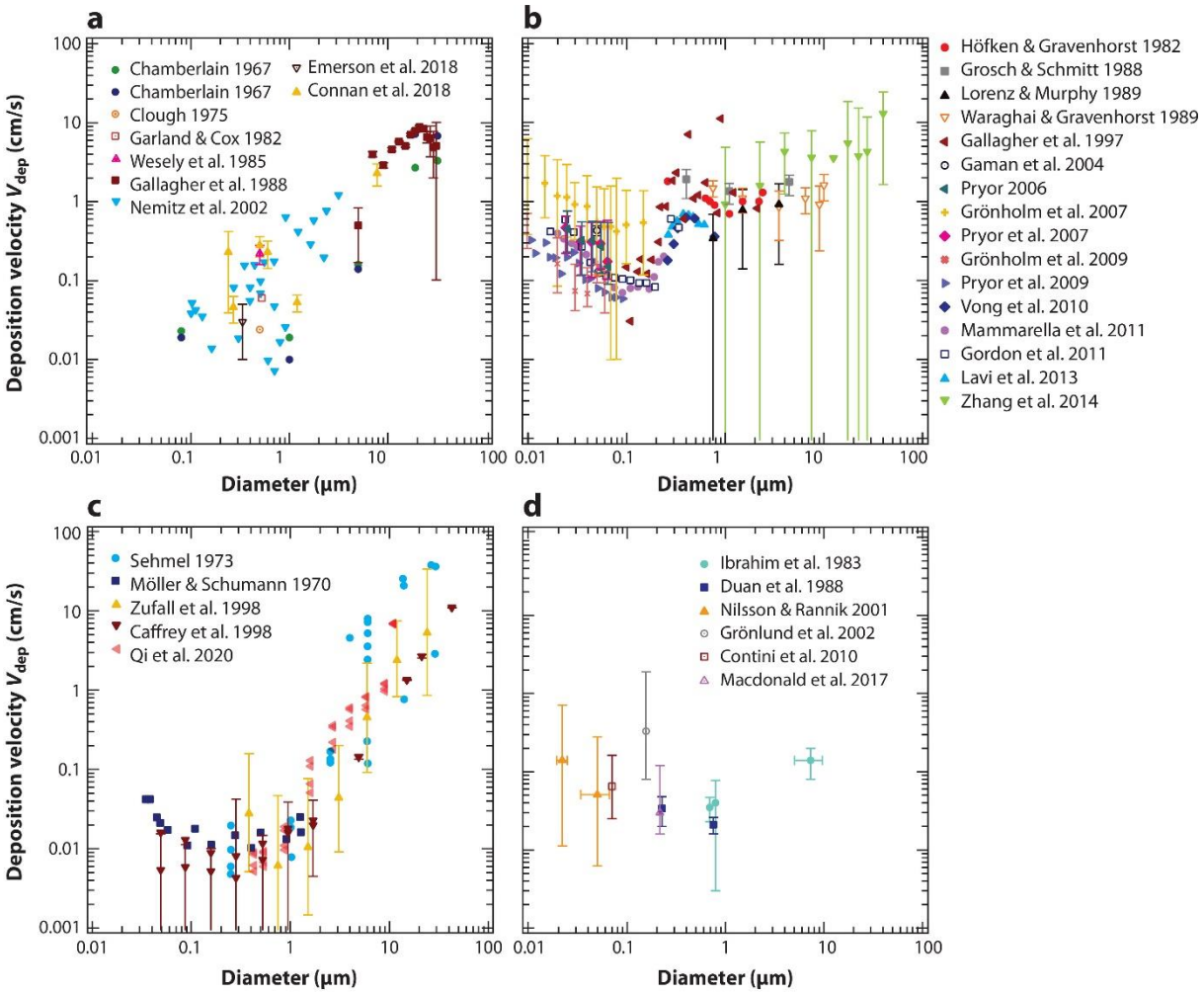

Figure 0.3: Graphs showing compiled multiple size–resolved particle flux observations of deposition velocity as a function of size over (a) grasslands, (b) forests, (c) water surfaces, and (d) the cryosphere. These data sets are not normalized for friction velocity (u*), which has been established to strongly influence flux.

Size is clearly a key controlling variable in particle dry deposition.[11,14,15] Particle are often treated as perfect spheres, however, they can be irregular in shape. This could alter deposition, but the influence of shape is currently not well understood or accounted for. Small particles are more strongly influenced by deposition processes driven by Brownian diffusion, while larger particles are more strongly influenced by interception, impaction, and gravitational settling (**Figure 0.2**). As a result of these competing processes, deposition velocity typically exhibits a minimum in the accumulation mode. This minimum occurs because uptake to surface collectors due to Brownian diffusion decreases as size increases, while removal by gravitational settling increases with size. The roles of surface uptake due to impaction and interception processes also increase with size, though models suggest a drop-off at the very large (i.e., tens of microns in diameter) size range. The importance of these processes are also impacted by particle density, which is accounted for using a bulk density. Of course, the relevance of different aerosol modes or size ranges depends on the question being posed; small particles are typically greater in number but can be less important in terms of mass exchange.

Deposition velocities are clearly a function of turbulence (typically described by friction velocity, u*), with more turbulent conditions inducing a stronger flux.[8,16–18] Land use type also influences deposition velocity, with more complex ecosystems with greater surface area holding more collectors and enabling more deposition through interception. Hence, deposition velocities over forests are typically greater than those over grasslands, which are in turn greater than those over lakes or smooth aquatic surfaces. At larger particle sizes (>10 μm in diameter), gravitational settling plays a controlling role, and deposition rates tend to converge independent of surface structure.

Investigating Particle Deposition in This Work

This work focuses on trends in size-resolved deposition velocities across three very different environments: a test house, a Ponderosa pine forest, and a low arctic tundra. Throughout all the work, dry deposition is investigated along with other processes happening in the environment of interest, so as to critically examine the role and underlying mechanisms of dry deposition. First, particle lifetime in indoor

environments is examined using cooking data from the House Observations of Microbial and Environmental Chemistry (HOMEChem) campaign. Particle sinks including dry deposition are characterized, and their impact on observed spatial gradients in concentration indoors is determined. Second, this work explores the seasonal variation of size-resolved particle dry deposition in a Ponderosa pine forest using data from the Seasonal Particles in Forests Flux studY (SPiFFY). The underlying mechanisms of dry deposition are discussed, and additional mechanisms are investigated to determine which contribute to the observed increase in deposition during the winter. Finally, measurements from the Arctic Black Carbon and Aerosol Deposition Study (Arctic BCADS) are presented and used to critically evaluate the treatment of snow-covered surfaces as flat surfaces in current dry deposition models.

INTRODUCTION REFERENCES

(1) IPCC. Climate Change 2013 - The Physical Science Basis, 2013.

(2) Carslaw, K. S.; Lee, L. A.; Reddington, C. L.; Pringle, K. J.; Rap, A.; Forster, P. M.; Mann, G. W.; Spracklen, D. V.; Woodhouse, M. T.; Regayre, L. A.; Pierce, J. R. Large Contribution of Natural Aerosols to Uncertainty in Indirect Forcing. *Nature* **2013**, *503* (7474), 67–71. https://doi.org/10.1038/nature12674.

(3) Fowler, D.; Pilegaard, K.; Sutton, M. A.; Ambus, P.; Raivonen, M.; Duyzer, J.; Simpson, D.; Fagerli, H.; Fuzzi, S.; Schjoerring, J. K.; Granier, C.; Neftel, A.; Isaksen, I. S. A.; Laj, P.; Maione, M.; Monks, P. S.; Burkhardt, J.; Daemmgen, U.; Neirynck, J.; Personne, E.; Wichink-Kruit, R.; Butterbach-Bahl, K.; Flechard, C.; Tuovinen, J. P.; Coyle, M.; Gerosa, G.; Loubet, B.; Altimir, N.; Gruenhage, L.; Ammann, C.; Cieslik, S.; Paoletti, E.; Mikkelsen, T. N.; Ro-Poulsen, H.; Cellier, P.; Cape, J. N.; Horváth, L.; Loreto, F.; Niinemets, Ü.; Palmer, P. I.; Rinne, J.; Misztal, P.; Nemitz, E.; Nilsson, D.; Pryor, S.; Gallagher, M. W.; Vesala, T.; Skiba, U.; Brüggemann, N.; Zechmeister-Boltenstern, S.; Williams, J.; O'Dowd, C.; Facchini, M. C.; de Leeuw, G.; Flossman, A.; Chaumerliac, N.; Erisman, J. W. Atmospheric Composition Change: Ecosystems–Atmosphere Interactions. *Atmospheric Environment* **2009**, *43* (33), 5193–5267. https://doi.org/10.1016/j.atmosenv.2009.07.068.

(4) Lee, L. A.; Carslaw, K. S.; Pringle, K. J.; Mann, G. W. Mapping the Uncertainty in Global CCN Using Emulation. *Atmospheric Chemistry and Physics* **2012**, *12* (20), 9739–9751. https://doi.org/10.5194/acp-12-9739-2012.

(5) Lee, L. A.; Pringle, K. J.; Reddington, C. L.; Mann, G. W.; Stier, P.; Spracklen, D. V.; Pierce, J. R.; Carslaw, K. S. The Magnitude and Causes of Uncertainty in Global Model Simulations of Cloud Condensation Nuclei. *Atmospheric Chemistry and Physics* **2013**, *13* (17), 8879–8914. https://doi.org/10.5194/acp-13-8879-2013.

(6) Pryor, S. C.; Barthelmie, R. J.; Hornsby, K. E. Size-Resolved Particle Fluxes and Vertical Gradients over and in a Sparse Pine Forest. *Aerosol Science and Technology* **2013**, *47* (11), 1248–1257. https://doi.org/10.1080/02786826.2013.831974.

(7) Pryor, S. C.; Barthelmie, R. J.; Spaulding, A. M.; Larsen, S. E.; Petroff, A. Size-Resolved Fluxes of Sub-100-Nm Particles over Forests. *Journal of Geophysical Research: Atmospheres* **2009**, *114* (D18). https://doi.org/10.1029/2009JD012248.
(8) Vong, R. J.; Vong, I. J.; Vickers, D.; Covert, D. S. Size-Dependent Aerosol Deposition Velocities during BEARPEX'07. *Atmospheric Chemistry and Physics* **2010**, *10* (12), 5749–5758. https://doi.org/10.5194/acp-10-5749-2010.
(9) Petroff, A.; Murphy, J. G.; Thomas, S. C.; Geddes, J. A. Size-Resolved Aerosol Fluxes above a Temperate Broadleaf Forest. *Atmospheric Environment* **2018**, *190*, 359–375. https://doi.org/10.1016/j.atmosenv.2018.07.012.
(10) Saylor, R. D.; Baker, B. D.; Lee, P.; Tong, D.; Pan, L.; Hicks, B. B. The Particle Dry Deposition Component of Total Deposition from Air Quality Models: Right, Wrong or Uncertain? *Tellus B: Chemical and Physical Meteorology* **2019**, *71* (1), 1550324. https://doi.org/10.1080/16000889.2018.1550324.
(11) Emerson, E. W.; Hodshire, A. L.; DeBolt, H. M.; Bilsback, K. R.; Pierce, J. R.; McMeeking, G. R.; Farmer, D. K. Revisiting Particle Dry Deposition and Its Role in Radiative Effect Estimates. *PNAS* **2020**. https://doi.org/10.1073/pnas.2014761117.
(12) Goldstein, A. H.; Galbally, I. E. Known and Unexplored Organic Constituents in the Earth's Atmosphere. *Environ. Sci. Technol.* **2007**, *41* (5), 1514–1521. https://doi.org/10.1021/es072476p.
(13) Slinn, W. G. N. Predictions for Particle Deposition to Vegetative Canopies. *Atmospheric Environment (1967)* **1982**, *16* (7), 1785–1794. https://doi.org/10.1016/0004-6981(82)90271-2.
(14) Petroff, A.; Mailliat, A.; Amielh, M.; Anselmet, F. Aerosol Dry Deposition on Vegetative Canopies. Part I: Review of Present Knowledge. *Atmospheric Environment* **2008**, *42* (16), 3625–3653. https://doi.org/10.1016/j.atmosenv.2007.09.043.
(15) Petroff, A.; Mailliat, A.; Amielh, M.; Anselmet, F. Aerosol Dry Deposition on Vegetative Canopies. Part II: A New Modelling Approach and Applications. *Atmospheric Environment* **2008**, *42* (16), 3654–3683. https://doi.org/10.1016/j.atmosenv.2007.12.060.
(16) Ahlm, L.; Krejci, R.; Nilsson, E. D.; Mårtensson, E. M.; Vogt, M.; Artaxo, P. Emission and Dry Deposition of Accumulation Mode Particles in the Amazon Basin. *Atmospheric Chemistry and Physics* **2010**, *10* (21), 10237–10253. https://doi.org/10.5194/acp-10-10237-2010.
(17) Sievering, H. Small-Particle Dry Deposition under High Wind Speed Conditions: Eddy Flux Measurements at the Boulder Atmospheric Observatory. *Atmospheric Environment (1967)* **1987**, *21* (10), 2179–2185. https://doi.org/10.1016/0004-6981(87)90350-7.
(18) GröNholm, T.; Aalto, P. P.; Hiltunen, V. J.; Rannik, Ül.; Rinne, J.; Laakso, L.; HyvöNen, S.; Vesala, T.; Kulmala, M. Measurements of Aerosol Particle Dry Deposition Velocity Using the Relaxed Eddy Accumulation Technique. *Tellus B: Chemical and Physical Meteorology* **2007**, *59* (3), 381–386. https://doi.org/10.1111/j.1600-0889.2007.00268.x.

CHAPTER 1 - FATES AND SPATIAL VARIATIONS OF ACCUMULATION MODE PARTICLES IN A MULTI-ZONE INDOOR ENVIRONMENT DURING THE HOMECHEM CAMPAIGN[2]

Chapter Overview

Studying the indoor dynamics that impact particles is crucial in order to understand indoor air chemistry and assess overall human exposure to particles. This work investigates spatial gradients in particle concentration, caused by indoor transport and loss mechanisms. We conducted a variety of cooking experiments during the House Observations of Microbial and Environmental Chemistry (HOMEChem) campaign in June 2018 that allowed us to probe these mechanisms. We measured size-resolved (0.06 – 1 μm and 0.13 – 3 μm) particle number concentrations from cooking experiments using optical instruments at four locations throughout the house simultaneously. The particle number concentration in the kitchen was 40 ± 10 % and 70 ± 10 % higher than the concentrations in the living room and the bedroom, respectively. There was a minor size dependence, with larger differences in the smaller sizes of the accumulation mode (0.1 – 2.5 μm) than the larger end of the range. Dilution accounts for the majority of these concentration differences. Surface deposition was the dominant fate of particles within a zone, with observed deposition velocities ranging from 0.1 to 0.6 m h^{-1}.

Introduction

Annually, ambient air pollution accounts for approximately 3.7 – 4.8 million deaths globally.[1] One important pollutant that contributes to air quality is particulate matter. Particles have been shown to have a significant impact on health and are a major cause of cardiovascular and respiratory disease.[2–4] Particles present in the built environment contribute substantially to overall exposure,[5] as people spend more time indoors than outside. In the US alone, people spend an average of 80 - 90% of their time

[2] Boedicker, E. K.; Emerson, E. W.; McMeeking, G. R.; Patel, S.; Vance, M. E.; Farmer, D. K. Fates and Spatial Variations of Accumulation Mode Particles in a Multi-Zone Indoor Environment during the HOMEChem Campaign. *Environ. Sci.: Processes Impacts* **2021**, 23 (7), 1029–1039. https://doi.org/10.1039/D1EM00087J.

indoors.[6] The impact of particles on human health is a function of their concentration, size, and composition, which are influenced by emission sources, a variety of dynamic processes (e.g. deposition, coagulation, and gas-to-particle partitioning), and building mechanics (e.g. natural and mechanical ventilation, infiltration air exchange, filtration, envelope penetration, and interzonal transport).[7–11] In order to better understand the full effect of indoor environments (relative to outdoor environments) on human exposure to particles, a quantitative description of the sources and sinks, including transport and deposition, of indoor particles is essential.

Indoor sources of particles include gas stoves,[12] printers,[13,14] 3D printers,[15,16] cigarette smoke,[17] and human activity (e.g. walking)[18] which have been well quantified elsewhere. Cooking is a dominant source of particle indoors and mainly contributes to ultrafine (<100 nm) and fine (100 nm – 2.5 μm) mode particles.[12,19,20] After emission, particles can deposit onto surfaces in the building and ventilation system, coagulate to form fewer but larger particles, and undergo gas-particle partitioning where particles are transformed when individual compounds evaporate off or condense onto particles.[7] In addition, particles can be transported from room to room within indoor environments and potentially outdoors.[7] Transport away from particle sources induces spatial gradients within buildings, which are influenced by building mechanics, environmental conditions such as temperature and humidity, and size-dependent particle losses.

While several models have been proposed for predicting particle spatial gradients,[21–25] there have been few comprehensive measurements of these gradients in occupied houses. The first studies to explore spatial variation indoors focused on overall concentration differences between rooms (zones) within a building. Ju and Spengler (1981) measured 24-hr averages of respirable particles in four homes in Boston, MA, and observed significant zonal differences in half the homes. Multi-zone experiments done by Miller and Nazaroff (2001) on environmental tobacco smoke using time- and size-resolved measurements in a two-room facility observed a 14 – 97% drop in particle mass concentration across zones after emission events. The magnitude of this difference was dependent on ventilation and zone segregation conditions:

increasing ventilation resulted in a 57 – 83% difference while segregating the two zones resulted in a 97% difference in particle mass. Other studies have since expanded on these observations including zonal differences in trace gas species[28–30]. However, most previous research on multi-zone systems has utilized simple two-zone environments, unoccupied houses, or has been limited in the number of size-resolved measurement points. Quantifying indoor spatial gradients of particles, both in terms of concentration and size, is necessary to accurately characterize and minimize human exposure to indoor particle sources and gain insight into particle chemistry occurring throughout an indoor environment.

The objective of this work was to critically analyze particle gradients observed in a test house during cooking events using several optical particle measurements. In order to fully characterize the fates of accumulation mode particles indoors, we looked at particle production during cooking, particle transportation through the house, and major loss mechanisms between and within different zones. Data presented here were collected as part of the House Observations of Microbial and Environmental Chemistry (HOMEChem) study, a month-long indoor chemistry campaign conducted in the UTest House at the University of Texas at Austin.[31]

Methods

Experimental overview

The HOMEChem campaign took place from 1 to 30 June 2018.[31] HOMEChem included a comprehensive suite of chemical and physical measurements that monitored both particle and gas-phase species during cooking, cleaning, and occupancy activities. The campaign utilized the UTest House at the University of Texas at Austin (Austin, TX, USA); a 3-bedroom, 2-bath house with a total house volume of 250 m^3 and a total floor area of 111 m^2. This analysis separated the house into three main zones: the kitchen, living room. and bedroom (**Figure 1.1**).

The outdoor air-change rate (*ACR*) of the house was maintained at 0.5 ± 0.1 h^{-1} by positively pressurizing the house relative to the outdoor environment when both of the two doors and all nine

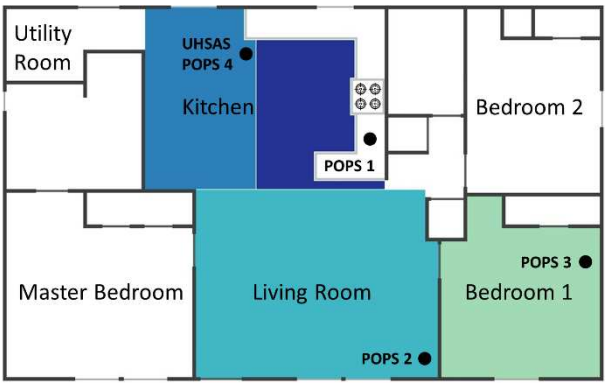

Figure 1.1: Floor plan of the UTest house. Black dots and labels indicate instrument sampling positions. Colors for the different zones on this plot indicate how the data in this paper will be organized, with the darkest color being the measurement closest to the source (kitchen) and the lightest color being the furthest from the sources (bedroom 1). The kitchen is considered a single zone in this analysis but has two colors to represent the two different instruments and sampling points within the zone.

windows were closed. This minimized variations in temperature and humidity around the house. During the campaign, the electric air handling unit with overhead air diffusers was operated continuously with a recirculation flow rate of 8 h^{-1} (2000 m^3 h^{-1}). Filters on the outdoor air supply and internal ducts were removed during the campaign, to ensure results were not affected by the filter condtions[9,10], and no stove exhaust hood was used during the study. The air conditioning (AC) system was set to 25°C throughout the campaign, except during designated venting periods. The AC system also provided dehumidification when cooling. Indoor temperature was 25 ± 2°C and indoor relative humidity was 57 ± 6% on experimental days. Outdoor temperature and reliative humidity were 29 ± 4°C and 71 ± 17% respectively throughout the campaign. Further details about the ventilation system employed during the campaign are described elsewhere.[31]

In order to investigate interzonal transport and deposition of particles indoors the cooking experiments from the HOMEChem campaign were investigated. Cooking experiments during HOMEChem included a total of sixteen vegetable stir-fry experiments, six breakfast experiments, three chili experiments, ten toast experiments, and two full typical U.S. Thanksgiving meals. Further details of the campaign set-up and experimental schedule are described elsewhere [31].

Instrumentation

Size-resolved particle concentrations were measured using an Ultra-High Sensitivity Aerosol Spectrometer (UHSAS, model UHSAS-G; DMT Inc., Longmont, CO),[32] which was calibrated regularly throughout the campaign using NIST standard polystyrene latex spheres (60 – 900 nm mobility diameter). We ran daily filters on the UHSAS to monitor instrument background and ensure that there were no internal leaks. The UHSAS was set to have 1 second resolution and count particles in 99 size bins between 0.06 and 1 µm by directing a solid-state laser (1054 nm) at the sample air flow and quantifying the resulting particle size-dependent scatter. Indoor air was sampled through an 8 m copper sampling line (ID: 6.35 mm) and outdoor air was sampled through a separate 4.8 m copper line (ID: 6.35 mm). Both lines connected to a 1.5 m segment of stainless-steel tubing (ID: 6.35 mm) attached to the valve switching

system that included a HEPA bypass system for running blanks and a Nafion dryer (MD700, Perma Pure LLC, Lakewood, NJ) which all normal sampling ran through. The UHSAS sampled at 50 mL/min off the line, which had a total flow of ~ 6 L/min (Re ≈ 1300; residence time of 3 s in the main line). Line losses calculated using the method described by Weiden et al. (2009) were negligible for the measured size range (< 5%).[33] Throughout the campaign the UHSAS typically switched at regular intervals between indoor (25 min) and outdoor sampling (5 min).

We simultaneously measured particle size distributions in four locations within the test house using four Portable Optical Particle Spectrometers (POPS; Handix Scientific LLC, Boulder, CO).[34] These instruments measure particles ranging from 0.13 to 3 µm using a 405 nm laser diode, and collected a size distribution every second. Both the UHSAS and the POPS correlate light scatter to particle size following Mie theory. The four POPS were placed in the kitchen, living room, and one of the three bedrooms of the test house (**Figure 1.1**), as well as in an external trailer to monitor outdoor conditions. The POPS had a 1.0 cm long stainless-steel inlet nozzle (ID: 0.81 mm) as an inlet housed in a stainless-steel tube (ID: 1.75 mm). The flow rate through the inlet was set to 180 mL/min. Particles were not actively dried like the UHSAS line was with the Nafion dryer, but sample flow was mixed with a filtered sheath flow which likely reduced the RH near particles.

Optical instruments have limitations on the magnitude of particle concentrations they can measure and can be biased because of differences in the composition of particles used for calibration and the particles measured. To address these limitations, we preformed saturation analysis and compared the optical measurements to a scanning mobility particle sizer (SMPS, TSI Inc., Shoreview, MN) that was present during the campaign. The intercomparisons of the optical instruments with the SMPS show good agreement between the average measured distributions in the size ranges used for analysis, validating the use of these instruments for the size dependent analysis presented here. Total concentration was underestimated compared to the SMPS indicating that further corrections would need to be applied (i.e. refractive index, saturation, etc.) if this data was being used to characterize cooking emissions, however,

that is outside the scope of this work. Data presented herein utilizes the full size range of all instruments except during instances where total concentrations are compared across the two instruments. Additionally, periods where saturation had a significant effect on the UHSAS measurements – saturation was not observed in the POPS measurements - were removed from the analysis. In cases of saturation, only data for the unaffected size bins of the UHSAS are presented. A detailed description of all instrument intercomparisons, saturation analysis, and data treatment, can be found in the supplemental (**Appendix 1S**).

Calculation of Deposition Velocity

We derived the rate of deposition from the total particle concentration loss rate after the termination of cooking events using the general method described by Thatcher and Layton (1995)**.**[35] However, in these measurements we omit the initial decay period from the calculation of the particle loss rate to account for the impact of dilution. The initial decay period ends when the house becomes well-mixed, at which point we assume exfiltration – controlled by the *ACR* of the house – and deposition are the major sinks of particles. Deposition within the ductwork was neglected because of the small size of the particles and the high recirculation rate. We assume particle removal by filtration within the recirculation ducts was zero due to the absence of filters. However, the impact of recirculation on turbulence characteristics and deposition is poorly understood and may warrant future study. The house was assumed to be well-mixed at the point when POPS concentration data from around the house converged on each other. We determine loss rate due to deposition loss as well as loss due to exfiltration using a linear fit to the natural log of the decay for the period after the cooking event had been terminated – the stove was turned off - and the house had achieved a well-mixed state. The deposition loss rate (λ_d) was calculated:

$$\lambda_d = \left(\frac{1}{\Delta t}\right)\ln\left(\frac{C_0}{C}\right) - ACR \qquad (1.1)$$

where Δt is the time change between the initial and final concentration, C_0 is the initial concentration (particles·cm^{-3}) at the start of the decay period when the house was well-mixed, C is the concentration (particles·cm^{-3}) at the end of the decay. Deposition velocity, v_d (m·h^{-1}), was derived using an approximate volume (V, m^3) to area (A, m^2) ratio:

$$v_d = \left(\frac{V}{A}\right)\lambda_d \quad (1.2)$$

We derived the volume-to-surface-area ratio to be 0.47 from the room geometry of bedroom 1 where a POPS was located. It was the only zone monitored that had well-defined boundaries that could be used to constrain this ratio. Using this geometry, the surface-area-to-volume ratio was determined to be 2.1, consistent with the findings of Manuja et al. (2019) who found this ratio to be 2.0 ± 0.2 for bedrooms when the contents of the room were not considered and 3.0 ± 0.4 when the contents were included.[36] While bedroom 1 was unfurnished, we acknowledge that additional objects or people could alter these ratios and this is discussed in the deposition modeling section. The application of the bedroom's volume-to-surface-area ratio to all the measurements is justified by the fact that the observed trend in deposition loss rate was consistent across the different zones of the house and the zones were similarly unfurnished.

Deposition Models

Two models were compared to the experimentally determined deposition velocities. The first was the indoor deposition model developed by Lai and Nazaroff (2000).[37] This model estimates total deposition using the surface-area-to-volume ratio of the indoor space and the deposition velocities for different indoor surfaces (i.e. floors, ceilings, and walls) (**Appendix 1S**).

The second model used was an outdoor resistance model developed by Emerson et al. (2020), which is a modification of the Zhang et al. (2001) model (**Appendix 1S**).[38,39] This model was originally designed to apply to outdoor environments, such as forests or grasslands, and breaks down deposition into contributions from Brownian diffusion, gravitational settling, impaction, and interception to total

deposition velocity. The land use category and seasonal select category for a needleleaf forest in the midsummer were used to represent the indoor environment. These parameters determine the characteristic radius of the collectors (2 mm) and the roughness length (0.8 m). An air speed typical for an indoor environment (v = 0.1 m/s) was applied, and the measurement height (z_r) was set to the UHSAS inlet height (~1.5 meters). Other model parameters are described in the supplemental (**Appendix 1S**).

For both models a particle density of 1 g cm^{-3} was used based on evidence described in Patel et al. (2020) suggesting this as an appropriate density for cooking particles. Friction velocities (u_*), which are velocity measurements representing the shear stress between flows, ranging from 0.01 to 0.03 m s^{-1} are considered reasonable for an indoor environment. Several friction velocities were applied to both models, ranging from 0.01 to 1 m s^{-1}, in order to determine the best fits to the data.

Spatial Gradient and Dilution Calculations

The concentration gradient was calculated using the average size-dependent concentrations for the cooking event during the cooking period – defined by an experimental log as the time when the stove was turned on to the time the stove was turned off. The percent difference was calculated as the change in the other zones compared to the kitchen values. Time off-sets between when enhancement was observed in the different zones was not used shift the data. The size-dependent percent differences for all the cooking events were averaged and we present the median for all the cooking events.

We assumed each zone to be well-mixed. The measured kitchen particle concentration was taken to be representative of the entire kitchen volume (~40 m^3). The kitchen particle concentration was diluted into the adjoining spaces: the utility room (~9 m^3) and living room (~52 m^3). This method was also used to estimate the particle concentration in the bedroom by diluting the measured living room particle concentration into its adjoining spaces: the master bedroom (~36 m^3) and bedroom 1 (~28 m^3). These calculations do not include the volume from closed spaces (i.e. bathrooms and closet spaces) and the hallway space in the dilution volume. These spaces can be neglected since their collective volume only

produced a 3-5% change in the predicted distribution when included. This method neglects the impact of dilution and repartitioning of semi-volatile particles.

Results and Discussion

Cooking particles were used to investigate interzonal transport and deposition indoors; however, the results herein are not differentiated by the cooking method. Analysis of different cooking sources indoors is outside the scope of this work but is well documented by Patel et al. (2020). Background conditions, such as particle concentration and indoor-to-outdoor concentration ratios, as well as some source observations, are described in the supplemental (**Appendix 1S**).

Sinks for Indoor Particles

Accumulation mode particles throughout the house had loss rates ranging from 0.66 to 1.95 h^{-1}, which encompass the losses due to surface deposition and exfiltration. Concentration decay was size-dependent with the slowest decay corresponding to particles around 200 nm. Loss rates did not vary substantially for accumulation mode particles across cooking type or between zones. This indicates that in the context of this work, cooking data from our measured size range can be treated similarly regardless of cooking method when determining major sinks for particles indoors (**Appendix 1S**). We evaluate possible sinks for accumulation mode particles using direct observations and theoretical calculations. We evaluate different sink contributions to the net loss and explore the factors controlling these sinks.

Deposition is one of the dominant processes that drives particle loss indoors. The deposition trends observed during the cooking emission experiments were size dependent with particles around 200 nm in the accumulation mode depositing least efficiently due to less influence from the mechanisms driving deposition (**Figure 1S.13**)[40]. These data are consistent with previous studies that examined size-resolved deposition indoors for accumulation mode particles[41–45]. Deposition measurements made by Tian et al. (2020) for deposition of supermicron particles during the HOMEChem campaign seamed together

well with our observations and are used here to present a more meaningful analysis of the mechanisms controlling deposition [46].

In order to understand the intricacies of deposition of particles in indoor environments, we probed different mechanisms controlling deposition using two models. First, the widely-used indoor deposition model developed by Lai & Nazaroff (2000) is useful for understanding the particle contribution to deposited films on surfaces.[37] However, this model did not accurately capture the observed deposition at HOMEChem (**Figure 1.2a**). To better constrain this model, we investigated the impact of both the friction velocity term and the surface-area-to-volume ratio. A friction velocity (u_*) of 1 cm s^{-1} resulted in a 98.7 ± 0.5 % underestimation of deposition. The model only agreed with deposition velocities measured for particles less than 200 nm, when a u_* of 100 cm s^{-1} was used (**Figure 1S.15**). Large u_* values have previously been used with this model to enable reasonable fits with observed data,[41] although most literature suggests that reasonable u_* values for indoor environments are in the range of 1 – 3 cm s^{-1}.[37] Even with the larger u_* the model underrepresented deposition rates by up to 82 % (10 ± 20 % on average) in the accumulation mode and 86 ± 6 % on average in the coarse mode (**Figure 1S.14**). In order to constrain the surface-area-to-volume ratio used in the model, the ratio was varied according to Manuja et al. (2019).[36] Based on this analysis, the surface-area-to-volume ratio could be used to fine tune the model approximation; however, modifying this ratio did not significantly change the agreement between the model and observed deposition rates (**Figure 1S.16**). This analysis also agrees with the findings of Thatcher et al. (2002) (**Figure 1S.17**), where even in a more realistic fully furnished room the Lai and Nazaroff (2000) model underrepresented particle deposition for particles smaller than 0.5 µm by an order of magnitude[43].

The second model we used (**Figure** 1.**2b**) was the outdoor resistance model of Emerson et al. (2020), which is based on the framework of Slinn and Zhang.[39,47] The Emerson model places emphasis on interception as an efficient collector of aerosols, and is thus appropriate for deposition to irregular, non-horizontal surfaces. The outdoor model agreed well with the measured deposition velocities, with an

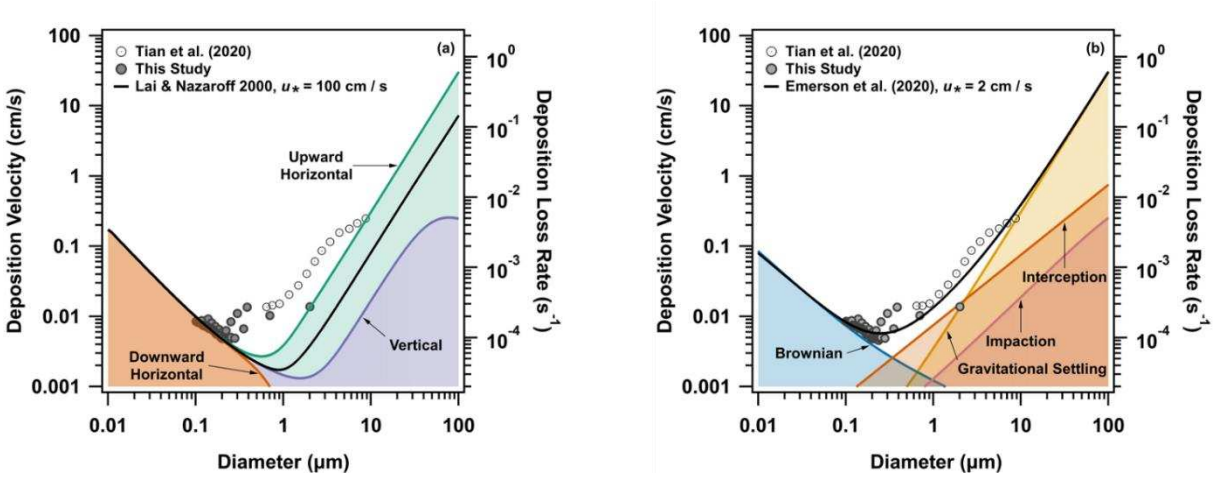

Figure 1.2: Size-dependent deposition for accumulation mode aerosols from this study and coarse mode particles from Tian et al. (2020) observed for cooking aerosols during HOMEChem. The measured deposition is compared to **(a)** the indoor model developed by Lai and Nazaroff (2000) and **(b)** the outdoor model developed by Emerson et al. (2020). In both plots deposition velocity is displayed on the left axis and deposition loss rate is displayed on right axis. The data from this study, both POPS and UHSAS data, are represented by the filled data points.

average difference of 10 ± 9 % in the accumulation mode and 30 ± 10 % in the coarse mode (**Figure 1S.14**). The model was also able to accurately reproduce the minimum (around 200 nm) in the observed deposition trend, in contrast to Lai and Nazaroff (2000). Tian et al. (2020) provide deposition rates for supermicron cooking particles at HOMEChem. Impaction and interception likely affect particles larger than 10 µm, which is at the limit of most indoor deposition measurements. Further measurements are thus needed to characterize the processes driving deposition of larger particles indoors. However, the close agreement of the Emerson model and the HOMEChem deposition measurements suggests that this resistance-based approach may be a useful alternative to the established Lai and Nazaroff approach in indoor settings.

Our model comparisons indicate that interception is playing a larger role in indoor deposition than currently accounted for and that current indoor models are likely underestimating particle loss rates even when elevated u_* values are used. The agreement between our observed indoor deposition rates and the outdoor Emerson et al. (2020) model shows that incorporation of interception terms, as well as an increased emphasis on the physical processes controlling particle deposition could led to improvements in indoor deposition models. This conclusion is consistent with previous literature: Thatcher et al. (1996) showed from experiments measuring deposition rates of fluorescent particles onto surfaces in a small chamber that deposition models did not consider all of the physical processes influencing particle deposition, additionally Lai (2005) added interception terms to the widely-used Lai and Nazaroff (2000) model to improve model-measurement comparisons over an array of surfaces.[48,49]

The significance of underestimating particle deposition with the current indoor models is clearly illustrated through particle lifetime calculations. Using the Emerson et al. (2020) model, deposition loss rate for 100 nm, 1 µm, and 10 µm particles are estimated to be 0.0001 s^{-1}, 0.001 s^{-1}, and 0.01 s^{-1} respectively. Using these rates, the lifetimes of these particle sizes with respect to deposition are approximately 3 hours, 17 minutes, and 2 minutes, respectively. However, when the same estimation is done using the Lai and Nazaroff (2000) model – with a u_* value of 2 cm s^{-1}, as used in the Emerson et al.

(2020) model to obtain the best fit to the data – the lifetimes for the same sized particles become 74 hours, 20 hours, and 14 minutes, respectively. This elevation of lifetime with respect to deposition is highly problematic for determining what controls particle lifetime indoors. If we compare these rates with the particle lifetime from exfiltration, which is approximately 2 hours (based off an average *ACR* of 0.5 h^{-1} for the house), we see that the Lai and Nazaroff (2000)) model predicts that exfiltration will control the lifetime of all accumulation mode aerosols when in actuality the lifetime of larger accumulation mode and coarse mode particles are determined by their deposition rate. Both models suggest that lifetimes of smaller accumulation mode particles are impacted more by the ventilation of the house. Of course, lowering the ventilation rate will enhance the relative importance of deposition. These discrepancies are particularly relevant when considering the effectiveness of ventilation in controlling particle lifetime – Bond et al. (2020) suggest that these discrepancies in predicted indoor deposition rate may be substantial enough to impact recommendations for different mitigation techniques for reducing exhaled respiratory aerosol exposure.[50]

Coagulation is a second order process, dependent on concentration and is therefore important in areas of high concentrations, however, initial analysis of the size distribution over the course of typical cooking events did not indicate evidence of coagulation within the measured size range after emission and dilution (**Figure 1S.28**). In order to strengthen these observations and rule out the impact of coagulation on accumulation mode particles, we calculated coagulation rates based on an average particle distribution during cooking from the UHSAS, which included the median diameters and average associated concentrations (**Table 1S.29**).[51] These calculations indicate that over the course of an hour coagulation would only lower particle number concentration by 1 – 6%, thereby ruling out coagulation as a major sink for accumulation mode particles during typical cooking events (**Figure 1S.30**). This result was the same when concentrations of larger particles from a POPS were included in the calculations. However, during Thanksgiving experiments, the peak particle concentration was about four times higher than the concentration of the other cooking events. The elevated particle concentrations lasted longer due to the

sustained nature of the cooking events. Visual analysis of particle size distribution evolution during Thanksgiving indicates that coagulation is occurring (**Figure 1S.28**), and the theoretical calculations indicate that coagulation could account for a 1 - 12% decrease in particle concentration (**Figure 1S.30**). The recirculation time (2000 m^3 h^{-1}) is on average 30 times and 20 times greater than the calculated coagulation rate for typical cooking (0.03 – 10 particles cm^{-3} h^{-1}) and Thanksgiving (0.002 – 30 particles cm^{-3} h^{-1}) events respectively. These data indicate that when indoor mechanics – like an enhanced rate of air recirculation in the house – are impacting particles by rapidly mixing particles through the space, particle concentration needs to be highly elevated for a period that greatly exceeds the air residence time of the house before coagulation occurs in the accumulation mode.

Transport and Spatial Variation of Particles

Size distribution characteristics have been previously observed in multi-zone environments[27,30]; however, processes that control the changes in magnitude and shape of particle size distributions between zones have not been thoroughly explored. In this work, we analyzed different zonal distributions to determine which size-dependent physical processes contribute to the development of a spatial gradient.

During all cooking events, a significant concentration gradient was observed throughout the house (**Figure 1.3**). This gradient persisted until the end of the cooking event. Between the kitchen and the living room there was, on average, a 40 ± 10 % decrease in the total particle number concentration, integrated over the entire cooking event (30 ± 20 % for surface area, and 30 ± 20 % in mass). Number concentration in the bedroom was, on average, 70 ± 10 % lower (60 ± 10 % for surface area, 50 ± 20 % in mass) than what was measured in the kitchen. The spikes in the concentration during events had a slight time offset between zones, with 0.7 ± 0.1 minutes between kitchen and living room signal peaks and 2.4 ± 0.9 minutes between the kitchen and the bedroom peaks.

We observed a particle size dependence in the concentration gradient. Percent differences were calculated as a function of size using the POPS data. Accumulation mode particles between 130 - 250 nm

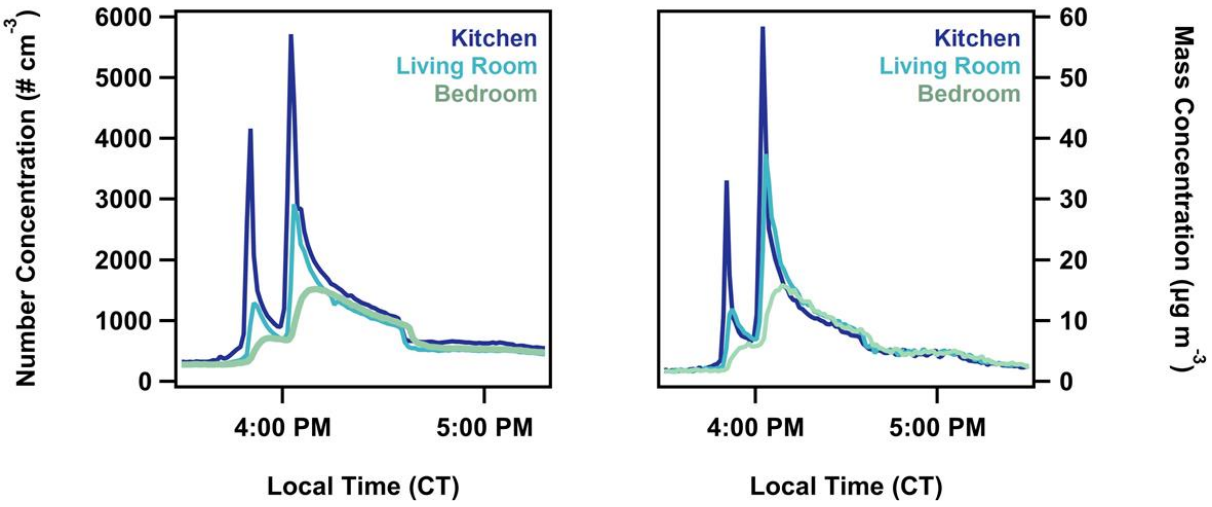

Figure 1.3: Time series of a typical stir-fry cooking event, with data from the POPS in all three rooms monitored during the experiments. The left panel shows number concentration and the right panel shows mass concentration (using an assumed density of 1.0 g cm^{-3}) over the course of the stir-fry.

generally had a higher percent difference compared to 250 nm – 3 µm particles (**Figure 1.4, Table 1S.12, Table 1S.13**). This size dependence explains the small changes in percent differences for total concentration measurements in number, area, and volume space for the measured size range. Higher percent differences between the zones for the particles bellow 250 nm indicate that a loss mechanism favoring the removal of these particles is contributing to spatial variation. One possibility for this removal mechanism is the entrapment of smaller particles in eddies created by the air flow through the house. Due to their smaller inertia and relaxation times, accumulation mode particles become trapped in the circulating flows of the house and are therefore not transported as easily as coarse particles are between zones. This mechanism has been proposed by multi-zone models but not directly observed before this work.[52,53] Alternatively, this could be the result of error and variability between the POPS measurements and more work would be needed to address the true source of this difference.

Impact of Sinks on Spatial Variation

While deposition and exfiltration are the dominant sinks for particles within a given zone, their estimated contribution to the measured loss rates are too slow to account for the magnitude of the particle concentration differences between zones for the measured size range during HOMEChem. Using the observed time offset (0.7 ± 0.1 minutes and 2.4 ± 0.9 minutes for the living room and bedroom respectively) between particle appearance in the different zones and the observed deposition and exfiltration rates, we calculated the contribution of each of these sinks to the gradient observed. Application of estimated losses from deposition and exfiltration to the measured particle concentration in the kitchen resulted in a 0.009 ± 0.006 % loss between the kitchen and the living room and a 0.03 ± 0.02 % loss between the kitchen and the bedroom. This change is negligible compared to the observed losses between the zones, therefore ruling out deposition and exfiltration as mechanisms that contribute significantly to the development of concentration gradients indoors. The minor impact of deposition on these concentration gradients is also evidenced by the fact that 130 - 250 nm accumulation mode particles had higher percent differences than the 250 nm – 3 µm particles. If the observed particle concentration

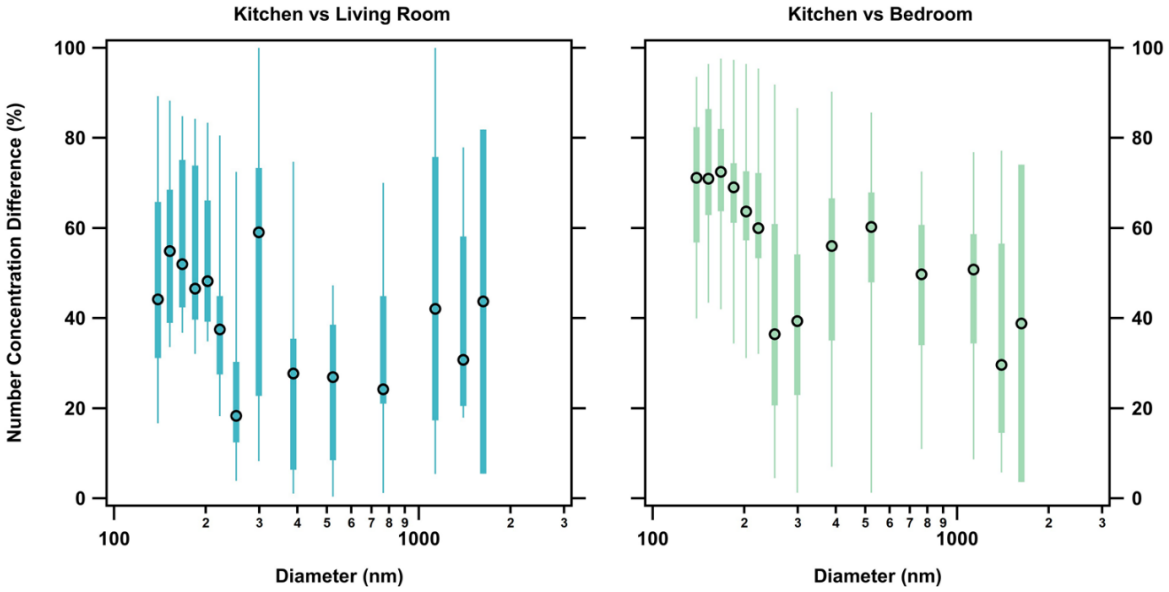

Figure 1.4: Size-dependent percent changes in aerosol number concentration between the kitchen and the other zones. The lower and upper bounds of the boxes represent the second and third quartiles, respectively, and the center point indicates the median of the data. The lower and upper tails mark the minimum and maximums of the data. Smaller accumulation mode particles (> 250 nm) had larger concentration differences between the kitchen and living room **(left)** and the kitchen and the bedroom **(right)** than the larger particles (< 250 nm) in the mode.

gradient was driven by deposition losses, there would be larger differences in the concentrations of 250 nm – 3 µm particles due to their larger deposition rates. For example, a 1µm and 200 nm particle had observed deposition rates of approximately 0.7 ± 0.2 h^{-1} and 0.3 ± 0.2 h^{-1} respectively. If the gradient was driven by deposition alone, then larger accumulation mode particles would have approximately two times the loss of the smaller particles.

Dilution, via transport through the house, accounts for the bulk concentration change between zones. Calculated diluted distributions using the overall zone volumes compared well with the measured distributions although it underestimated the concentration (slope of 1.50 ± 0.05, R^2 = 0.99 for the living room comparison and slope of 1.35 ± 0.06, R^2 = 0.95 for the bedroom comparison) (**Figure 1.5**). The high associated error in larger size bins (produced by the low counts recorded for those particles) was accounted for when comparing the measured and calculated distributions. Agreement between measured concentrations and dilution calculations indicate that the loss between zones can be approximated using a simple dilution calculation when the internal recirculation rate of the indoor environment is high. Increased flow through the recirculation system (equivalent to 8 house volume exchanges h^{-1}) did not contribute significantly to the observed gradient; when applied to the observed kitchen measurements it produced a 0.07 ± 0. 04 % change between the kitchen and living room and 0.2 ± 0.1 % change between the kitchen and bedroom.

Conclusions

Significant spatial differences in particle concentration persist indoors throughout emission periods. Deposition and dilution are the most important factors controlling particle concentration within a zone. Larger differences in the accumulation mode particles between 130 - 250 nm compared to 250 nm – 3 µm particles between zones during cooking indicate that there is an additional loss process that favors smaller particles. This additional loss could be a result of indoor air flow trapping smaller particles as they are transported, which has been speculated in multi-zone models – but not directly observed before our work.[52,53] However, this could also be the result of instrument variability and error between the different

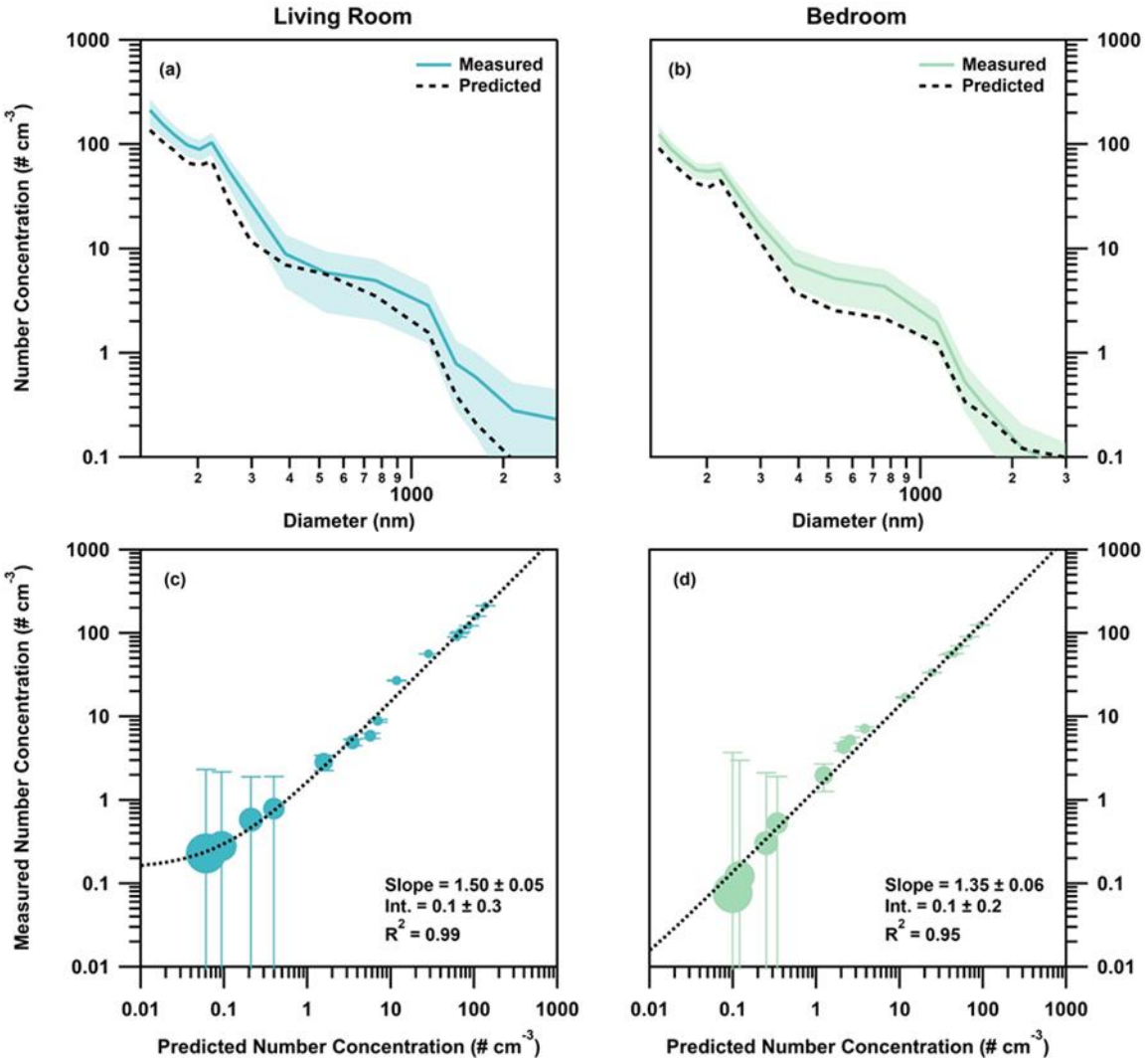

Figure 1.5: Average particle distribution for an entire stir-fry cooking event compared to the diluted source measurement: **(a)** kitchen to living room and **(b)** the living room to bedroom. The shaded regions represent the standard deviation of the measurement. Direct comparison between the diluted approximation to the measured distribution in **(c)** the living room and **(d)** the bedroom, with the error bars representing the error of the measurement. Marker size in the bottom panels is representative of particle size.

POPS instruments. Additionally, the deposition observations herein show that widely-used indoor models are inadequate for predicting particle deposition indoors, typically leading to an underestimate in particle loss rates for the accumulation mode. Incorporating interception terms into existing models improve model-measurement comparisons for this study, and may similarly improve the observed model-measurement discrepancies in previous studies.[49] Understanding and accurately modeling deposition processes is crucial for understanding particle lifetimes indoors, which determine how long particles, including those containing disease causing agents, persist in indoor environments. Characterizing deposition indoors is therefore necessary in establishing particle impact on human health and determining mitigation strategies.

However, these findings extend beyond understanding indoor particle dynamics and have implications for surface chemistry, gas uptake onto particles, and exposure assessments. Particle deposition impacts surface reservoirs indoors, which control multiphase surface chemistry.[54] Observed airborne gradients in particle concentration imply differences in particle loadings on surfaces, which would in turn modulate surface chemistry in different zones. Particle concentration and composition both influence gas-phase uptake onto particles.[55,56] Observed gradients indicate that this concentration-dependent partitioning process will occur differently throughout the house during cooking periods. For example, the uptake coefficient of dinitrogen pentoxide (N_2O_5) – which has been detected in indoor environments during cooking[57] – is inversely proportional to the available particle surface area.[58] Using our observed percent differences in particle surface area between zones, we estimate that N_2O_5 uptake could increase by 40% between the kitchen and the living room. However, this process is also complicated by the high surface-to-volume ratios of indoor environments, where particle surface area in the kitchen, living room, and bedroom only accounts for maximum of 0.06%, 0.04%, and 0.02% of the total available surface area, respectively. This would be especially true in fully furnished, more realistic environments. Thus, further analysis of indoor spatial variations in particle and gas species concentrations are needed to fully characterize the impacts of spatial gradients on partitioning processes.

Finally, these observed spatial gradients have significant implications for exposure assessment to individuals. Particle concentration indoors not only determines an individual's exposure to particulate matter, but can also dictate exposure to lower volatility gas-phase species like diethylhexyl phthalate (DEHP)[56,59], a common indoor phthalate found in building materials.[60] Particle phase DEHP correlates with increased particle concentration indoors, a process attributed to surface-to-gas-to-particle exchanges.[56,59] Transport of particles therefore provide a mechanism to move pollutants through homes. Our observations suggest this partitioning processes and subsequent exposures may have strong spatial gradients in the indoor environment.

CHAPTER 1 – REFERENCES

(1) Cohen, A. J.; Brauer, M.; Burnett, R.; Anderson, H. R.; Frostad, J.; Estep, K.; Balakrishnan, K.; Brunekreef, B.; Dandona, L.; Dandona, R.; Feigin, V.; Freedman, G.; Hubbell, B.; Jobling, A.; Kan, H.; Knibbs, L.; Liu, Y.; Martin, R.; Morawska, L.; Pope, C. A.; Shin, H.; Straif, K.; Shaddick, G.; Thomas, M.; van Dingenen, R.; van Donkelaar, A.; Vos, T.; Murray, C. J. L.; Forouzanfar, M. H. Estimates and 25-Year Trends of the Global Burden of Disease Attributable to Ambient Air Pollution: An Analysis of Data from the Global Burden of Diseases Study 2015. *The Lancet* **2017**, *389* (10082), 1907–1918. https://doi.org/10.1016/S0140-6736(17)30505-6.

(2) Pope III, C. A.; Dockery, D. W. Health Effects of Fine Particulate Air Pollution: Lines That Connect. *Journal of the Air & Waste Management Association* **2006**, *56* (6), 709–742. https://doi.org/10.1080/10473289.2006.10464485.

(3) Dockery, D. W.; Pope III, C. A. Acute Respiratory Effects of Particulate Air Pollution. *Annual Review of Public Health* **1994**, *15* (1), 107–132. https://doi.org/10.1146/annurev.pu.15.050194.000543.

(4) Brook Robert D.; Rajagopalan Sanjay; Pope C. Arden; Brook Jeffrey R.; Bhatnagar Aruni; Diez-Roux Ana V.; Holguin Fernando; Hong Yuling; Luepker Russell V.; Mittleman Murray A.; Peters Annette; Siscovick David; Smith Sidney C.; Whitsel Laurie; Kaufman Joel D. Particulate Matter Air Pollution and Cardiovascular Disease. *Circulation* **2010**, *121* (21), 2331–2378. https://doi.org/10.1161/CIR.0b013e3181dbece1.

(5) Azimi, P.; Stephens, B. A Framework for Estimating the US Mortality Burden of Fine Particulate Matter Exposure Attributable to Indoor and Outdoor Microenvironments. *J Expo Sci Environ Epidemiol* **2020**, *30* (2), 271–284. https://doi.org/10.1038/s41370-018-0103-4.

(6) Klepeis, N. E.; Nelson, W. C.; Ott, W. R.; Robinson, J. P.; Tsang, A. M.; Switzer, P.; Behar, J. V.; Hern, S. C.; Engelmann, W. H. The National Human Activity Pattern Survey (NHAPS): A Resource for Assessing Exposure to Environmental Pollutants. *J Expo Sci Environ Epidemiol* **2001**, *11* (3), 231–252. https://doi.org/10.1038/sj.jea.7500165.

(7) Nazaroff, W. W. Indoor Particle Dynamics. *Indoor Air* **2004**, *14* (7), 175–183. https://doi.org/10.1111/j.1600-0668.2004.00286.x.

(8) Riley, W. J.; McKone, T. E.; Lai, A. C. K.; Nazaroff, W. W. Indoor Particulate Matter of Outdoor Origin: Importance of Size-Dependent Removal Mechanisms. *Environ. Sci. Technol.* **2002**, *36* (2), 200–207. https://doi.org/10.1021/es010723y.

(9) Howard-Reed, C.; Wallace, L. A.; Emmerich, S. J. Effect of Ventilation Systems and Air Filters on Decay Rates of Particles Produced by Indoor Sources in an Occupied Townhouse. *Atmospheric Environment* **2003**, *37* (38), 5295–5306. https://doi.org/10.1016/j.atmosenv.2003.09.012.

(10) Wallace, L. A.; Emmerich, S. J.; Howard-Reed, C. Effect of Central Fans and In-Duct Filters on Deposition Rates of Ultrafine and Fine Particles in an Occupied Townhouse. *Atmospheric Environment* **2004**, *38* (3), 405–413. https://doi.org/10.1016/j.atmosenv.2003.10.003.

(11) Wallace, L.; Kindzierski, W.; Kearney, J.; MacNeill, M.; Héroux, M.-È.; Wheeler, A. J. Fine and Ultrafine Particle Decay Rates in Multiple Homes. *Environ. Sci. Technol.* **2013**, *47* (22), 12929–12937. https://doi.org/10.1021/es402580t.

(12) Wallace, L. A.; Emmerich, S. J.; Howard-Reed, C. Source Strengths of Ultrafine and Fine Particles Due to Cooking with a Gas Stove. *Environ. Sci. Technol.* **2004**, *38* (8), 2304–2311. https://doi.org/10.1021/es0306260.

(13) He, C.; Morawska, L.; Taplin, L. Particle Emission Characteristics of Office Printers. *Environ. Sci. Technol.* **2007**, *41* (17), 6039–6045. https://doi.org/10.1021/es063049z.

(14) Schripp, T.; Wensing, M.; Uhde, E.; Salthammer, T.; He, C.; Morawska, L. Evaluation of Ultrafine Particle Emissions from Laser Printers Using Emission Test Chambers. *Environ. Sci. Technol.* **2008**, *42* (12), 4338–4343. https://doi.org/10.1021/es702426m.

(15) Kim, Y.; Yoon, C.; Ham, S.; Park, J.; Kim, S.; Kwon, O.; Tsai, P.-J. Emissions of Nanoparticles and Gaseous Material from 3D Printer Operation. *Environ. Sci. Technol.* **2015**, *49* (20), 12044–12053. https://doi.org/10.1021/acs.est.5b02805.

(16) Azimi, P.; Zhao, D.; Pouzet, C.; Crain, N. E.; Stephens, B. Emissions of Ultrafine Particles and Volatile Organic Compounds from Commercially Available Desktop Three-Dimensional Printers with Multiple Filaments. *Environ. Sci. Technol.* **2016**, *50* (3), 1260–1268. https://doi.org/10.1021/acs.est.5b04983.

(17) Klepeis, N. E.; Apte, M. G.; Gundel, L. A.; Sextro, R. G.; Nazaroff, W. W. Determining Size-Specific Emission Factors for Environmental Tobacco Smoke Particles. *Aerosol Science and Technology* **2003**, *37* (10), 780–790. https://doi.org/10.1080/02786820300914.

(18) Ferro, A. R.; Kopperud, R. J.; Hildemann, L. M. Source Strengths for Indoor Human Activities That Resuspend Particulate Matter. *Environ. Sci. Technol.* **2004**, *38* (6), 1759–1764. https://doi.org/10.1021/es0263893.

(19) Abt, E.; Suh, H. H.; Catalano, P.; Koutrakis, P. Relative Contribution of Outdoor and Indoor Particle Sources to Indoor Concentrations. *Environ. Sci. Technol.* **2000**, *34* (17), 3579–3587. https://doi.org/10.1021/es990348y.

(20) Patel, S.; Sankhyan, S.; Boedicker, E. K.; DeCarlo, P. F.; Farmer, D. K.; Goldstein, A. H.; Katz, E. F.; Nazaroff, W. W.; Tian, Y.; Vanhanen, J.; Vance, M. E. Indoor Particulate Matter during HOMEChem: Concentrations, Size Distributions, and Exposures. *Environ. Sci. Technol.* **2020**, *54* (12), 7107–7116. https://doi.org/10.1021/acs.est.0c00740.

(21) Lai, A. C. K.; Wang, K.; Chen, F. Z. Experimental and Numerical Study on Particle Distribution in a Two-Zone Chamber. *Atmospheric Environment* **2008**, *42* (8), 1717–1726. https://doi.org/10.1016/j.atmosenv.2007.11.030.

(22) Lu, W.; Howarth, A. T. Numerical Analysis of Indoor Aerosol Particle Deposition and Distribution in Two-Zone Ventilation System. *Building and Environment* **1996**, *31* (1), 41–50. https://doi.org/10.1016/0360-1323(95)00024-0.

(23) Chung, K. C. Three-Dimensional Analysis of Airflow and Contaminant Particle Transport in a Partitioned Enclosure. *Building and Environment* **1998**, *34* (1), 7–17. https://doi.org/10.1016/S0360-1323(97)00073-5.

(24) Zhao, B.; Zhang, Y.; Li, X.; Yang, X.; Huang, D. Comparison of Indoor Aerosol Particle Concentration and Deposition in Different Ventilated Rooms by Numerical Method. *Building and Environment* **2004**, *39* (1), 1–8. https://doi.org/10.1016/j.buildenv.2003.08.002.
(25) Kao, H.-M.; Chang, T.-J.; Hsieh, Y.-F.; Wang, C.-H.; Hsieh, C.-I. Comparison of Airflow and Particulate Matter Transport in Multi-Room Buildings for Different Natural Ventilation Patterns. *Energy and Buildings* **2009**, *41* (9), 966–974. https://doi.org/10.1016/j.enbuild.2009.04.005.
(26) Ju, Carole.; Spengler, J. D. Room-to-Room Variations in Concentration of Respirable Particles in Residences. *Environ. Sci. Technol.* **1981**, *15* (5), 592–596. https://doi.org/10.1021/es00087a600.
(27) Miller, S. L.; Nazaroff, W. W. Environmental Tobacco Smoke Particles in Multizone Indoor Environments. *Atmospheric Environment* **2001**, *35* (12), 2053–2067. https://doi.org/10.1016/S1352-2310(00)00506-9.
(28) Tang, M.; Zhu, N.; Kinney, K.; Novoselac, A. Transport of Indoor Aerosols to Hidden Interior Spaces. *Aerosol Science and Technology* **2020**, *54* (1), 94–110. https://doi.org/10.1080/02786826.2019.1677854.
(29) Singer, B. C.; Pass, R. Z.; Delp, W. W.; Lorenzetti, D. M.; Maddalena, R. L. Pollutant Concentrations and Emission Rates from Natural Gas Cooking Burners without and with Range Hood Exhaust in Nine California Homes. *Building and Environment* **2017**, *122*, 215–229. https://doi.org/10.1016/j.buildenv.2017.06.021.
(30) Mølgaard, B.; Ondráček, J.; Šťávová, P.; Džumbová, L.; Barták, M.; Hussein, T.; Smolík, J. Migration of Aerosol Particles inside a Two-Zone Apartment with Natural Ventilation: A Multi-Zone Validation of the Multi-Compartment and Size-Resolved Indoor Aerosol Model. *Indoor and Built Environment* **2014**, *23* (5), 742–756. https://doi.org/10.1177/1420326X13481484.
(31) Farmer, D. K.; Vance, M. E.; Abbatt, J. P. D.; Abeleira, A.; Alves, M. R.; Arata, C.; Boedicker, E.; Bourne, S.; Cardoso-Saldaña, F.; Corsi, R.; DeCarlo, P. F.; Goldstein, A. H.; Grassian, V. H.; Ruiz, L. H.; Jimenez, J. L.; Kahan, T. F.; Katz, E. F.; Mattila, J. M.; Nazaroff, W. W.; Novoselac, A.; O'Brien, R. E.; Or, V. W.; Patel, S.; Sankhyan, S.; Stevens, P. S.; Tian, Y.; Wade, M.; Wang, C.; Zhou, S.; Zhou, Y. Overview of HOMEChem: House Observations of Microbial and Environmental Chemistry. *Environ. Sci.: Processes Impacts* **2019**, *21* (8), 1280–1300. https://doi.org/10.1039/C9EM00228F.
(32) Cai, Y.; Montague, D. C.; Mooiweer-Bryan, W.; Deshler, T. Performance Characteristics of the Ultra High Sensitivity Aerosol Spectrometer for Particles between 55 and 800nm: Laboratory and Field Studies. *Journal of Aerosol Science* **2008**, *39* (9), 759–769. https://doi.org/10.1016/j.jaerosci.2008.04.007.
(33) Von der Weiden, S. L.; Drewnick, F.; Borrmann, S. Particle Loss Calculator – a New Software Tool for the Assessment of the Performance of Aerosol Inlet Systems. *Atmospheric Measurement Techniques* **2009**, *2* (2), 479–494. https://doi.org/10.5194/amt-2-479-2009.
(34) Gao, R. S.; Telg, H.; McLaughlin, R. J.; Ciciora, S. J.; Watts, L. A.; Richardson, M. S.; Schwarz, J. P.; Perring, A. E.; Thornberry, T. D.; Rollins, A. W.; Markovic, M. Z.; Bates, T. S.; Johnson, J. E.; Fahey, D. W. A Light-Weight, High-Sensitivity Particle Spectrometer for PM2.5 Aerosol Measurements. *Aerosol Science and Technology* **2016**, *50* (1), 88–99. https://doi.org/10.1080/02786826.2015.1131809.
(35) Thatcher, T. L.; Layton, D. W. Deposition, Resuspension, and Penetration of Particles within a Residence. *Atmospheric Environment* **1995**, *29* (13), 1487–1497. https://doi.org/10.1016/1352-2310(95)00016-R.
(36) Manuja, A.; Ritchie, J.; Buch, K.; Wu, Y.; Eichler, C. M. A.; Little, J. C.; Marr, L. C. Total Surface Area in Indoor Environments. *Environ. Sci.: Processes Impacts* **2019**, *21* (8), 1384–1392. https://doi.org/10.1039/C9EM00157C.
(37) Lai, A. C. K.; Nazaroff, W. W. Modeling Indoor Particle Deposition from Turbulent Flow onto Smooth Surfaces. *Journal of Aerosol Science* **2000**, *31* (4), 463–476. https://doi.org/10.1016/S0021-8502(99)00536-4.

(38) Emerson, E. W.; Hodshire, A. L.; DeBolt, H. M.; Bilsback, K. R.; Pierce, J. R.; McMeeking, G. R.; Farmer, D. K. Revisiting Particle Dry Deposition and Its Role in Radiative Effect Estimates. *PNAS* **2020**. https://doi.org/10.1073/pnas.2014761117.
(39) Zhang, L.; Gong, S.; Padro, J.; Barrie, L. A Size-Segregated Particle Dry Deposition Scheme for an Atmospheric Aerosol Module. *Atmospheric Environment* **2001**, *35* (3), 549–560. https://doi.org/10.1016/S1352-2310(00)00326-5.
(40) Hinds, W. C. *Aerosol Technology: Properties, Behavior, and Measurement of Airborne Particles*, 2nd ed.; John Wiley & Sons, Inc.: New York, NY, 1999.
(41) Hussein, T.; Glytsos, T.; Ondráček, J.; Dohányosová, P.; Ždímal, V.; Hämeri, K.; Lazaridis, M.; Smolík, J.; Kulmala, M. Particle Size Characterization and Emission Rates during Indoor Activities in a House. *Atmospheric Environment* **2006**, *40* (23), 4285–4307. https://doi.org/10.1016/j.atmosenv.2006.03.053.
(42) He, C.; Morawska, L.; Gilbert, D. Particle Deposition Rates in Residential Houses. *Atmospheric Environment* **2005**, *39* (21), 3891–3899. https://doi.org/10.1016/j.atmosenv.2005.03.016.
(43) Thatcher, T. L.; Lai, A. C. K.; Moreno-Jackson, R.; Sextro, R. G.; Nazaroff, W. W. Effects of Room Furnishings and Air Speed on Particle Deposition Rates Indoors. *Atmospheric Environment* **2002**, *36* (11), 1811–1819. https://doi.org/10.1016/S1352-2310(02)00157-7.
(44) Vette, A. F.; Rea, A. W.; Lawless, P. A.; Rodes, C. E.; Evans, G.; Highsmith, V. R.; Sheldon, L. Characterization of Indoor-Outdoor Aerosol Concentration Relationships during the Fresno PM Exposure Studies. *Aerosol Science and Technology* **2001**, *34* (1), 118–126. https://doi.org/10.1080/02786820117903.
(45) Lee, W.-C.; Wolfson, J. M.; Catalano, P. J.; Rudnick, S. N.; Koutrakis, P. Size-Resolved Deposition Rates for Ultrafine and Submicrometer Particles in a Residential Housing Unit. *Environ. Sci. Technol.* **2014**, *48* (17), 10282–10290. https://doi.org/10.1021/es502278k.
(46) Tian, Y.; Arata, C.; Boedicker, E.; Lunderberg, D. M.; Patel, S.; Sankhyan, S.; Kristensen, K.; Misztal, P. K.; Farmer, D. K.; Vance, M.; Novoselac, A.; Nazaroff, W. W.; Goldstein, A. H. Indoor Emissions of Total and Fluorescent Supermicron Particles during HOMEChem. *Indoor Air* **2020**. https://doi-org.ezproxy2.library.colostate.edu/10.1111/ina.12731.
(47) Slinn, W. G. N. Predictions for Particle Deposition to Vegetative Canopies. *Atmospheric Environment (1967)* **1982**, *16* (7), 1785–1794. https://doi.org/10.1016/0004-6981(82)90271-2.
(48) Thatcher, T. L.; Fairchild, W. A.; Nazaroff, W. W. Particle Deposition from Natural Convection Enclosure Flow Onto Smooth Surfaces. *Aerosol Science and Technology* **1996**, *25* (4), 359–374. https://doi.org/10.1080/02786829608965402.
(49) Lai, A. C. K. Modeling Indoor Coarse Particle Deposition onto Smooth and Rough Vertical Surfaces. *Atmospheric Environment* **2005**, *39* (21), 3823–3830. https://doi.org/10.1016/j.atmosenv.2005.02.055.
(50) Bond, T. C.; Bosco-Lauth, A.; Farmer, D. K.; Francisco, P. W.; Pierce, J. R.; Fedak, K. M.; Ham, J. M.; Jathar, S. H.; VandeWoude, S. Quantifying Proximity, Confinement, and Interventions in Disease Outbreaks: A Decision Support Framework for Air-Transported Pathogens. *medRxiv* **2020**, 2020.09.09.20187625. https://doi.org/10.1101/2020.09.09.20187625.
(51) Seinfeld, J. H.; Pandis, S. N. *Atmospheric Chemistry and Physics: From Air Pollution to Climate Change*, 3rd ed.; John Wiley & Sons, Inc.: New York, NY, 1998.
(52) Chang, T.-J.; Hu, T.-S. Transport Mechanisms of Airborne Particulate Matters in Partitioned Indoor Environment. *Building and Environment* **2008**, *43* (5), 886–895. https://doi.org/10.1016/j.buildenv.2007.01.030.
(53) Chang, T.-J.; Kao, H.-M.; Hsieh, Y.-F. Numerical Study of the Effect of Ventilation Pattern on Coarse, Fine, and Very Fine Particulate Matter Removal in Partitioned Indoor Environment. *Journal of the Air & Waste Management Association* **2007**, *57* (2), 179–189. https://doi.org/10.1080/10473289.2007.10465311.
(54) D. Abbatt, J. P.; Wang, C. The Atmospheric Chemistry of Indoor Environments. *Environmental Science: Processes & Impacts* **2020**, *22* (1), 25–48. https://doi.org/10.1039/C9EM00386J.

(55) Collins, D. B.; Wang, C.; Abbatt, J. P. D. Selective Uptake of Third-Hand Tobacco Smoke Components to Inorganic and Organic Aerosol Particles. *Environ. Sci. Technol.* **2018**, *52* (22), 13195–13201. https://doi.org/10.1021/acs.est.8b03880.
(56) Lunderberg, D. M.; Kristensen, K.; Tian, Y.; Arata, C.; Misztal, P. K.; Liu, Y.; Kreisberg, N.; Katz, E. F.; DeCarlo, P. F.; Patel, S.; Vance, M. E.; Nazaroff, W. W.; Goldstein, A. H. Surface Emissions Modulate Indoor SVOC Concentrations through Volatility-Dependent Partitioning. *Environ. Sci. Technol.* **2020**, *54* (11), 6751–6760. https://doi.org/10.1021/acs.est.0c00966.
(57) Arata, C.; Zarzana, K. J.; Misztal, P. K.; Liu, Y.; Brown, S. S.; Nazaroff, W. W.; Goldstein, A. H. Measurement of NO3 and N2O5 in a Residential Kitchen. *Environ. Sci. Technol. Lett.* **2018**, *5* (10), 595–599. https://doi.org/10.1021/acs.estlett.8b00415.
(58) Brown, S. S.; Dubé, W. P.; Fuchs, H.; Ryerson, T. B.; Wollny, A. G.; Brock, C. A.; Bahreini, R.; Middlebrook, A. M.; Neuman, J. A.; Atlas, E.; Roberts, J. M.; Osthoff, H. D.; Trainer, M.; Fehsenfeld, F. C.; Ravishankara, A. R. Reactive Uptake Coefficients for N2O5 Determined from Aircraft Measurements during the Second Texas Air Quality Study: Comparison to Current Model Parameterizations. *Journal of Geophysical Research: Atmospheres* **2009**, *114* (D7). https://doi.org/10.1029/2008JD011679.
(59) Lunderberg, D. M.; Kristensen, K.; Liu, Y.; Misztal, P. K.; Tian, Y.; Arata, C.; Wernis, R.; Kreisberg, N.; Nazaroff, W. W.; Goldstein, A. H. Characterizing Airborne Phthalate Concentrations and Dynamics in a Normally Occupied Residence. *Environ. Sci. Technol.* **2019**, *53* (13), 7337–7346. https://doi.org/10.1021/acs.est.9b02123.
(60) Shi, S.; Cao, J.; Zhang, Y.; Zhao, B. Emissions of Phthalates from Indoor Flat Materials in Chinese Residences. *Environ. Sci. Technol.* **2018**, *52* (22), 13166–13173. https://doi.org/10.1021/acs.est.8b03580.

CHAPTER 2 - SEASONAL VARIATION IN PARTICLE FLUX AND THE EFFECT OF ENVIRONMENTAL CONDITIONS ON SIZE-RESOLVED DRY DEPOSITION IN A PINE FOREST[3]

Chapter Overview

Dry deposition is a fundamental process that removes particles from the atmosphere, and therefore directly controls their lifetime and total impact on air quality and radiative forcing. The processes influencing dry deposition are poorly constrained in models. Seasonal changes in dry deposition remain uncertain due to the lack of observations over multiple seasons. We present measurements of size-resolved sub-micron particle deposition from a flux study that surveyed all four major seasons. Particle concentrations and therefore fluxes were highest in the summer and lowest in the winter. Size-dependent deposition velocities in all seasons were consistent with previously observed trends, however, our observations show a 130 ± 60% increase in wintertime deposition velocity compared to the summer, which is not currently captured in size-resolved deposition models. We explore the influence of scalar gradients and changes in environmental conditions as possible drivers of this increase. We find that phoretic effects, such as thermophoresis, and the addition of snow to the canopy had negligible impacts on our canopy level measurements. While turbophoresis impacted the observed seasonal changes in size-resolved particle deposition velocity, it did not fully explain the observed differences between the summer and winter. We suggest that the increase in deposition velocity is instead caused by changes to the leaf-level conditions and physiology during the wintertime, which increase interception of particles.

[3] Boedicker, E.K; DeBolt, H.M.; Fulgam, R.; Emerson, E.W.; Farmer, D.K. Seasonal variation in particle flux and the effect of environmental conditions on size-resolved dry deposition in a pine forest. This paper is currently with coauthors and is close to submission.

Introduction

Particles impact the quality of the air and radiative balance of Earth's atmosphere as a function of their size, chemical composition, and lifetime. The lifetime of particles is controlled by their rate of removal. The two removal pathways for particles from the atmosphere are wet deposition, which is the scavenging of particles and subsequent removal by precipitation, and dry deposition, which is the removal of particles through interactions with terrestrial and aquatic surfaces. Dry deposition of particles in the accumulation mode is currently the largest source of uncertainty in global models in the prediction of concentrations of cloud condensation nuclei and the prediction of particle impacts on cloud albedo [1–3]. Uncertainty in dry deposition removal rates stem from both inaccuracy in current theoretical parameterizations and the limited spatial and temporal coverage of measurements, especially over certain terrestrial surfaces during seasons other than summertime. Understanding the removal of particles through dry deposition is critical for constraining particle lifetime and therefore total impact in the atmosphere. While there have been major strides in quantifying and understanding dry deposition, large gaps in our knowledge of underlying deposition mechanisms persist [4–7].

Several terms can be used to describe the biosphere-atmosphere exchange of particles. Particle flux describes the net exchange of particles and is strongly influenced by changes in particle concentration and size distribution in an environment. Environments exhibit seasonal changes in concentration and size distribution that can influence particle flux; this is easily observed in urban environments where local particle sources persist. During the winter in urban regions particle concentration and therefore flux often increase due to an increased use of heating systems [8]. In contrast, rural environments often see increases in particle flux during the summer due to the dominance of biogenic secondary organic aerosol. In the same way, size distribution changes can influence particle flux. For these reasons particle flux is ideal for identifying sources of particles within an environment. Exchange velocity (V_{ex}) is derived from the flux and is independent of the particle concentration, describing the vertical directional movement of particles in an environment. Both flux and V_{ex} follow the

same sign convention where positive indicates upward movement, or emission, and negative indicates downward movement, or deposition. Deposition velocity (V_{dep}) describes the portion of exchange velocities that have a downward direction – using a positive sign for velocities directed downward towards biosphere surfaces– and defines how quickly particles are collected by the surface. Since these terms are independent of concentration, their behavior should remain unchanged unless there are shifts in the underlying mechanisms driving these velocities.

The extent to which the mechanisms behind dry deposition velocity over terrestrial ecosystems vary with ecosystem properties or other seasonally varying parameters remains poorly constrained by observations. Few studies have presented either bulk aerosol deposition velocity[9–12] or size resolved deposition measurements across seasons [13–15]. These studies typically observe seasonal differences in both particle flux and deposition velocity and have raised several hypotheses regarding seasonality of particle dry deposition. In their study of cloud droplet deposition (3 – 31 µm), Gallagher et al. (1992) observed a reduction in deposition velocity during wintertime snow cover that they attributed to the addition of snow to the canopy thereby reducing overall surface roughness.[15] In contrast, Mammarella et al. (2011) observed an increase in deposition velocity in the winter, while the fall and summer periods had the lowest deposition velocities.[14] Mammerella et al. suggested wintertime enhancements in ultrafine (0.020 – 0.065 µm) particle deposition velocities were due to thermophoretic effects, and changes to other particle sizes were due to either turbophoretic effects or changes in the concentration of various modes in the seasonal distributions. Thermophoresis occurs whenever there is a strong thermal gradient surrounding a particle. Thermophoretic deposition only occurs when a cold surface interacts with a warmer aerosol-laden flow. Turbophoresis is the movement of particles by gradients in turbulence. For this mechanism, increased turbulence in areas above the canopy and collecting surface drive particle collisions and interactions which in turn move particles away from the areas of high turbulence and towards regions of low turbulence. In this way both processes enhance the interaction time between the particle and the surface, therefore increasing the deposition velocity. Phoretic effects describe the effects

of all scalar gradients, including thermophoresis and turbophoresis, and have been explored as contributors to deposition over snow and ice surfaces [16,17]. Turbophoresis in particular has been considered as a contributor to particle deposition in forests where trees create significant gradients in turbulence between the top of the canopy and the forest floor [18,19]. Another seasonal factor that could impact dry deposition is the condition of the forest canopy or vegetation structure. Particle uptake by vegetation is a significant contributor to dry deposition [20], and plant morphology and physiology impacts particle deposition [21–23]. Changes to the canopy structures affect eddy penetration which could also impact turbophoresis. Seasonal changes in leaf-level conditions could therefore have significant impacts on dry deposition. The relative influence of each of these proposed mechanisms has not been critically evaluated, due to the limitations of available measurements, but they have been incorporated in some particle deposition models.

The objective of this work was to investigate seasonal variation in particle concentration and fluxes over a temperate pine forest from the Seasonal Particles in Forests Flux studY (SPiFFY) in 2016. We present general trends in meteorology, particle concentration and distribution, and particle flux across the four seasons: winter, spring, summer, and fall. Additionally, we present seasonal trends in total and size-resolved particle deposition velocity compared to current resistance model parameters. This work explores the drivers of seasonal variations in particle deposition and presents new evidence for the addition of previously neglected mechanisms in dry deposition modules as well as the inclusion of seasonally specific constants.

Methods

Site Description

The Seasonal Particles in Forests Flux studY (SPiFFY) was conducted at Manitou Experimental Forest Observatory (MEFO) located within Manitou Experimental Forest in central Colorado, USA (39.1006°N, 105.0942°W). Four measurement campaigns were performed between 2015 and 2016, each

representative of one of the major seasons: winter (February 1 – March 1, 2016), spring (April 15−May 15, 2016), summer (July 14−September 16, 2016), and fall (October 1−November 1, 2016). Manitou Experimental Forest is approximately 6760 ha of ponderosa pine, Douglas fir, mixed conifer, and aspen vegetation with an average canopy height of 16 m. Manitou Experimental Forest elevation ranges from 2280 – 2840 m above sea level. The MEFO tower site is described in detail by Ortega et al. (2014).[24] Measurements were made at the 30 m walk-up tower at MEFO, with instrumentation installed in an exterior trailer at the base of the tower. The footprint of the tower was dominated by Ponderosa pine trees reaching 16 m in height.

Fulgham et al. (2019) summarized the meteorology of the site across the four seasons during SPiFFY, which is presented in **Figure 2.1** and **Table 2.1**.[25] The friction velocity (u^*) and sensible heat flux (H) followed the conventional diel cycles associated with increases in solar heating during the day, enhancing turbulence, and decreases at night (**Figure 2.1**). This trend is observed in all four seasons, with the summer and fall having the strongest increase in sensible heat during the day. Friction velocities were comparable across seasons; however, the winter did exhibit higher turbulence during nighttime periods than other seasons. Further details of the site set up and these trends can be found in Supplemental **Figure 2S.1 & 2S.2**.

Instrumentation

Size-resolved particle concentrations were measured using an Ultra-High Sensitivity Aerosol Spectrometer (UHSAS; DMT Inc., Longmont, CO).[26] The UHSAS had a 10 Hz time resolution and counted particles in 99 size bins (0.06 – 1 μm). The data was re-binned during analysis to 10 size bins, and data from 0.06 – 0.089 μm was not included in the analysis due to the presence of noise that caused irregular and severe fluctuations in the signal of that size range. Calibrations were run at the beginning of each deployment using NIST standard polystyrene latex spheres (60, 150, 300, 600, and 900 nm mobility diameter). System zeros were run using a HEPA filter and switch installed at the front of the main line.

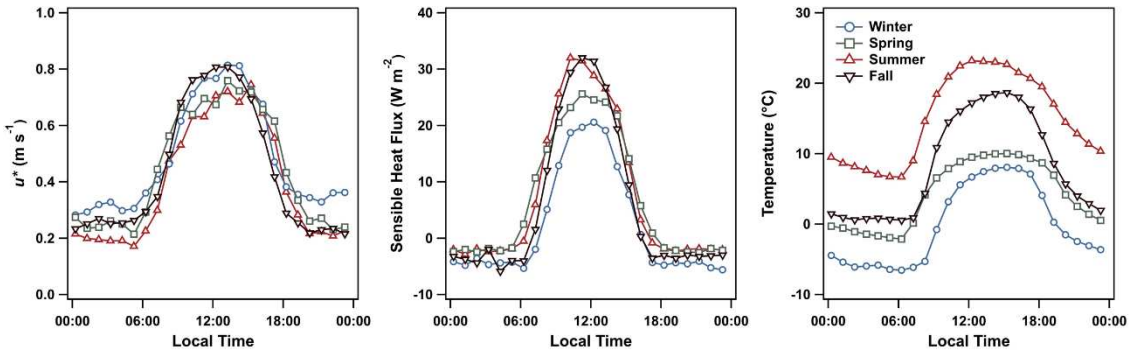

Figure 2.1: Average diel cycle for friction velocity (u^*), sensible heat flux (H), and air temperature of each season. Each point represents an hourly median value.

Table 2.1: Seasonal environmental daytime conditions, originally published by Fulgham et al. (2019)

	Friction Velocity (m/s) μ ± σ (min – max)	**Wind Speed (m/s) μ ± σ (min – max)**	**Temperature (°C)** μ ± σ (min – max)	**Relative Humidity (%)** μ ± σ (min – max)
Winter	0.5 ± 0.3 (0.025 – 1.6)	3.5 ± 2 (0.25 – 11)	7 ± 5 (-7.0 – 16)	27 ± 10 (8.0 – 88)
Spring	0.4 ± 0.3 (0.030 – 1.6)	3.6 ± 2 (0.0 – 18)	10 ± 6 (-3.7 – 21)	40 ± 20 (0.0 – 93)
Summer	0.4 ± 0.3 (0.030 – 1.5)	3.0 ± 1 (0.0 – 10)	23 ± 4 (11 – 29)	33 ± 20 (0.0 – 86)
Fall	0.4 ± 0.3 (0.005 – 1.7)	3.4 ± 2 (0.0 – 11)	15 ± 4 (0.5 – 23)	25 ± 10 (0.0 – 92)

The inlet set-up for the measurements consisted of a 28.98 m (ID: 7.14 mm, OD: 9.53 mm) copper line installed 25 m above ground level on the tower and was co-located with the sonic anemometer. A cone with metal mesh to keep out bugs and debris was affixed to the front of the inlet. Flow through the main line was maintained at ~20 L/min (Re ≈ 3900; residence time of 3.5 s in the main line) using a backing pump and mass flow controller. Inside the trailer, a 3.05 m line reduced to ID: 4.83 mm (OD: 6.35 mm), and the UHSAS sampled off the main line at 60 mL/min through its internal conductive silicone tubing (OD: 3.2 mm) (**Figure 2S.1**). Particle loss in the main line calculated using the method described by Von der Weiden et al. (2009) was determined to be negligible (<5%).[27]

Two different sonic anemometers were used during the campaign to measure three-dimensional wind speed and temperature. For the winter, spring, and summer periods (February 1 – August 5, 2016), we used a CSAT3 sonic anemometer (Campbell Scientific, Logan, UT). Inlet offsets from the CSAT were x = 20 cm, y = 40 cm, z = 10 cm. The fall measurements (October 1−November 1, 2016) used a SATI-series K-style sonic anemometer (Applied Technologies Inc., Boulder, CO). Inlet offsets from the SATI were x = 0 cm, y = 0 cm, z = 60. Both anemometers were set to record data at 10 Hz time resolution. Data from the CSAT3/SATI and UHSAS were logged on separate computers and the timestamps were synched to an online time server. Any observed clock drifts in the data were handled in post processing.

Eddy Covariance Measurements

Surface-atmosphere exchange was measured using eddy covariance flux techniques. The vertical flux (F_c) in this technique is determined by the covariance of the vertical wind speed (w) and a scalar (c; particle concentration):

$$F_c = \overline{w'c'} = \frac{1}{N}\sum_{i=0}^{N}(c_i - \bar{c})\,(w_i - \bar{w}) \qquad (2.1)$$

where N is the number of points, w_i and c_i are the instantaneous measurements of the vertical windspeed and particle concentration respectively, and $\bar{w}$ and $\bar{c}$ are the mean values. We used a flux averaging time

interval of 30-min. Deposition velocity can be derived from the vertical flux and the mean concentration over a given period.

$$F_c = -V_{dep}\,\bar{c} \quad (2.2)$$

Using this notation, a positive V_{dep} corresponds to deposition and a negative V_{dep} indicates an emission. We treat the positive and negative fluxes as two separate processes following uneven distribution of positive and negative fluxes around zero (**Figure 2S.3**). Only negative fluxes were used to derive deposition velocities, consistent with other particle flux studies [28,29]. Pryor et al. (2013) identified drivers of positive fluxes in a pine forest, which gives additional support to the separation of positive and negative fluxes in the calculation of deposition velocities (V_{dep}).[30] Additionally, the variability in some of the seasonal measurements was high, resulting in means either at the edge or outside the 25th to 75th confidence intervals; we thus use the medians of the deposition velocity data to investigate changes between seasons.

Data Treatment and Quality Control

Several quality controls were enforced on the data based on u^*, stationarity, and precipitation events. We also removed data taken during exceptional events. For example, during the fall campaign period, several prescribed burns were carried out in an area adjacent to MEFO. We exclude particle flux data from time periods in which CO concentration was elevated (> 3800 ppb), which resulted in the removal of data from 10th October. Data that did not meet the following requirements for u^*, stationarity, and precipitation quality control were rejected:

1. Periods in which turbulence was not well developed, defined by a friction velocity (u^*) < 0.14 m/s, were excluded [31,32].
2. Measurement periods in which the flux was not in steady state, as determined by a stationarity test, were excluded as they fail the assumptions of the eddy covariance method. A stationarity test compares 5-min fluxes to the full 30-min flux to ensure that the fluxes do not vary during the period of

interest [33]. A period is considered to have stationarity if the 5-min periods do not deviate from the 30-min period by more than 30%, and the following criterion is met:

$$0.7 < \frac{\overline{\langle w'c' \rangle_{5min}}}{\overline{\langle w'c' \rangle_{30min}}} < 1.3 \quad (2.3)$$

3. Precipitation events were excluded from this analysis, as they can affect the signal of the sonic anemometer and distort the measured flux. A total of 24 precipitation events occurred, 3 in the winter, 12 in the spring, 9 in the summer, and zero in the fall.

These filters resulted in 241, 180, 305, and 363 flux periods for winter, spring, summer, and fall respectively. Results of each test and the number of flux periods impacted is summarized in **Table 2.2** (**Figure 2S.3**).

Corrections

A single point storage correction was applied to the data in order to account for the difference in turbulent flux bellow the measurement height [11].

$$F_{storage} = \int_0^{z_r} \frac{\delta \bar{c}}{\delta t} dz \approx \frac{\overline{c(t+\Delta T)} - \overline{c(t)}}{\Delta T} \quad (2.4)$$

This storage correction resulted in a < 1% change in the total flux in all four seasons. Additionally, a two-dimensional rotation of windspeed in three axes corrected for the sonic anemometer not being mounted with a perfect level over the footprint [34,35].

Signal-to-Noise and Flux Uncertainty

To account for uncertainty in calculated flux measurements, we considered the signal-to-noise ratio of the UHSAS as well as flux uncertainty from instrument noise, counting statistics, and the covariance measurement. The signal-to-noise ratio of the UHSAS number concentration measurements is defined as the ratio between the mean concentration (μ) of a period and the standard deviation of the instrument signal during a system zero (σ_{zero}). A system zero is defined as a measurement period in

which a HEPA filter is placed in front of the inlet. Here an adjacent period to the system zero was used to calculate the signal-to-noise ratio in each season (**Figure 2S.4**).

$$SNR = \frac{\mu}{\sigma_{zero}} \tag{2.5}$$

Contribution of instrument noise to the flux uncertainty (δF_{noise}) was determined using the method described by Billesbach (2011).[36] In this method it is assumed that the contribution of instrument noise to the total uncertainty is the covariance when the correlation coefficient is minimized, which is achieved by randomizing the time sequence of the scalar, or particle concentration.

$$\delta F_{noise} = \frac{1}{M} \sum_{i,j=1}^{M} w'(t_i)\, c'(t_j) \tag{2.6}$$

where M is the number of measurements in the interval, w' and c' are the deviations from the mean vertical windspeed and concentration, and i and j are the time indices.

The uncertainty in the flux from counting discrete particles (ΔF_N) is calculated using the cumulative number of particles (N), along with the mean concentration ($\bar{c}$), and the variance of the vertical velocity (σ_w) during a flux period [37].

$$\Delta F_N = \frac{\sigma_w \bar{c}}{\sqrt{N}} \tag{2.7}$$

Finally, the uncertainty in the covariance is quantified here using the method outlined by Finkelstein and Sims (2001).[38] Estimation of the random error comes from the calculation of variance of a covariance when the two variables, here vertical windspeed and particle concentration, are lagged at unrealistic time scales (50 – 60s). Finkelstein and Sims (2001) outline the following parameterization for the variance of the covariance (σ^2):

$$\sigma^2 = \frac{1}{M} \left[\sum_{i=-m}^{m} \sigma_{x,x}^2(i)\, \sigma_{y,y}^2(i) + \sum_{i=-m}^{m} \sigma_{x,y}^2(i)\, \sigma_{y,x}^2(i) \right] \tag{2.8}$$

where M is the number of measurements in a flux period, $\sigma_{x,x}^2$ and $\sigma_{y,y}^2$ are the variance of the two variables, $\sigma_{x,y}^2$ and $\sigma_{y,x}^2$ are the estimated covariances of the two variables, and m is number of samples

used to captures the integral time scale (m = 200, 20s of 10 Hz data). The auto- ($\sigma_{x,x}^2$) and cross-covariance ($\sigma_{x,y}^2$) is computed for a lag (h) by:

$$\sigma_{x,x}^2(h) = \frac{1}{M}\sum_{i=1}^{M-h}(x_t - \bar{x})(x_{t+h} - \bar{x}) \quad (2.9)$$

$$\sigma_{x,y}^2(h) = \frac{1}{M}\sum_{i=1}^{M-h}(x_t - \bar{x})(y_{t+h} - \bar{y}) \quad (2.10)$$

The subsequent uncertainty in the covariance ($\sigma_{w'N'}$) ranged from 30 – 80 # cm^{-2} s^{-1}. We also evaluated the time-lagged covariance spectra for each flux period out to 50s to attempt and identify the time lag between the vertical windspeed and particle concentration measurements. However, the determination of a time lag by autocorrelation is problematic for data limited by counting statistics [39] so a fixed lag time of 3.5 s was used based off the flow through the inlet line. For all the calculations outlined above, some variable notation has been changed from the original source in order to have consistent references in this work. Results of the error analysis are summarized in **Table 2.3**. The instrumental and random noise were both within the measured variation of the particle fluxes, however, the uncertainty from counting discrete particles exceeded the measured variation. This indicates that the uncertainty from counting is the overwhelming contributor to uncertainty in these flux measurements.

Flux Limit of Detection

Limits of detection for individual flux periods (LOD_i) were first calculated considering random error using the method from Langford et al. (2015):

$$LOD_i = \alpha\, RE_i \quad (2.11)$$

with α being the specified confidence interval (α = 3 was used for the 99th percentile in this work), and RE_i representing the random error of the flux period from the Finkelstein and Sims (2001) calculation above ($\sigma_{w'N'}$).[38,39] Time-resolved limits of detection were used to calculate an average limit of detection for each season, LOD_{season}.

Table 2.2: Summary of quality control tests for the SPiFFY campaign. Number of flux periods that did not meet the quality control factor listed as well as the percent of the total available measurements that did not meet the standard, are presented for each test and each season. The original number of measurement periods is listed under the season headers, and the number of flux periods retained are listed in the final row.

	Winter (N=858)	Spring (N=1001)	Summer (N=1330)	Fall (N=1433)
u^*	76 (9%)	141 (14%)	198 (15%)	231 (16%)
Stationarity	513 (60%)	722 (72%)	965 (73%)	1019 (71%)
Precipitation	96 (11%)	279 (28%)	0 (0%)	12 (0.01%)
Accepted Flux Periods	**241 (28%)**	**180 (18%)**	**305 (23%)**	**363 (25%)**

Table 2.3: Summary of uncertainty and LOD for total particle flux measurements during SPiFFY

Total Flux ($\mu \pm \sigma$)	Winter (2 ± 70)	Spring (-60 ± 100)	Summer (-50 ± 100)	Fall
SNR	100	200	300	300
δF_{noise} (# cm^{-2} s^{-1})	20	30	30	20
ΔF_N (# cm^{-2} s^{-1})	800	2000	2000	1000
$\boldsymbol{\sigma_{w'N'}}$(# cm^{-2} s^{-1})	30	80	70	60
$\overline{\boldsymbol{LOD_{season}}}$ (# cm^{-2} s^{-1})	8	40	20	20
|Flux periods| > $\overline{\boldsymbol{LOD_{season}}}$ / TOTAL FLUX PERIODS	220/241	111/180	269/305	316/363

$$\overline{LOD_{season}} = \frac{1}{N}\sqrt{\sum_{i=1}^{N} LOD_i^2} \quad (2.12)$$

For this project, the average limits of detection for particle flux measurements using this method were 8 (winter), 40 (spring), 20 (summer), and 20 (fall) # cm^{-2} s^{-1}. These numbers are high compared to an *LOD* calculated through flux analysis on zero periods, which resulted in $\overline{LOD}_{zero}$ of 4 # cm^{-2} s^{-1} for both the winter and fall. While the $\overline{LOD}_{zero}$ needs further investigation if it is to be verified, the large difference between $\overline{LOD}_{season}$ and $\overline{LOD}_{zero}$ indicates a need for the critical evaluation of *LOD* calculation methods for flux measurements in the future.

Spectral Analysis

The UHSAS and other similar optical particle instruments have been previously used for eddy-covariance measurements, and their measurements have been validated using spectral analysis [13,40]. Here, we use spectral analysis to investigate and validate the measurements. Frequency weighted dimensionless cospectra of vertical wind speed and particle concentration followed the sensible heat, and the inertial subrange ($f^{-4/3}$) predicted by Kolmogorov theory is observed for each season between 0.01 and 5 Hz (**Figure 2.2**). **Figure 2.2** provides example cospectra for a 30-minute period from each season during the day where $u^* \geq 1$ m s^{-1} to reduce noise caused by low turbulence. Stability during the periods were -0.03, -0.04, -0.10, and -0.04 for the winter, spring, summer, and fall.

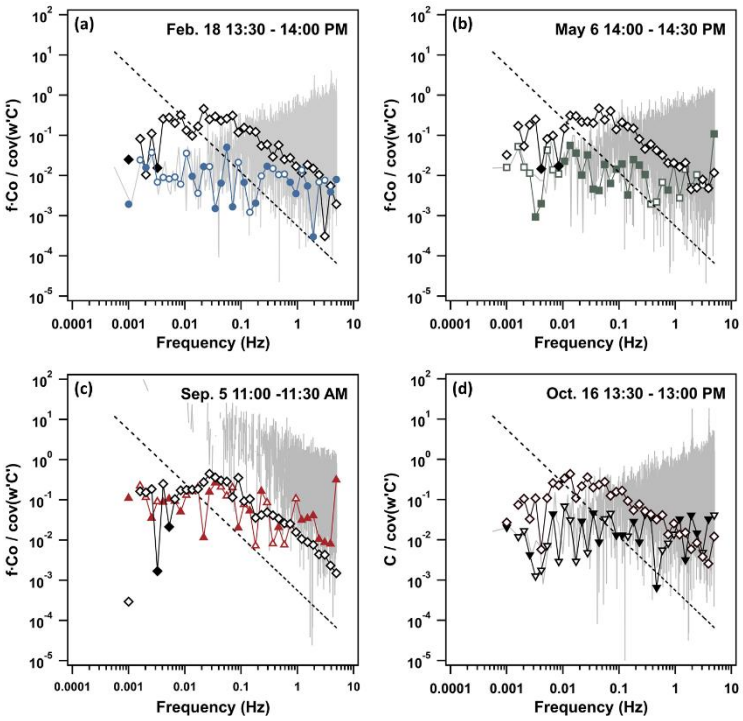

Figure 2.2: Frequency weighted dimensionless cospectral density of particle concentration (wC, color) and temperature (wT, black diamonds) with vertical wind speed for a representative 30-minute period for each of the four seasons. Individual data points are medians from 40 evenly spaced logarithmic bins, with open points representing positive data and closed points representing negative data that have been forced positive. The cospectra are presented for the (a) winter (blue circles), (b) spring (green squares), (c) summer (red upward triangles), and (d) fall (dark brown downward triangles). Raw wC cospectra are shown in light grey in the background and the inertial subrange ($f^{-4/3}$) is shown with the dashed line.

Deposition and Leaf Level Modeling

Deposition Models

We used the single layer resistance model from Emerson et al. (2020), which is based on the models presented by Zhang et al. (2001) and Slinn (1982), and aspects of the multi-layer model proposed by Katul et al. (2010) to investigate the roles of different mechanisms in controlling measured deposition velocities.[18,28,41,42] The full parameterization of Emerson et al. (2020) along with the relevant parameterizations from Katul et al. (2010) are in **Appendix 2A**. We integrated the work of Katul et al. (2010) into the deposition velocity framework of Emerson et al. (2020) in order to investigate the impact of turbophoresis on particle deposition. Following Zhang and Slinn, the Emerson et al. (2020) framework is based on the gravitational settling velocity (V_g), the aerodynamic resistance (R_a), and the surface resistance (R_s).

$$V_d(d_p) = V_g(d_p) + \frac{1}{R_a + R_s} \tag{2.13}$$

We then incorporated the term developed by Katul et al. (2010) describing the collection efficiency of turbophoresis (E_{turbo}) into the surface resistance parameterization (R_s) from the Emerson et al. (2020) model by adding it in series to the collection efficiencies of Brownian diffusion processes (E_b), impaction (E_{im}), and interception (E_{in}) (Eq. 2.14).

$$R_s = \frac{1}{\varepsilon_0\, u^*\, (E_b + E_{im} + E_{in} + \boldsymbol{E_{turbo}})\, R_1} \tag{2.14}$$

$$E_{turbo} = \frac{\tau_p}{1 + \frac{\tau_p}{\tau}} \left(\frac{\sigma_w^2}{\pi\, b\, \eta}\right) \tag{2.15}$$

The new surface resistance relies on the previously listed collection efficiencies, friction velocity (u^*), and the bounce correction (R_1) along with the empirical constant $\varepsilon_0 = 3$. E_{turbo} is dependent on the particle relaxation time (τ_p), Lagrangian turbulent timescale (τ), the standard deviation of the vertical velocity (σ_w), the thickness of the viscous sublayer for the vertical velocity variance (b), which can range

from $5 < b < 50$, and the kinematic viscosity of air (η). In the parameterization for E_{turbo}, the particle relaxation time (τ_p) is the size dependent term (**Appendix 2A**). While we were able to use measured values for σ_w and in the calculation of the Lagrangian turbulent timescale, these values can be approximated using u^*. [43] Standard deviation of the vertical velocity trends linearly with u^*, with an acceptable approximation being $\sigma_w \approx 1.0\, u^* - 1.2\, u^*$ [43]. Data from all four measurement periods of the SPiFFY campaign had a relationship of $\sigma_w \approx 1.1\, u^*$ (**Figure 2S.5**). Additionally, the Lagrangian turbulent timescale can be approximated by $\tau \approx (0.3\, u^*) / (1.1\, u^*)^2$. This approximation relies on the σ_w/u^* relationship from before as well as $u^*/\,\overline{U} \approx 0.3$ [43,44], which we were also able to validate using the SPiFFY data (**Figure 2S.6**).

Leaf Level Energy Balance and Thermophoretic Settling Velocity

We used a simple leaf energy balance to explore leaf effects on particle deposition. The energy balance calculations were based on equations outlined by Monteith and Unsworth (1990), Sridhar and Elliott (2002), and Jones (2013).[45–47] We used the open-source single point leaf energy balance framework developed by Kevin Tu (http://landflux.org/Tools.php) to help structure the energy balance. We adapted these equations and frameworks to work with real time meteorology data reported by the U.S. Forest Service [48] along with sonic anemometer data collected during the campaign periods. A full description of the leaf energy balance calculation is in **Appendix 2B**.

Thermophoretic settling velocity was calculated following Salthammer et al. (2011) and Hinds (1999).[49,50] This velocity was then integrated into the Emerson et al. (2020) deposition model (**Appendix 2B**).

Results and Discussion

Seasonal trends in particle fluxes and concentrations

Total (0.08–1 µm) particle concentration (# cm^{-3}), flux (# cm^{-2} s^{-1}), and exchange velocity (V_{ex}, cm s^{-1}) all exhibited distinct diel cycles (**Figure 2.3, Figure 2S.7**). The flux and V_{ex} magnitude peak in the middle of the day due to increased turbulence (see u^* in **Figure 2.1**), while particle number concentration peaks at night and decreases during the day as the boundary layer grows and mixes with larger volumes. Daytime fluxes were largest in the summer and spring measurement periods, with nighttime fluxes being comparable across all four seasons. Flux measurements were dominated by downward fluxes in all seasons, except the winter, resulting in negatively skewed flux data (**Figure 2S.3**).

As discussed in the introduction, particle concentration and size distribution can impact the direction and magnitude of particle fluxes. Particle concentrations were highest in the summer and lowest in the winter, providing a partial explanation for the larger particle fluxes in summer versus winter. As exchange and deposition velocities are independent of concentration, seasonal shifts in size distribution could potentially account for the observed seasonality in these values. However, no major changes in the average size distribution occurred between seasons (**Figure 2.3**). Daytime count median diameters were 128 ± 8, 140 ± 20, 140 ± 10, and 130 ± 10 nm for the winter, spring, summer, and fall, respectively. These count median diameters did not change substantially at night (**Figure 2S.8**, **Table 2S.9**). Particle distributions did not change between periods of positive and negative flux (**Figure 2S.10**, **Table 2S.11**). This consistency in the distributions indicates that changes in total particle exchange velocities are not attributable to seasonal shifts in size distribution.

Measured and modeled seasonal trends in particle dry deposition

As noted above, we segregate the downward flux periods from periods in which upward fluxes occurred and used these downward fluxes and their associate particle number concentrations to calculate deposition velocity, V_{dep}. Our sign convention now switches to give positive velocities for V_{dep}. Deposition velocity

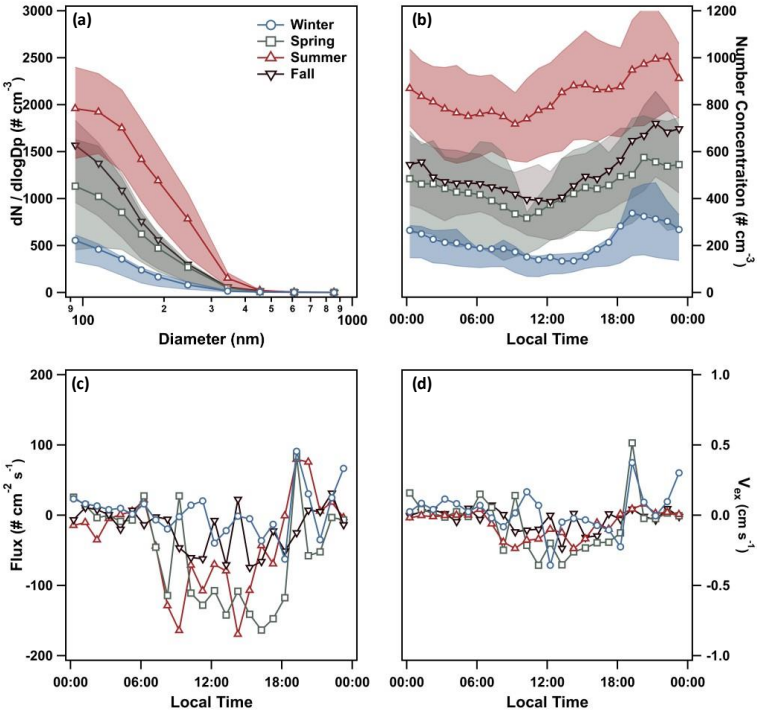

Figure 2.3: (a) Average daytime size distribution (dN/dlogDp) of particles for each season, with the 25th to 75th confidence intervals shaded, as well as diel trends of hourly mean (b) number concentration for particles 0.84 – 1 µm (also with the 25th to 75th confidence intervals shaded), (c) flux, and (d) exchange velocity (V_{ex}) across seasons.

for all particles measured followed the diel trend of both friction velocity and sensible heat flux, with peak values occurring around noon (**Figure 2.4**, **Figure 2S.12**). Additionally, size-dependent deposition velocities in each season followed trends previously observed in needleleaf forests [14,29,51–55]. Binned deposition velocity from all seasons had a strong linear relationship with friction velocity (**Figure 2.5**); this relationship was present in all size ranges measured during the study with larger particles having bigger slopes (**Figure 2S.13, Table 2S.14**). This trend is consistent with other particle deposition studies [13,53].

While total deposition velocity did not vary significantly between seasons, the size-dependent deposition velocity in the winter was greater than in the spring, summer, and fall. The enhancement of winter deposition relative to summer was the largest and ranged from 23 – 202% (130 ± 60%) depending on particle size, with particles less than 0.35 µm having the largest enhancement. This enhancement decreased when deposition was normalized by u^*, ranging from 17 to 145 % (80 ± 40%), but was still significant based on t-tests of the size-dependent data (only the 0.505 – 0.711 µm range did not show significant difference). Wintertime enhancement of particle dry deposition velocities has been observed in two other particle deposition studies. First, Suni et al. (2003) compiled six years (1996 - 2001) of particle flux measurements (total particle number from 0.014 - 3 µm) over a Scots pine forest in Hyytiälä, Finland, from 1996 to 2001.[12] They hypothesized that the larger wintertime bulk deposition was a result of a larger presence of small particles (< 0.10 µm) having larger deposition velocities, that when included in the integrated total deposition velocity increased wintertime measurement. Second, Rannik et al. (2009) presented particle flux measurements from the same site as Suni et al. (2003) but for 2000 to 2007.[11,12] In contrast to Suni et al., Rannik et al. (2009) noted the same increase in wintertime deposition, but found that the number of nucleation days – on which small particles would dominate – was lowest in the winter. Additionally the continued analysis by Mammarella et al. (2011), indicated that the seasonal changes in geometric mean diameter were inadequate to cause the increased winter deposition rates.[14] Similar to our observations, Mammarella et al. (2011) found that size-dependent deposition velocities were significantly

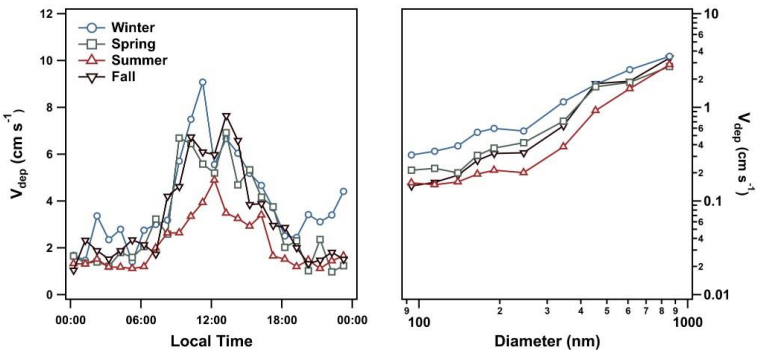

Figure 2.4: Diel cycle of median total particle dry deposition (left), and median size-dependent dry deposition for each season (right).

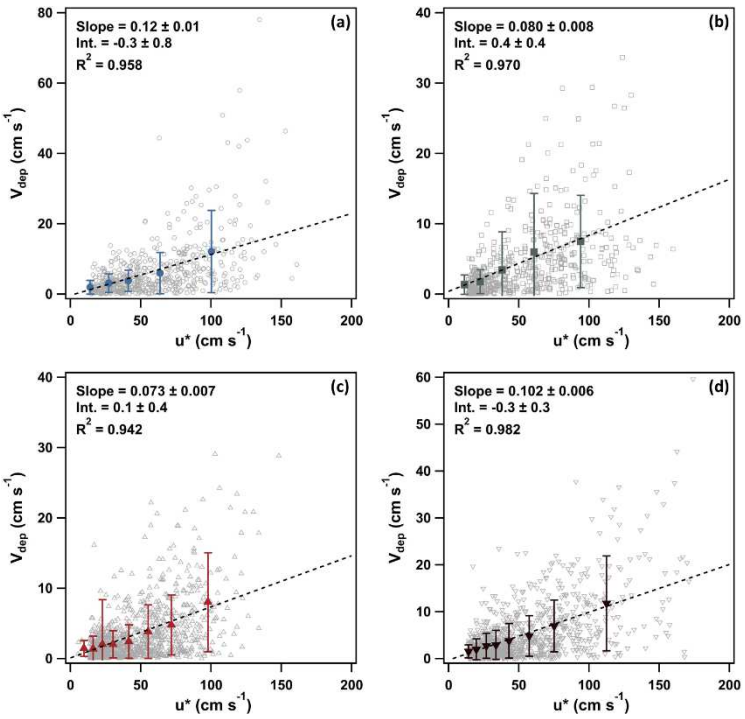

Figure 2.5: Total deposition velocity verses friction velocity (u^*) for the (a) winter, (b) spring, (c) summer, and (d) fall. Grey points are raw data, and the colored markers are mean deposition binned by u^* (each one representing 200 measurement points), with the error bars representing standard deviation.

higher in winter than other seasons. That work concluded that the observed seasonal dependence of the dry deposition was driven by bi-modal distributions in the wintertime.

We investigated the cause of the wintertime increase in deposition during SPiFFY by comparing our results to the resistance model from Emerson et al. (2020), which is based on the work of Zhang et al. (2001) and Slinn (1982).[28,41,42] This model framework was chosen as the base comparison because of its wide use in chemical transport and climate models, including GLOMAP and GEOS-Chem, as well as its ability to assess the roles of Brownian motion, gravitational settling, interception, and impaction. Using measured values u^*, windspeed, temperature, and stability function, we evaluated the ability of the Emerson et al. (2020) model to capture seasonal variation in both total and size-dependent dry deposition (**Figure 2.6**). While the model accurately captured the diel trends for the summer data, there was a clear systematic underestimation of deposition in the other seasons. The largest underestimation was in the winter, when the predicted deposition was ~90% lower than the measured values (**Figure 2S.15**). The size-resolved model predictions clearly disagreed with the measured winter deposition in every size bin. To resolve this disagreement we investigated additional mechanisms that are not currently accounted for in the Emerson et al. (2020) parameterization. Additionally, we explored possible seasonal dependencies for terms that are currently considered, but not parameterized to be seasonally dependent.

Influence of scalar gradients on seasonal deposition velocities

Phoretic effects, which are the drift of particles induced by gradients in scalars such as temperature, water vapor, and electricity, can impact particle movement. The influence of these gradients has been well studied in indoor environments [49], however, their contribution in outdoor forested environments is still uncertain [4,56]. Previous studies have hypothesized that such gradients could impact particle deposition over snow and ice surfaces and impact forested environments during the winter. In their deposition model, Petroff and Zhang (2010) used a constant parameter to describe bulk phoretic effects over ice, snow, and water surfaces; this single phoretic parameter helped resolve differences between measured and modeled deposition velocities.[16] Mammarella et al. (2011) used their

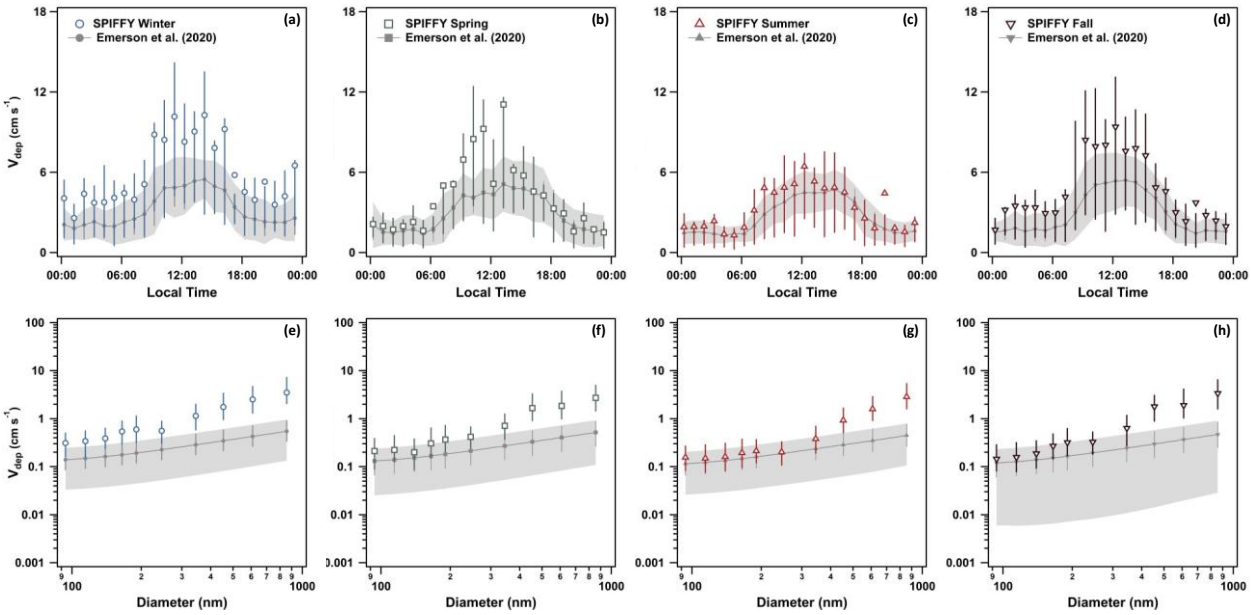

Figure 2.6: Average measured diel deposition velocity compared to the modeled diel deposition for the (a) winter and (b) summer using the resistance model from Emerson et al. (2020). Additionally, seasonal size-dependent deposition trends compared to the model are shown for the (c) winter and (d) summer. For all four plots the modeled deposition is shown as closed grey markers, with shading representing the standard deviation and grey bars representing the interquartile range. Measured average data are represented as open markers with bars representing the interquartile range.

measurements of particles in the Brownian diffusion dominated regime (0.020 – 0.065 μm) to investigate the power law dependency between normalized deposition velocity (V_{dep}/u^*) and the Schmidt number (Sc) and found that this relationship differed for winter versus other seasons.[14] While Mammarella et al. (2011) ultimately concluded that the strong winter deposition velocities must be due seasonal differences in size distribution, they noted that additional factors, such as electrostatic and thermophoretic forces, could contribute to the enhancement of deposition of very small particles. Here, we hypothesized that snow-covered canopies during SPiFFY were affected by phoretic effects – in particular, gradients in temperature or turbulence. We do not consider electrophoresis, as the findings of Tammet el al. (2001) indicate that these gradients only affect 0.01 – 0.2 μm particles above the canopy during low-wind conditions.[17] However, this does not remove electrophoresis from future considerations as the findings are heavily dependent on the electric field strength.

Thermophoretic effects on deposition

We first investigated thermophoresis, which is the drift of particles caused by temperature gradients between the air and collecting surfaces, as a possible driver of the increased winter deposition caused by the low temperatures and the addition of snow to the canopy [57]. We modeled these gradients using measured meteorological parameters along with a simple leaf level energy balance (**Appendix 2B**). This energy balance showed that in the winter, needles were consistently colder than the surrounding air during the day, while temperatures at night were comparable. Specifically, the leaf level energy balance predicted an average gradient of 4 ± 2 K between the leaf and surrounding air. Incorporating the thermophoretic settling velocity with this gradient into the Emerson et al. (2020) deposition model yielded negligible changes in the predicted particle deposition velocity. In the sub-micron size range of interest here, thermophoresis is not strongly correlated to particle size. Unrealistic gradients (15 – 60 K/mm) would be needed for thermophoresis to drive the observed change in size-dependent deposition. Thus, thermophoresis cannot compete with the other drivers of deposition in a needleleaf forest.

Movement of particles by turbophoresis

Discrepancies between models and field observations of particle deposition are common, and often attributed to missing deposition mechanisms [5,7]. Movement of particles from areas of high to low turbulence, or turbophoresis, has been proposed as an important mechanism for dry deposition of particles in the accumulation mode [14,18,19,58]. Two studies successfully integrated a turbophoresis term into a size-resolved dry deposition parameterization. First, Feng (2008) developed a zero-dimensional representation of particle deposition based on the deposition in pipes.[19] In that model, turbophoresis – referred to as the "burst effect of atmospheric eddy turbulence" – is parameterized according to the roughness Reynolds number. Later, Katul et al. (2010) developed a multi-layer model for particle dry deposition.[18] In the Katul model, turbophoresis was parameterized according to the vertical momentum flux, or turbulent stress, and the standard deviation of the vertical velocity. Katul et al. (2010) concluded that the effects of turbophoresis were most prominent for particles between 0.1 and 10 µm above and in the upper layers of the canopy, and that the effects could be neglected for particles < 0.01 µm.

To investigate the effect of turbophoresis on the SPiFFY observations, we used the Katul et al. (2010) parameterization (**Appendix 2A**) because it maintains the minimum in size-dependent deposition velocity, in contrast to the Feng (2008) model. This minimum is a key characteristic of particle deposition that has emerged in recent syntheses of observations [4–6]. However, the Katul parameterization has two components that may result in underestimation of deposition to the canopy. First, the model neglects interception, which has a significant role in deposition over forests. Second, the model relies on the inertial impaction term from Slinn and Slinn (1980), which was formulated for water and smooth surfaces.[59] Katul et al. (2010) acknowledged these as possible reasons for underestimation of particle deposition and recognized the need to further consider "microroughness" of leaves and needles.

Single point calculations of turbophoretic velocity (V_t), following those of Katul et al. (2010), allow us to bound the possible contribution to total deposition. Turbophoretic velocity (V_t) for a 0.1 µm particle (τ_p = 1.4 x 10^{-7} at 298 K) should be ~0.04 cm s^{-1} assuming a u* = 1.0 m s^{-1} and a leaf level

boundary layer thickness of 0.15 mm. This is an order of magnitude lower than our measured deposition velocities for this size range and is therefore expected to be negligible. Using the same assumptions but for a 1 μm particle (τ_p = 5.0 x 10^{-6} at 298 K) we estimate that V_t is ~1.3 cm s^{-1}, potentially resulting in a ~40% increase in the total modeled deposition for particles in that size range. This single point calculation based on the Katul parameterization indicates that turbophoresis may play a role in deposition of larger particles (≥ 1 μm). However, turbophoresis is unlikely to fully explain the seasonal differences observed during SPiFFY as the largest seasonal discrepancies occurred at the lower end of our size range.

To evaluate the impact of turbophoresis over the entire size range and over time while accounting for challenges with the Katul et al. (2010) model, we isolated the turbophoretic collection efficiency from the model and integrated it into the Emerson et al. (2020) parameterization of surface resistance. We present both the resulting deposition velocities (V_{dep}) and surface resistances (R_S) – presented as velocities – from the model with (V_{dep}+ E_{turbo}, R_S+ E_{turbo}) and without (V_{dep}, R_S) turbophoresis in **Figure 2.7a**. As a sensitivity test, we varied the thickness of the viscous sublayer (b) between 5 and 50 mm following Katul et al. (2010). Turbophoresis resulted in large changes for deposition of 1 – 10 μm particles, with larger changes for a thinner viscous sublayer, i.e. when b = 5 (**Figure 2.7a, 2.7b**). The incorporation of turbophoresis resolved some of the initial model-measurement disagreement shown in in Figure 6 for larger particles but had little effect on the model-measurement disagreement at the lower end of the measured size range. Even with the addition of turbophoresis, total deposition in the wintertime was still underpredicted by ~40% (**Figure 2.7c, Figure 2S.16**). Interestingly, inclusion of the turbophoresis term also created a plateau in deposition for particles greater than 10 μm (**Figure 2.8**). This modeled plateau is consistent with a feature frequently noted in size-resolved deposition velocity observations, particularly over needleleaf forests. Saylor et al. (2019) developed an empirical logistic equation to resolve this feature but attributed it to an unknown mechanism.[5] Turbophoresis thus provides a potential mechanism to explain this observed feature in 1 – 10 μm size range. A more critical exploration of the turbophoresis parameterization would be needed to resolve this.

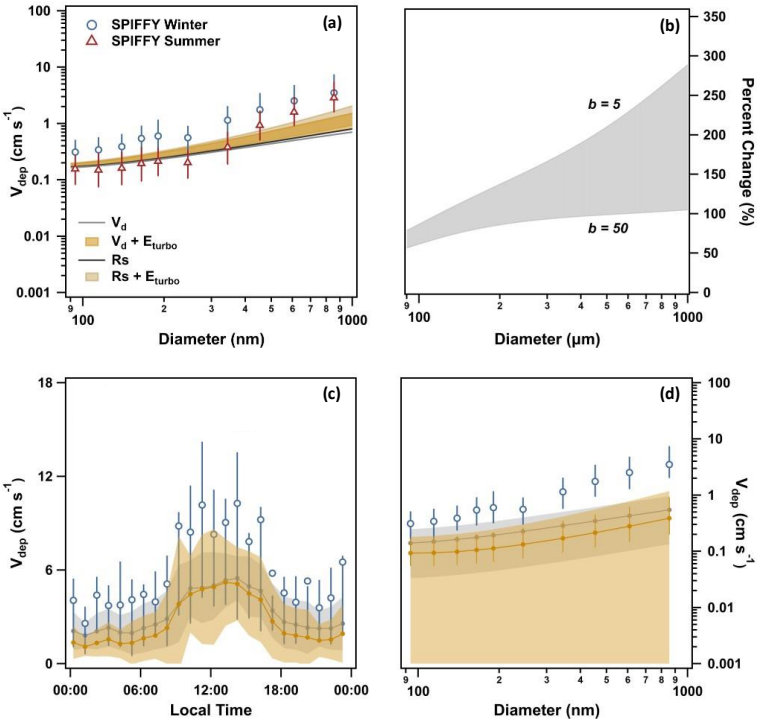

Figure 2.7: (a) Size resolved deposition measured during the winter (blue circles) and summer (red triangle) periods of SPiFFY compared to modeled deposition velocities from Emerson et al. (2020) (V_d; light grey line) versus Emerson et al. (2020) with the inclusion of turbophoresis collection efficiency in the surface resistance term ($V_d + E_{turbo}$; gold shaded region). Surface resistance without turbophoresis (R_s; dark grey line) and with turbophoresis incorporated ($R_s + E_{turbo}$; dark gold shaded region) are shown as velocities. The shaded range shows how the second model formulation changes with the thickness of the viscous sublayer (b); higher deposition values occur at smaller b values. (b) The percent increase in predicted deposition with the addition of turbophoresis is shown as a function of particle size. (c) The average observed (blue circles) versus predicted (shaded range) diel cycle and (d) size-dependent prediction of the model with (grey circles, grey shading) and without (gold circles, gold shading) turbophoresis considered is shown for the winter. The shading represents standard deviation; bars on data points represent the interquartile range.

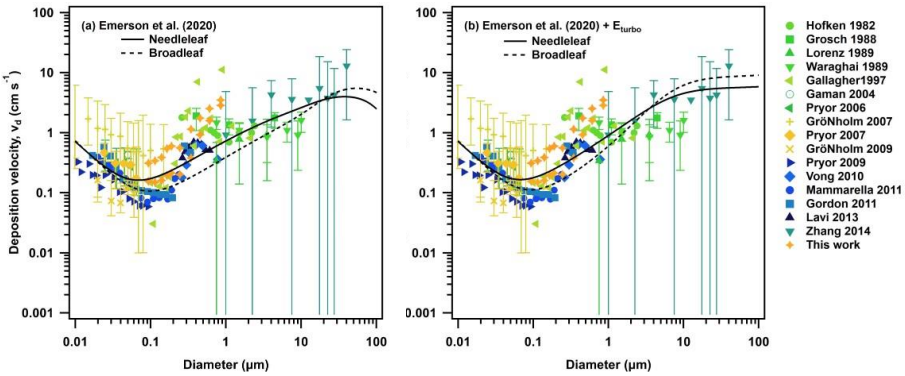

Figure 2.8: Comparison of (a) the Emerson et al. (2020) model alone and (b) the Emerson et al. (2020) model with the turbophoresis collection efficiency (E_{turbo}) from Katul et al. (2010) integrated into the surface resistance (R_s) term. Between the two figured the creation of the plateau above 10 μm from the addition of turbophoresis can clearly be seen.

Both the Emerson et al. (2020) model and the integrated Emerson et al. (2020) with E_{turbo} were compared against literature values for size resolved deposition in forests [14,29,51,53–55,60–69]. The two parameterizations were both comparable to the synthesized literature data, which can be observed in **Figure 2.8**. For these comparisons the models were run for both a needleleaf and broadleaf condition in the midsummer, assuming u^* = 0.5 m s^{-1}, T = 20 °C, and an average wind speed of 3 m s^{-1}.

Influence of snow cover on deposition velocity

Thermophoresis and turbophoresis are not the only hypotheses proposed in the literature to explain seasonal variation in particle deposition velocities. Gallagher et al. (1992) observed a significant decrease in 3 – 31 μm cloud droplet deposition over a snow-covered Sitka spruce canopy.[15] That study used an isolated snow event to observe the effect of snow on deposition and found deposition was two times lower during snow cover. This snow-driven suppression in V_{dep} was attributed to a decrease in surface roughness of the canopy and the subsequent increase of the effective target diameter. Changes in surface roughness from snowfall are not directly accounted for in either the Emerson et al. (2020) or the Zhang et al. (2001) model, and could contribute to model-measurement disagreement.[28,41] In both model parameterizations, roughness length is used to describe surface roughness and is defined with a seasonally variable term. For an evergreen needleleaf forest, the roughness length ranges from 0.8 – 0.9 m, with a drop in the term during the midsummer and transitional spring, but not during the winter period. This approach is consistent with our measured roughness length, which did not vary substantially between seasons. During the spring SPiFFY campaign, we captured an isolated snow period, allowing us to contrast snow-covered fluxes versus prior bare forest surfaces. We observe no significant differences in the total or size-dependent deposition trends during these two periods (**Figure 2.9**), indicating that another mechanism, independent of snow, is driving the increased wintertime deposition velocities.

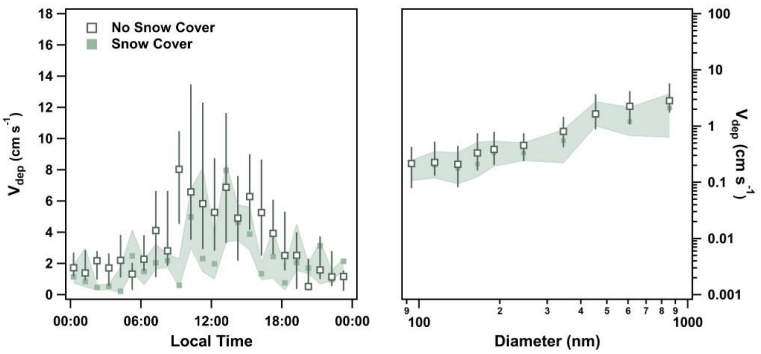

Figure 2.9: Average diel cycle of total deposition velocity (left) and average size-dependent deposition velocity (right) during periods of snow cover (solid green markers with shaded interquartile range) versus no snow cover (open markers with bars representing the interquartile range) from the spring.

The role of interception and changes in the needle surface during the winter

While many deposition studies have proposed alternate mechanisms to explain the numerous model-measurement discrepancies, few have suggested tuning currently considered mechanisms by season. Below we explore aspects of dry deposition mechanisms that could be seasonally dependent. We investigate the extent to which seasonality in certain deposition mechanisms and their associated parameterizations could explain the enhanced wintertime deposition velocities observed at Manitou. We do not consider roughness length (z_0) nor the characteristic radius of the collectors (A); while both terms are well established to be seasonally dependent over deciduous forests, measured roughness length did not vary strongly between seasons at SPiFFY (**Figure 2S.2**) and the characteristic radius for an evergreen needleleaf forest is not expected to change seasonally. We first consider potential seasonality in Brownian diffusion, and then interception.

As discussed above, Mammarella et al. (2011) indicated that deposition of smaller particles (0.020 – 0.065 μm) behaved differently in winter than in other seasons. Because the deposition of these particles is dominated by Brownian diffusion, the group investigated potential seasonality in that term. Following previous work, Mammarella et al. parameterized the Brownian collection efficiency as:

$$E_b = C_b Sc^{-\gamma} \tag{2.16}$$

where C_b and γ are constants. Proposed values for γ have historically been land use dependent but not seasonally dependent. For example, Slinn and Slinn (1980) recommend a γ = 1/2 for water surfaces and Slinn (1982) proposed that γ = 2/3 for vegetated surfaces.[42,59] In the Zhang et al. (2001) and subsequent Emerson et al. (2020) model, γ is also defined as a land use dependent constant ranging from 1/2 to 2/3.[28,41] Mammarella et al. (2011) found that scaling observed deposition velocities with the Schmidt number (Sc) implied a much lower exponential term of γ = 0.36 in the winter, in contrast to γ = 0.66 in other seasons. While the study theorized that this was due to phoretic effects, our analyses above shows that thermo-, electro-, and turbophoretic effects are unlikely to influence particle deposition in this

ultrafine size range (< 0.1 μm) under reasonable wintertime conditions in a similarly structured forest. Thus, while seasonally scaling the constants in Brownian collection efficiency terms decreased model-measurement discrepancy in one instance, there is no mechanistic basis for such a shift – particularly one that only impacts Brownian diffusion related mechanisms. We note that the Schmidt number is the ratio of kinematic viscosity to diffusion coefficients, which do depend on temperature and therefore will change seasonally. However, while the Schmidt number changes by 40 ± 7% from the coldest to warmest conditions at Manitou this only results in an average change of 2 ± 2% in the deposition velocities for our measured size range (**Figure 2S.17**). Further, as our measured particle size range during SPiFFY was larger (0.08 – 1.0 um) than the Mammarella study, merely changing the seasonality of the Brownian diffusion term did not fully account for the observed changes in wintertime data. In fact, applying this scaling to the Emerson et al. (2020) model only caused new problems in model disagreement for the SPiFFY data (**Figure 2S.18**).

The seasonal dependence of interception is typically limited in models to considerations of roughness length and collector radius – but as described above, neither vary substantially enough at Manitou to account for the enhanced wintertime deposition velocities. Plant physiological literature suggests that other aspects of needleleaf forests may undergo seasonal changes that warrant consideration in deposition. Needleleaf plants are efficient at capturing particles [70,71] due to their large available surface area, thick and highly structured epicuticular wax, and high stomatal density [21,23,72]. While surface area of evergreen needleleaf trees is considered independent of season, stomatal conditions are well-established to change with environmental conditions [22,23]. The seasonality and link to particle uptake of the epicuticular wax properties of evergreen needleleaf trees is less well understood, however seasonal changes in needleleaf wax structure have been observed [73] and it has been shown that elevated temperatures can lead to smother wax structures on needles [74] Additionally, the wax can be altered and damaged by uptake of pollutants which has been linked to changes in the plant's particle uptake capacity [75]. Studies of particle loadings collected on evergreen needleleaf trees provide some evidence of

seasonality in particle collection efficiency [21,76–78], but many of these studies lack clear linkages to leaf properties or adequate air concentration data to discern enhanced wintertime deposition velocities, rather than just deposition flux. However, changes in stomatal conditions, epicuticular wax properties, and needle anatomy could be changing the flow of particles around needle surfaces and the collection efficiency of interception. Seasonal changes in plant physiology would trend with interception over other terms because interception is the only mechanism that depends strongly on particle interactions with the collecting surface. In contrast, mechanisms like Brownian motion and impaction both depend on the energy of the particle.

To determine whether seasonal changes in interception collection efficiency could account for enhanced wintertime deposition velocity, we used the Emerson et al. (2020) parameterization first excluding turbophoresis. Doubling the interception constant (C_{in}) from 2.5 to 5 closed the gap between the measured and modeled total and size-resolved deposition (**Figure 2.10, Figure 2S.16**). This increase in the constant indicates that the collection efficiency of interception approximately doubling in the winter. Incorporating both turbophoretic processes and this seasonally adjusted interception constant produces comparable model-measurement agreement as the isolated adjusted interception constant (**Figure 2.10, Figure 2S.16**). However, the isolated increased interception constant produced better size-dependent agreement. The hypothesis that seasonally driven changes in plant physiology enhances particle uptake via interception mechanisms during the winter is consistent with SPiFFY data and can be accounted for with seasonally dependent interception terms.

Conclusions

Significant seasonal changes in particle trends were observed throughout the SPiFFY campaign. Particle concentration, flux, exchange velocity (V_{ex}), and deposition velocity (V_{dep}) all exhibited similar diel trends that varied in magnitude between seasons. The winter had the lowest concentrations and fluxes of particles, yet the highest deposition velocities; the summer had the highest concentrations and fluxes, with the lowest deposition velocities. The spring and fall acted as transition seasons and fell between the

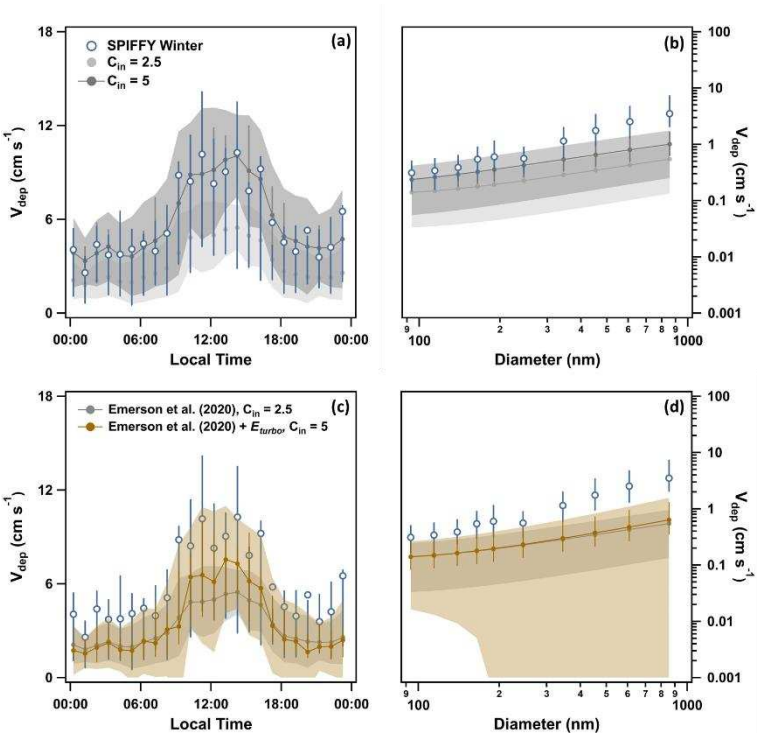

Figure 2.10: Average measured diel deposition velocity compared to the original and adjusted modeled diel deposition for the winter. Additionally, seasonal size-dependent deposition trends compared to the model are shown for the winter. For both plots the modeled deposition is shown as closed grey markers, with shading representing the standard deviation and grey bars representing the interquartile range. Measured average data are represented as open markers with bars representing the interquartile range.

summer and winter trends. These differences extended to the size resolved trends in V_{dep}, with the smaller particles (0.1 – 0.3 µm) having the largest changes between seasons. The commonly-used resistance model approach for particle deposition (e.g. Emerson et al. (2020) revision of Zhang et al. (2001)) accurately described size-resolved V_{dep} and total particle V_{dep} in the summer, but was unable to predict seasonal variation or capture V_{dep} in the winter. Trends for total and size-resolved deposition velocity in the winter, spring, and fall were significantly underestimated by the model. The winter had the largest model disagreement (~90%).

Observation of enhanced deposition velocities during winter is consistent with previous particle flux data collected over forests [11,12,14]. The wintertime enhancement has been attributed to multiple factors, including increases in concentration of larger particles, scalar gradients (thermophoretic and turbophoretic effects) that drive particles towards surfaces, and changes in surface roughness from snow on the canopy [11,14,15]. Changes in leaf physiological properties may also enhance particle uptake. However, our quantitative understanding of the relative impact of these factors is limited [4–6]. This data set provided the unique opportunity to probe the importance of these and other mechanisms in controlling deposition velocity over an evergreen needleleaf canopy across seasons.

The particle size distribution was consistent across seasons and could not explain enhanced wintertime total particle deposition velocity. Seasonal differences in size-resolved V_{dep} further indicated a missing size-dependent deposition mechanism. Using a simple leaf-level energy balance and equations outlined by Salthammer et al. (2011) and Hinds (1999), we ruled out thermophoresis as the source of enhanced V_{dep}.[49,50] We ignored electrophoresis, which has been previously shown to have a negligible influence on deposition to a canopy [17]. Using an isolated snow event during the spring measurement period, we determined snow in the canopy does not change the surface roughness enough to impact deposition mechanisms or account for the observed enhancement in wintertime deposition.

Our analyses show that both turbophoresis and interception can influence dry deposition. Incorporating the turbophoresis collection efficiency term developed by Katul et al. (2010) into Emerson

et al. (2020)'s surface resistance term improved model-measurement comparisons. Turbophoresis has a greater impact on larger particles (closer to 1 μm) than smaller, so is not responsible for the enhanced wintertime deposition velocity. The more interesting result from the incorporation of turbophoresis was the change in shape it created in the predicted size-dependent deposition trend for large particles (10 – 100 μm). The addition created a plateau in this size range, which could help explain the shelf observed in deposition measurements over forests for particles > 10 μm. This range was outside our measured size range, but our results indicate that turbophoresis should be explored further as a mechanism for dry deposition of particles. We hypothesize that interception in the winter is also enhanced by changes in the stomatal conditions and needle structure during the winter. Needle surface structure impacts particle interactions with the surface and therefore uptake, which would be described by the interception efficiency for our measured size range. We account for this factor by increasing the scaling constant for interception in the Emerson et al. (2020) model. This enhancement resolves the wintertime model-measurement discrepancy in deposition velocity and suggests further work into seasonal shifts in plant physiology of evergreen needleleaf trees is warranted. We also note that this could be the result of another mechanism that has a similar size dependence as interception playing a role in wintertime deposition. Overall, these findings support the development and addition of seasonal constants into currently used deposition modules in order to more accurately predict variation in deposition trends, particle lifetime, and the impact of particles on both air quality and radiative properties.

CHAPTER 2 – REFERENCES

(1) Carslaw, K. S.; Lee, L. A.; Reddington, C. L.; Pringle, K. J.; Rap, A.; Forster, P. M.; Mann, G. W.; Spracklen, D. V.; Woodhouse, M. T.; Regayre, L. A.; Pierce, J. R. Large Contribution of Natural Aerosols to Uncertainty in Indirect Forcing. *Nature* **2013**, *503* (7474), 67–71. https://doi.org/10.1038/nature12674.

(2) Lee, L. A.; Carslaw, K. S.; Pringle, K. J.; Mann, G. W. Mapping the Uncertainty in Global CCN Using Emulation. *Atmospheric Chemistry and Physics* **2012**, *12* (20), 9739–9751. https://doi.org/10.5194/acp-12-9739-2012.

(3) Lee, L. A.; Pringle, K. J.; Reddington, C. L.; Mann, G. W.; Stier, P.; Spracklen, D. V.; Pierce, J. R.; Carslaw, K. S. The Magnitude and Causes of Uncertainty in Global Model Simulations of Cloud Condensation Nuclei. *Atmospheric Chemistry and Physics* **2013**, *13* (17), 8879–8914. https://doi.org/10.5194/acp-13-8879-2013.

(4) Farmer, D. K.; Boedicker, E. K.; DeBolt, H. M. Dry Deposition of Atmospheric Aerosols: Approaches, Observations, and Mechanisms. *Annu. Rev. Phys. Chem.* **2021**. https://doi.org/10.1146/annurev-physchem-090519-034936.

(5) Saylor, R. D.; Baker, B. D.; Lee, P.; Tong, D.; Pan, L.; Hicks, B. B. The Particle Dry Deposition Component of Total Deposition from Air Quality Models: Right, Wrong or Uncertain? *Tellus B: Chemical and Physical Meteorology* **2019**, *71* (1), 1550324. https://doi.org/10.1080/16000889.2018.1550324.

(6) Hicks, B. B.; Saylor, R. D.; Baker, B. D. Dry Deposition of Particles to Canopies—A Look Back and the Road Forward. *Journal of Geophysical Research: Atmospheres* **2016**, *121* (24), 14,691-14,707. https://doi.org/10.1002/2015JD024742.

(7) Pryor, S. C.; Gallagher, M.; Sievering, H.; Larsen, S. E.; Barthelmie, R. J.; Birsan, F.; Nemitz, E.; Rinne, J.; Kulmala, M.; Grönholm, T.; Taipale, R.; Vesala, T. A Review of Measurement and Modelling Results of Particle Atmosphere–Surface Exchange. *Tellus B: Chemical and Physical Meteorology* **2008**, *60* (1), 42–75. https://doi.org/10.1111/j.1600-0889.2007.00298.x.

(8) Casquero-Vera, J. A.; Lyamani, H.; Titos, G.; Moreira, G. de A.; Benavent-Oltra, J. A.; Conte, M.; Contini, D.; Järvi, L.; Olmo-Reyes, F. J.; Alados-Arboledas, L. Aerosol Number Fluxes and Concentrations over a Southern European Urban Area. *Atmospheric Environment* **2022**, *269*, 118849. https://doi.org/10.1016/j.atmosenv.2021.118849.

(9) Zhai, J.; Cong, L.; Yan, G.; Wu, Y.; Liu, J.; Wang, Y.; Ma, W.; Zhang, Z. Dry Deposition of Particulate Matter and Ions in Forest at Different Heights. *Int J Environ Res* **2019**, *13* (1), 117–130. https://doi.org/10.1007/s41742-018-0158-z.

(10) Ahlm, L.; Krejci, R.; Nilsson, E. D.; Mårtensson, E. M.; Vogt, M.; Artaxo, P. Emission and Dry Deposition of Accumulation Mode Particles in the Amazon Basin. *Atmospheric Chemistry and Physics* **2010**, *10* (21), 10237–10253. https://doi.org/10.5194/acp-10-10237-2010.

(11) Rannik, Ü.; Mammarella, I.; Aalto, P.; Keronen, P.; Vesala, T.; Kulmala, M. Long-Term Aerosol Particle Flux Observations Part I: Uncertainties and Time-Average Statistics. *Atmospheric Environment* **2009**, *43* (21), 3431–3439. https://doi.org/10.1016/j.atmosenv.2009.02.049.

(12) Suni, T.; Rinne, J.; Reissell, A.; Altimir, N.; Keronen, P.; Rannik, Ü.; Dal Maso, M.; Kulmala, M.; Vesala, T. Long-Term Measurements of Surface Fluxes above a Scots Pine Forest in Hyytiälä, Southern Finland, 1996-2001. *Boreal Env. Res.* **2003**, *8* (4), 287–301.

(13) Petroff, A.; Murphy, J. G.; Thomas, S. C.; Geddes, J. A. Size-Resolved Aerosol Fluxes above a Temperate Broadleaf Forest. *Atmospheric Environment* **2018**, *190*, 359–375. https://doi.org/10.1016/j.atmosenv.2018.07.012.

(14) Mammarella, I.; Rannik, Ü.; Aalto, P.; Keronen, P.; Vesala, T.; Kulmala, M. Long-Term Aerosol Particle Flux Observations. Part II: Particle Size Statistics and Deposition Velocities. *Atmospheric Environment* **2011**, *45* (23), 3794–3805. https://doi.org/10.1016/j.atmosenv.2011.04.022.
(15) Gallagher, M. W.; Beswick, K. M.; Choularton, T. W. Measurement and Modelling of Cloudwater Deposition to a Snow-Covered Forest Canopy. *Atmospheric Environment. Part A. General Topics* **1992**, *26* (16), 2893–2903. https://doi.org/10.1016/0960-1686(92)90281-O.
(16) Petroff, A.; Zhang, L. Development and Validation of a Size-Resolved Particle Dry Deposition Scheme for Application in Aerosol Transport Models. *Geoscientific Model Development* **2010**, *3* (2), 753–769. https://doi.org/10.5194/gmd-3-753-2010.
(17) Tammet, H.; Kimmel, V.; Israelsson, S. Effect of Atmospheric Electricity on Dry Deposition of Airborne Particles from Atmosphere. *Atmospheric Environment* **2001**, *35* (20), 3413–3419. https://doi.org/10.1016/S1352-2310(01)00119-4.
(18) Katul, G. G.; Grönholm, T.; Launiainen, S.; Vesala, T. Predicting the Dry Deposition of Aerosol-Sized Particles Using Layer-Resolved Canopy and Pipe Flow Analogy Models: Role of Turbophoresis. *Journal of Geophysical Research: Atmospheres* **2010**, *115* (D12). https://doi.org/10.1029/2009JD012853.
(19) Feng, J. A Size-Resolved Model and a Four-Mode Parameterization of Dry Deposition of Atmospheric Aerosols. *Journal of Geophysical Research: Atmospheres* **2008**, *113* (D12). https://doi.org/10.1029/2007JD009004.
(20) Pryor, S. C.; Barthelmie, R. J.; Larsen, S. E.; Sørensen, L. L. Ultrafine Particle Number Fluxes over and in a Deciduous Forest. *Journal of Geophysical Research: Atmospheres* **2017**, *122* (1), 405–422. https://doi.org/10.1002/2016JD025854.
(21) He, C.; Qiu, K.; Alahmad, A.; Pott, R. Particulate Matter Capturing Capacity of Roadside Evergreen Vegetation during the Winter Season. *Urban Forestry & Urban Greening* **2020**, *48*, 126510. https://doi.org/10.1016/j.ufug.2019.126510.
(22) Räsänen, J. V.; Yli-Pirilä, P.; Holopainen, T.; Joutsensaari, J.; Pasanen, P.; Kivimäenpää, M. Soil Drought Increases Atmospheric Fine Particle Capture Efficiency of Norway Spruce. *Boreal Env. Res.* **2012**, *17*, 21–30.
(23) Räsänen, J. V.; Holopainen, T.; Joutsensaari, J.; Ndam, C.; Pasanen, P.; Rinnan, Å.; Kivimäenpää, M. Effects of Species-Specific Leaf Characteristics and Reduced Water Availability on Fine Particle Capture Efficiency of Trees. *Environmental Pollution* **2013**, *183*, 64–70. https://doi.org/10.1016/j.envpol.2013.05.015.
(24) Ortega, J.; Turnipseed, A.; Guenther, A. B.; Karl, T. G.; Day, D. A.; Gochis, D.; Huffman, J. A.; Prenni, A. J.; Levin, E. J. T.; Kreidenweis, S. M.; DeMott, P. J.; Tobo, Y.; Patton, E. G.; Hodzic, A.; Cui, Y. Y.; Harley, P. C.; Hornbrook, R. S.; Apel, E. C.; Monson, R. K.; Eller, A. S. D.; Greenberg, J. P.; Barth, M. C.; Campuzano-Jost, P.; Palm, B. B.; Jimenez, J. L.; Aiken, A. C.; Dubey, M. K.; Geron, C.; Offenberg, J.; Ryan, M. G.; Fornwalt, P. J.; Pryor, S. C.; Keutsch, F. N.; DiGangi, J. P.; Chan, A. W. H.; Goldstein, A. H.; Wolfe, G. M.; Kim, S.; Kaser, L.; Schnitzhofer, R.; Hansel, A.; Cantrell, C. A.; Mauldin, R. L.; Smith, J. N. Overview of the Manitou Experimental Forest Observatory: Site Description and Selected Science Results from 2008 to 2013. *Atmospheric Chemistry and Physics* **2014**, *14* (12), 6345–6367. https://doi.org/10.5194/acp-14-6345-2014.
(25) Fulgham, S. R.; Brophy, P.; Link, M.; Ortega, J.; Pollack, I.; Farmer, D. K. Seasonal Flux Measurements over a Colorado Pine Forest Demonstrate a Persistent Source of Organic Acids. *ACS Earth Space Chem.* **2019**, *3* (9), 2017–2032. https://doi.org/10.1021/acsearthspacechem.9b00182.
(26) Cai, Y.; Montague, D. C.; Mooiweer-Bryan, W.; Deshler, T. Performance Characteristics of the Ultra High Sensitivity Aerosol Spectrometer for Particles between 55 and 800nm: Laboratory and Field Studies. *Journal of Aerosol Science* **2008**, *39* (9), 759–769. https://doi.org/10.1016/j.jaerosci.2008.04.007.

(27) Von der Weiden, S. L.; Drewnick, F.; Borrmann, S. Particle Loss Calculator – a New Software Tool for the Assessment of the Performance of Aerosol Inlet Systems. *Atmospheric Measurement Techniques* **2009**, *2* (2), 479–494. https://doi.org/10.5194/amt-2-479-2009.
(28) Emerson, E. W.; Hodshire, A. L.; DeBolt, H. M.; Bilsback, K. R.; Pierce, J. R.; McMeeking, G. R.; Farmer, D. K. Revisiting Particle Dry Deposition and Its Role in Radiative Effect Estimates. *PNAS* **2020**. https://doi.org/10.1073/pnas.2014761117.
(29) Lavi, A.; Farmer, D. K.; Segre, E.; Moise, T.; Rotenberg, E.; Jimenez, J. L.; Rudich, Y. Fluxes of Fine Particles Over a Semi-Arid Pine Forest: Possible Effects of a Complex Terrain. *Aerosol Science and Technology* **2013**, *47* (8), 906–915. https://doi.org/10.1080/02786826.2013.800940.
(30) Pryor, S. C.; Barthelmie, R. J.; Hornsby, K. E. Size-Resolved Particle Fluxes and Vertical Gradients over and in a Sparse Pine Forest. *Aerosol Science and Technology* **2013**, *47* (11), 1248–1257. https://doi.org/10.1080/02786826.2013.831974.
(31) Papale, D.; Reichstein, M.; Aubinet, M.; Canfora, E.; Bernhofer, C.; Kutsch, W.; Longdoz, B.; Rambal, S.; Valentini, R.; Vesala, T.; Yakir, D. Towards a Standardized Processing of Net Ecosystem Exchange Measured with Eddy Covariance Technique: Algorithms and Uncertainty Estimation. *Biogeosciences* **2006**, *3* (4), 571–583. https://doi.org/10.5194/bg-3-571-2006.
(32) Reichstein, M.; Falge, E.; Baldocchi, D.; Papale, D.; Aubinet, M.; Berbigier, P.; Bernhofer, C.; Buchmann, N.; Gilmanov, T.; Granier, A.; Grünwald, T.; Havránková, K.; Ilvesniemi, H.; Janous, D.; Knohl, A.; Laurila, T.; Lohila, A.; Loustau, D.; Matteucci, G.; Meyers, T.; Miglietta, F.; Ourcival, J.-M.; Pumpanen, J.; Rambal, S.; Rotenberg, E.; Sanz, M.; Tenhunen, J.; Seufert, G.; Vaccari, F.; Vesala, T.; Yakir, D.; Valentini, R. On the Separation of Net Ecosystem Exchange into Assimilation and Ecosystem Respiration: Review and Improved Algorithm. *Global Change Biology* **2005**, *11* (9), 1424–1439. https://doi.org/10.1111/j.1365-2486.2005.001002.x.
(33) Foken, Th.; Wichura, B. Tools for Quality Assessment of Surface-Based Flux Measurements. *Agricultural and Forest Meteorology* **1996**, *78* (1), 83–105. https://doi.org/10.1016/0168-1923(95)02248-1.
(34) Wilczak, J. M.; Oncley, S. P.; Stage, S. A. Sonic Anemometer Tilt Correction Algorithms. *Boundary-Layer Meteorology* **2001**, *99* (1), 127–150. https://doi.org/10.1023/A:1018966204465.
(35) Massman, W. J. A Simple Method for Estimating Frequency Response Corrections for Eddy Covariance Systems. *Agricultural and Forest Meteorology* **2000**, *104* (3), 185–198. https://doi.org/10.1016/S0168-1923(00)00164-7.
(36) Billesbach, D. P. Estimating Uncertainties in Individual Eddy Covariance Flux Measurements: A Comparison of Methods and a Proposed New Method. *Agricultural and Forest Meteorology* **2011**, *151* (3), 394–405. https://doi.org/10.1016/j.agrformet.2010.12.001.
(37) Fairall, C. W. Interpretation of Eddy-Correlation Measurements of Particulate Deposition and Aerosol Flux. *Atmospheric Environment (1967)* **1984**, *18* (7), 1329–1337. https://doi.org/10.1016/0004-6981(84)90041-6.
(38) Finkelstein, P. L.; Sims, P. F. Sampling Error in Eddy Correlation Flux Measurements. *Journal of Geophysical Research: Atmospheres* **2001**, *106* (D4), 3503–3509. https://doi.org/10.1029/2000JD900731.
(39) Langford, B.; Acton, W.; Ammann, C.; Valach, A.; Nemitz, E. Eddy-Covariance Data with Low Signal-to-Noise Ratio: Time-Lag Determination, Uncertainties and Limit of Detection. *Atmospheric Measurement Techniques* **2015**, *8* (10), 4197–4213. https://doi.org/10.5194/amt-8-4197-2015.
(40) Deventer, M. J.; Held, A.; El-Madany, T. S.; Klemm, O. Size-Resolved Eddy Covariance Fluxes of Nucleation to Accumulation Mode Aerosol Particles over a Coniferous Forest. *Agricultural and Forest Meteorology* **2015**, *214–215*, 328–340. https://doi.org/10.1016/j.agrformet.2015.08.261.
(41) Zhang, L.; Gong, S.; Padro, J.; Barrie, L. A Size-Segregated Particle Dry Deposition Scheme for an Atmospheric Aerosol Module. *Atmospheric Environment* **2001**, *35* (3), 549–560. https://doi.org/10.1016/S1352-2310(00)00326-5.

(42) Slinn, W. G. N. Predictions for Particle Deposition to Vegetative Canopies. *Atmospheric Environment (1967)* **1982**, *16* (7), 1785–1794. https://doi.org/10.1016/0004-6981(82)90271-2.
(43) Finnigan, J. Turbulence in Plant Canopies. *Annu. Rev. Fluid Mech.* **2000**, *32*, 519–571. https://doi.org/10.1146/annurev.fluid.32.1.519.
(44) Poggi, D.; Porporato, A.; Ridolfi, L.; Albertson, J. D.; Katul, G. G. The Effect of Vegetation Density on Canopy Sub-Layer Turbulence. *Boundary-Layer Meteorology* **2004**, *111* (3), 565–587. https://doi.org/10.1023/B:BOUN.0000016576.05621.73.
(45) Monteith, J. L.; Unsworth, M. H. *Principles of Environmental Physics: Plants, Animals, and the Atmosphere*, 2nd ed.; Edward Arnold: London, 1990.
(46) Sridhar, V.; Elliott, R. L. On the Development of a Simple Downwelling Longwave Radiation Scheme. *Agricultural and Forest Meteorology* **2002**, *112* (3), 237–243. https://doi.org/10.1016/S0168-1923(02)00129-6.
(47) Jones, H. G. *Plants and Microclimate: A Quantitative Approach to Environmental Plant Physiology*, 3rd ed.; Cambridge University Press: Cambridge, United Kingdom, 2013. https://doi.org/10.1017/CBO9780511845727.
(48) Frank, J. M.; Fornwalt, P. J.; Asherin, L. A.; Alton, S. K. *Manitou Experimental Forest Hourly Meteorology Data*, 3rd ed.; Forest Service Research Data Archive: Fort Collins, CO, 2021.
(49) Salthammer, T.; Fauck, C.; Schripp, T.; Meinlschmidt, P.; Willenborg, S.; Moriske, H.-J. Effect of Particle Concentration and Semi-Volatile Organic Compounds on the Phenomenon of 'Black Magic Dust' in Dwellings. *Building and Environment* **2011**, *46* (10), 1880–1890. https://doi.org/10.1016/j.buildenv.2011.03.008.
(50) Hinds, W. C. *Aerosol Technology: Properties, Behavior, and Measurement of Airborne Particles*, 2nd ed.; John Wiley & Sons, Inc.: New York, NY, 1999.
(51) Vong, R. J.; Vong, I. J.; Vickers, D.; Covert, D. S. Size-Dependent Aerosol Deposition Velocities during BEARPEX'07. *Atmospheric Chemistry and Physics* **2010**, *10* (12), 5749–5758. https://doi.org/10.5194/acp-10-5749-2010.
(52) Grönholm, T.; Launiainen, S.; Ahlm, L.; Mårtensson, E. M.; Kulmala, M.; Vesala, T.; Nilsson, E. D. Aerosol Particle Dry Deposition to Canopy and Forest Floor Measured by Two-Layer Eddy Covariance System. *Journal of Geophysical Research: Atmospheres* **2009**, *114* (D4). https://doi.org/10.1029/2008JD010663.
(53) GröNholm, T.; Aalto, P. P.; Hiltunen, V. J.; Rannik, Ül.; Rinne, J.; Laakso, L.; HyvöNen, S.; Vesala, T.; Kulmala, M. Measurements of Aerosol Particle Dry Deposition Velocity Using the Relaxed Eddy Accumulation Technique. *Tellus B: Chemical and Physical Meteorology* **2007**, *59* (3), 381–386. https://doi.org/10.1111/j.1600-0889.2007.00268.x.
(54) Gallagher, M. W.; Beswick, K. M.; Duyzer, J.; Westrate, H.; Choularton, T. W.; Hummelshøj, P. Measurements of Aerosol Fluxes to Speulder Forest Using a Micrometeorological Technique. *Atmospheric Environment* **1997**, *31* (3), 359–373. https://doi.org/10.1016/S1352-2310(96)00057-X.
(55) Lorenz, R.; Murphy, C. E. Dry Deposition of Particles to a Pine Plantation. *Boundary-Layer Meteorol* **1989**, *46* (4), 355–366. https://doi.org/10.1007/BF00172241.
(56) Petroff, A.; Mailliat, A.; Amielh, M.; Anselmet, F. Aerosol Dry Deposition on Vegetative Canopies. Part I: Review of Present Knowledge. *Atmospheric Environment* **2008**, *42* (16), 3625–3653. https://doi.org/10.1016/j.atmosenv.2007.09.043.
(57) Batchelor, G. K.; Shen, C. Thermophoretic Deposition of Particles in Gas Flowing over Cold Surfaces. *Journal of Colloid and Interface Science* **1985**, *107* (1), 21–37. https://doi.org/10.1016/0021-9797(85)90145-6.
(58) Katul, G. G.; Poggi, D. The Influence of Hilly Terrain on Aerosol-Sized Particle Deposition into Forested Canopies. *Boundary-Layer Meteorol* **2010**, *135* (1), 67–88. https://doi.org/10.1007/s10546-009-9459-2.
(59) Slinn, S. A.; Slinn, W. G. N. Predictions for Particle Deposition on Natural Waters. *Atmospheric Environment (1967)* **1980**, *14* (9), 1013–1016. https://doi.org/10.1016/0004-6981(80)90032-3.

(60) Zhang, J.; Shao, Y.; Huang, N. Measurements of Dust Deposition Velocity in a Wind-Tunnel Experiment. *Atmospheric Chemistry and Physics* **2014**, *14* (17), 8869–8882. https://doi.org/10.5194/acp-14-8869-2014.
(61) Gordon, M.; Staebler, R. M.; Liggio, J.; Vlasenko, A.; Li, S.-M.; Hayden, K. Aerosol Flux Measurements above a Mixed Forest at Borden, Ontario. *Atmospheric Chemistry and Physics* **2011**, *11* (14), 6773–6786. https://doi.org/10.5194/acp-11-6773-2011.
(62) Grönholm, T.; Launiainen, S.; Ahlm, L.; Mårtensson, E. M.; Kulmala, M.; Vesala, T.; Nilsson, E. D. Aerosol Particle Dry Deposition to Canopy and Forest Floor Measured by Two-Layer Eddy Covariance System. *Journal of Geophysical Research: Atmospheres* **2009**, *114* (D4). https://doi.org/10.1029/2008JD010663.
(63) Pryor, S. C.; Larsen, S. E.; Sørensen, L. L.; Barthelmie, R. J.; Grönholm, T.; Kulmala, M.; Launiainen, S.; Rannik, Ü.; Vesala, T. Particle Fluxes over Forests: Analyses of Flux Methods and Functional Dependencies. *Journal of Geophysical Research: Atmospheres* **2007**, *112* (D7). https://doi.org/10.1029/2006JD008066.
(64) Pryor, S. C.; Barthelmie, R. J.; Spaulding, A. M.; Larsen, S. E.; Petroff, A. Size-Resolved Fluxes of Sub-100-Nm Particles over Forests. *Journal of Geophysical Research: Atmospheres* **2009**, *114* (D18). https://doi.org/10.1029/2009JD012248.
(65) Pryor, S. C. Size-Resolved Particle Deposition Velocities of Sub-100nm Diameter Particles over a Forest. *Atmospheric Environment* **2006**, *40* (32), 6192–6200. https://doi.org/10.1016/j.atmosenv.2006.04.066.
(66) Gaman, A.; Rannik, Ü.; Aalto, P.; Pohja, T.; Siivola, E.; Kulmala, M.; Vesala, T. Relaxed Eddy Accumulation System for Size-Resolved Aerosol Particle Flux Measurements. *J. Atmos. Oceanic Technol.* **2004**, *21* (6), 933–943. https://doi.org/10.1175/1520-0426(2004)021<0933:REASFS>2.0.CO;2.
(67) Waraghai, A.; Gravenhorst, G. Dry Deposition of Atmoshperic Particles to an Old Spruce Stand. In *Mechanisms and Effects of Pollutant-Transfer into Forests: Proceedings of the Meeting on Mechanisms and Effects of Pollutant-Transfer into Forests, held in Oberursel/Taunus, F.R.G., November 24–25, 1988*; Georgii, H.-W., Ed.; Springer Netherlands: Dordrecht, 1989; pp 77–86. https://doi.org/10.1007/978-94-009-1023-2_9.
(68) Grosch, S.; Schmitt, G. Experimental Investigations on the Deposition of Trace Elements in Forest Areas. In *Environmental Meteorology: Proceedings of an International Symposium held in Würzburg, F.R.G., 29 September – 1 October 1987*; Grefen, K., Löbel, J., Eds.; Springer Netherlands: Dordrecht, 1988; pp 201–216. https://doi.org/10.1007/978-94-009-2939-5_15.
(69) Höfken, K. D.; Gravenhorst, G. Deposition of Atmospheric Aerosol Particles to Beech- and Spruce Forest. In *Deposition of Atmospheric Pollutants: Proceedings of a Colloquium held at Oberursel/Taunus, West Germany, 9–11 November 1981*; Georgii, H.-W., Pankrath, J., Eds.; Springer Netherlands: Dordrecht, 1982; pp 191–194. https://doi.org/10.1007/978-94-009-7864-5_19.
(70) Beckett, K. P.; Freer-Smith, P. H.; Taylor, G. Urban Woodlands: Their Role in Reducing the Effects of Particulate Pollution. *Environmental Pollution* **1998**, *99* (3), 347–360. https://doi.org/10.1016/S0269-7491(98)00016-5.
(71) Beckett, K. P.; Freer-Smith, P. H.; Taylor, G. Particulate Pollution Capture by Urban Trees: Effect of Species and Windspeed. *Global Change Biology* **2000**, *6* (8), 995–1003. https://doi.org/10.1046/j.1365-2486.2000.00376.x.
(72) Sæbø, A.; Popek, R.; Nawrot, B.; Hanslin, H. M.; Gawronska, H.; Gawronski, S. W. Plant Species Differences in Particulate Matter Accumulation on Leaf Surfaces. *Science of The Total Environment* **2012**, *427–428*, 347–354. https://doi.org/10.1016/j.scitotenv.2012.03.084.
(73) Altieri, A.; Del Caldo, L.; Manes, F. Morphology of Epicuticular Waxes in Pinus Pinea Needles in Relation to Season and Pollution-Climate. *European Journal of Forest Pathology* **1994**, *24* (2), 79–91. https://doi.org/10.1111/j.1439-0329.1994.tb01061.x.

(74) Apple, M. E.; Olszyk, D. M.; Ormrod, D. P.; Lewis, J.; Southworth, D.; Tingey, D. T. Morphology and Stomatal Function of Douglas Fir Needles Exposed to Climate Change: Elevated CO2 and Temperature. *International Journal of Plant Sciences* **2000**, *161* (1), 127–132. https://doi.org/10.1086/314237.
(75) Burkhardt, J.; Pariyar, S. Particulate Pollutants Are Capable to 'Degrade' Epicuticular Waxes and to Decrease the Drought Tolerance of Scots Pine (Pinus Sylvestris L.). *Environmental Pollution* **2014**, *184*, 659–667. https://doi.org/10.1016/j.envpol.2013.04.041.
(76) Zha, Y.; Shi, Y.; Tang, J.; Liu, X.; Feng, C.; Zhang, Y. Spatial-Temporal Variability and Dust-Capture Capability of 8 Plants in Urban China. *Pol. J. Environ. Stud.* **2018**, *28* (1), 453–462. https://doi.org/10.15244/pjoes/81679.
(77) Zhang, Z.; Liu, J.; Wu, Y.; Yan, G.; Zhu, L.; Yu, X. Multi-Scale Comparison of the Fine Particle Removal Capacity of Urban Forests and Wetlands. *Sci Rep* **2017**, *7* (1), 46214. https://doi.org/10.1038/srep46214.
(78) Freer-Smith, P. H.; Beckett, K. P.; Taylor, G. Deposition Velocities to Sorbus Aria, Acer Campestre, Populus Deltoides × Trichocarpa 'Beaupré', Pinus Nigra and × Cupressocyparis Leylandii for Coarse, Fine and Ultra-Fine Particles in the Urban Environment. *Environmental Pollution* **2005**, *133* (1), 157–167. https://doi.org/10.1016/j.envpol.2004.03.031.

CHAPTER 3 - BOUNDING DRY DEPOSITION OF PARTICULATE MATTER AND BLACK CARBON IN THE LOW ARCTIC [4]

Chapter Overview

Understanding particle lifetime is critical for bounding the impacts of aerosols in the rapidly changing Arctic environment. Particle removal through dry deposition has a direct impact on short- and long-range transport of aerosols, concentrations of cloud condensation nuclei, and aerosol impacts on cloud albedo and lifetime. Currently, direct observations of dry deposition in the Arctic are scarce which makes constraining current models difficult. We present new measurements of total particle and black carbon (BC) deposition as well as size-resolved particle dry deposition from the low Arctic. Total particle and BC deposition were 0.13 cm s^{-1} and 0.85 cm s^{-1} respectively and were strongly dependent on the measured friction velocity. Size-dependent velocities showed a minimum around 0.13 μ. Current resistance models of dry deposition were unable to capture the observed trend, however, removing the assumption of a flat surface by incorporating an interception term resulted in substantial improvements in model measurement agreement in this work. We hypothesize that this could indicate the misclassification of a snow-covered tundra as a flat surface, which leads to an overestimation of particle lifetime and impacts.

Introduction

The Arctic is a rapidly changing environment that is warming two to three times faster than the rest of the globe[1]. This phenomenon is known as arctic amplification. Factors controlling this accelerated warming are poorly constrained, which stems from our lack of ability to predict regional feedback processes in the Arctic[2,3]. The two most important feedbacks for arctic amplification are that of temperature and albedo[2]. Aerosols play a critical role in these feedbacks through direct, scattering and

[4] This manuscript is currently being drafted and further analysis is still in progress. All analysis presented here was done by E.K. Boedicker and led by D.K.Farmer.

absorbing radiation, and indirect effects, acting as cloud condensation nuclei (CCN) and determining cloud albedo and lifetime[4,5]. The magnitude of these effects in the arctic are dependent upon local environmental conditions, long-range transport of aerosols, and the lifetime of aerosols[6].

Aerosol lifetime is determined by its rate of removal through wet and dry deposition. Wet deposition is the scavenging of particles and subsequent removal by precipitation and dry deposition is the removal of particles through interactions with terrestrial surfaces[7]. The relative contribution of each of these removal pathways has been observed to be seasonal in the arctic, with wet deposition playing a larger role in the warmer months and dry deposition having a higher impact in the winter[8–10]. This seasonality was clearly shown in measurements taken by Macdonald et al. (2017) over a ten-month period in Alert, Canada, where black carbon, ammonium, and sulfate aerosol deposition rates were all within the predicted range for dry deposition in the winter but increased significantly in the spring and fall[10]. Constraining these trends through observations is critical for bounding the role of aerosols in the arctic and improving models. Eckhardt et al. (2015) identified aerosol removal processes in the arctic and lower latitudes as the largest cause in variation between models and improving deposition schemes has led to improvements in predicting the seasonal aerosol cycle in the arctic[11–13].

Dry deposition of accumulation mode aerosols (0.1 – 1 μm) is of particular interest as it has been identified as the largest source of uncertainty in the prediction of CCN concentrations and the prediction of aerosol impacts on cloud albedo in global models[14,15]. Schmale et al. (2021) identified these process, along with others that dry deposition has a critical impact on, as key measurement and modeling gaps in understanding arctic aerosols[16]. However, there are few measurements of size-resolved dry deposition in the cryosphere that can be used to improve and constrain dry deposition predictions[17–22]. This work presents new measurements of size-resolved deposition for accumulation mode aerosols taken as part of a two-month campaign in Utqiagvik, Alaska, USA, that we use to constrain dry deposition in the Arctic and evaluate model representations.

Methods

Site Description

The Arctic Black Carbon and Aerosol Deposition Study (ArcticBCADS) was conducted at the Atmospheric Radiation Monitoring (ARM) facility's North Slope of Alaska (NSA) site in Utqiagvik (formally Barrow), Alaska, USA. A particle flux measurement system was installed at the site's meteorological tower (71.324°N, 156.615°W), a 40 m triangular tower (**Figure 3.1**). Measurements took place from September 9 to October 24, 2021. NSA is classified as a coastal tundra and its surface variability and complex composition of vegetation has been well characterized in other work [23,24]. The dominant vegetation includes various sedge species (*Carex aquatillis, Eriophorum russeolum,* and *Eriophorum angustifolium*), tundragrass (*Dupontia fisheri*), and pendant grass (*Arctophila fulva*), as well as various moss and lichens [23]. Canopy height was near zero throughout the campaign, the average vegetation height has been reported to be 17 ± 8 cm during periods with no snow cover[23].

Instrumentation

Size-resolved particle concentrations were measured by an Ultra-High Sensitivity Aerosol Spectrometer (UHSAS; DMT Inc., Longmont, CO)[25]. The UHSAS is an optical measurement system that quantify size-dependent scatter and contains a 1054 nm solid-state Nd^{3+}:Y LiF4 laser. The UHSAS was configured to a 10 Hz time resolution and counted particles in 99 size bins (0.06 – 1 µm). Data were re-binned during processing – where finer resolution bins were combined over new size ranges – to minimize the error caused by the low counts during the campaign. Instrument zeros and calibrations were done weekly throughout the campaign using HEPA filters and NIST standard polystyrene latex spheres (0.10 – 0.90 µm mobility diameter).

Refractory black carbon (rBC) was measured using a Single-Particle Soot Photometer (SP2, eight-channel, Model D; DMT Inc., Longmont, CO)[26,27]. The SP2 quantifies both thermal visible radiation emitted from rBC particles after induced incandescence and size-dependent scatter from a 1064 nm

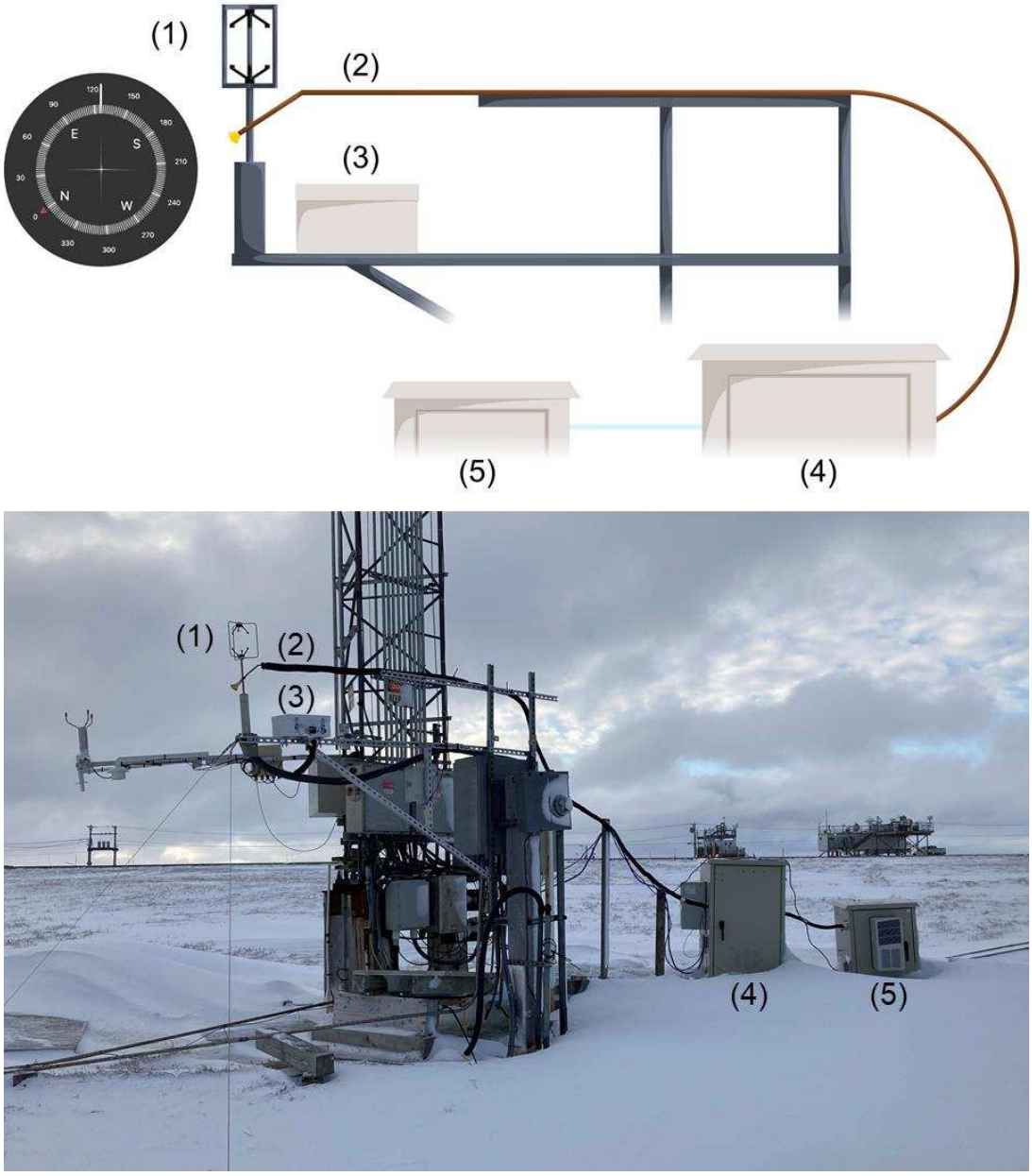

Figure 3.1: Schematic of the flux measurement system set-up. (1) The sonic anemometer was mounted at the front of the boom, 125 CCW off North. (2) A copper inlet was run from the sonic, where it was protected from rain and other precipitation using a small funnel, to the instrument enclosure (4). The POPS (3) was mounted to the boom behind the sonic, while the UHSAS and SP2 were housed in a temperature-controlled instrument enclosure (4). At the end of the line a backing pump, housed in a second temperature-controlled enclosure (5), maintained turbulence in the main line.

continuous-wave Nd:YAG laser. Instrument zeros and PSL checks were done in tandem with those preformed for the UHSAS throughout the campaign. Instrument response to size-selected fullerene soot by a Differential Mobility Analyzer (DMA) was measured at the beginning and end of the campaign. We calibrated for rBC in the mass range of 0.3 – 50 fg (70 to 600 nm mobility diameter). Calibrations for the SP2 can be found in the supplemental (**Figure 3S.1**).

A sonic anemometer (WindMaster Pro; Gill Instruments) and inlet were mounted to a boom that extended 6ft from the tower and 3.7 m above ground level (**Figure 3.1**). The inlet was oriented downward (~45°) and protected from precipitation using a funnel with a mesh screen. Inlet displacement from the center of the sonic was 0.3 m in the vertical direction. The SP2, UHSAS, and backing pump were housed in temperature-controlled enclosures at the base of the tower. The inlet was 6.4 m (ID: 7 mm) of copper tubing with no sharp bends. A bypass pump and critical orifice maintained a turbulent flow of ~15 LPM through the main line (Re ≈ 2900; 0.96 s residence time), while laminar flow was maintained within the internal tubing of the SP2 and UHSAS. Particle losses caused by transport through the bypass were determined to be negligible (< 5%) for the particle ranges measured by our instruments. All instruments were time synced using the network time protocol (NTP) time server, with the clock on the SP2 set as the internal standard for all the instruments.

Eddy-Covariance Measurements

The eddy covariance method for measuring surface-atmosphere exchange expresses the flux of a scalar (F_c), like concentration (c), as the covariance between the scalar and the vertical wind speed (w):

$$F_c = \overline{w'c'} = \frac{1}{N}\sum_{i=0}^{N}(c_i - \bar{c})\,(w_i - \bar{w}) \tag{3.1}$$

where n is the number of measurement points in a flux period, w_i and c_i are the instantaneous measurements of the vertical windspeed and particle concentration respectively, and $\bar{w}$ and $\bar{c}$ are the mean values. Typically, fluxes are analyzed over a 30-minute period to ensure that the analysis is capturing

small scale cycles. The eddy covariance method relies on well-developed turbulence and requires that concentration be in steady state during the 30-min period.

Eddy covariance analysis was run initially on the Arctic BCADS data, and several quality controls were enforced on the data based on u^*, stationarity, wind direction, and precipitation events. Flux periods where turbulence was not well developed with a friction velocity (u^*) < 0.14 m/s [28,29], where measured concentration did not meet the steady state assumption [30], where the direction of the wind was obstructed by the meteorology tower (166 – 203 °CW), and times when precipitation events occurred were all excluded from analysis. These filters resulted in the loss of approximately 90% of measured flux periods, with stationarity being the leading driver of measurement losses (**Table 3.1**).

Wavelet Analysis

Wavelet analysis decomposes a measured signal into a series of frequencies while preserving its time localization [31–33]. This method allows us to map a time series into a time and frequency space making it possible to evaluate fluxes over shorter time scales (e.g. 1-min vs 30-min flux estimates). Additionally, while wavelet analysis still requires well developed turbulence, it does not require a steady state assumption which leads to the preservation of a larger portion of data compared to the eddy covariance method. Turbulent flux in wavelet analysis (F_w) is defined as the sum of the real part of the cross-wavelet spectrum (E_{cw}) over all scales (j):

$$F_w = \delta j \sum_{j=0}^{J} \frac{E_{cw}(j)}{s_j} \tag{3.2}$$

$$E_{cw} = \frac{\delta t}{R} \frac{1}{N} \sum_{n=0}^{N-1} \left[W_n^c(s_j) \, W_n^{*w}(s_j) \right] \tag{3.3}$$

In Eq. 3.2 and 3.3, j is the scale index, δj is the scale step size (in this work $\delta j = 0.25$), J is the maximum number of scales (based on the wavelet), and s_j is the scale value which is defined as fractional powers of two:

Table 3.1: Summary of quality control tests for the Arctic BCADS campaign. Number of flux periods impacted, as well as the percent of the total available measurements, are presented for each test and each season. The final rows list the number of flux periods available after quality control for both the eddy-covariance method (EC) and the wavelet analysis.

	September (N=819)	**October** (N=958)	**Total Campaign** (N=1777)
Stationarity†	635 (77%)	746 (78%)	1381 (78%)
u^*	102 (12%)	210 (22%)	312 (18%)
Wind direction	153 (19%)	228 (24%)	381 (21%)
Precipitation	75 (9%)	47 (5%)	122 (7%)
EC Flux Periods	**122 (15%)**	**92 (10%)**	**214 (12%)**
Wavelet Flux Periods	**515 (63%)**	**467 (49%)**	**982 (55%)**

†Only applied to the EC data.

$$s_j = s_0\, 2^{j\,\delta j} \tag{3.4}$$

The smallest resolvable scale (s_0) is defined as:

$$s_0 = 2\,\delta t \tag{3.5}$$

Additionally, in the equations above, δt is the data frequency in the time series and *N* is the number of data points in the portion of the time series being considered. The *R* term is the reconstruction factor, and it is dependent on the type of wavelet used in the transform [33]. Both $W_n^c(s_j)$ and $W_n^{*w}(s_j)$ are the wavelet transforms of the concentration (c) and vertical wind component (w) time series, with the asterisk (*) indicating the complex conjugate of the transform.

$$W_n(s_j, n) = \sum_{n'=0}^{N-1} x_{n'}\, \psi^* \left[\frac{(n'-n)\,\delta t}{s_j}\right] \tag{3.6}$$

Eq. 6 shows the continuous wavelet transform at a scale (s_j), defined as the convolution of the time series $x(t)$ with the scaled and translated version of a wavelet function (ψ), where *n* is the localized time index and the asterisk (*) again indicating the complex conjugate.

In this work we used the Ricker wavelet (ψ^R), based on the second derivative of the gaussian probability density function. This follows similar work that also uses this wavelet to evaluate turbulent flux measurements [31,34]. Formulation for the Ricker wavelet is as follows [31]:

$$\psi^R(u) = \frac{2\left(1-\frac{u^2}{\sigma^2}\right) e^{-\frac{u^2}{2\sigma}}}{\pi^{1/4}\sqrt{3\,\sigma}} \tag{3.7}$$

This analysis was verified through direct comparisons with the quality-controlled eddy covariance results (**Figure 3.2**), and resulted in the retention of 55% of the available measurement points (**Table 3.1**)

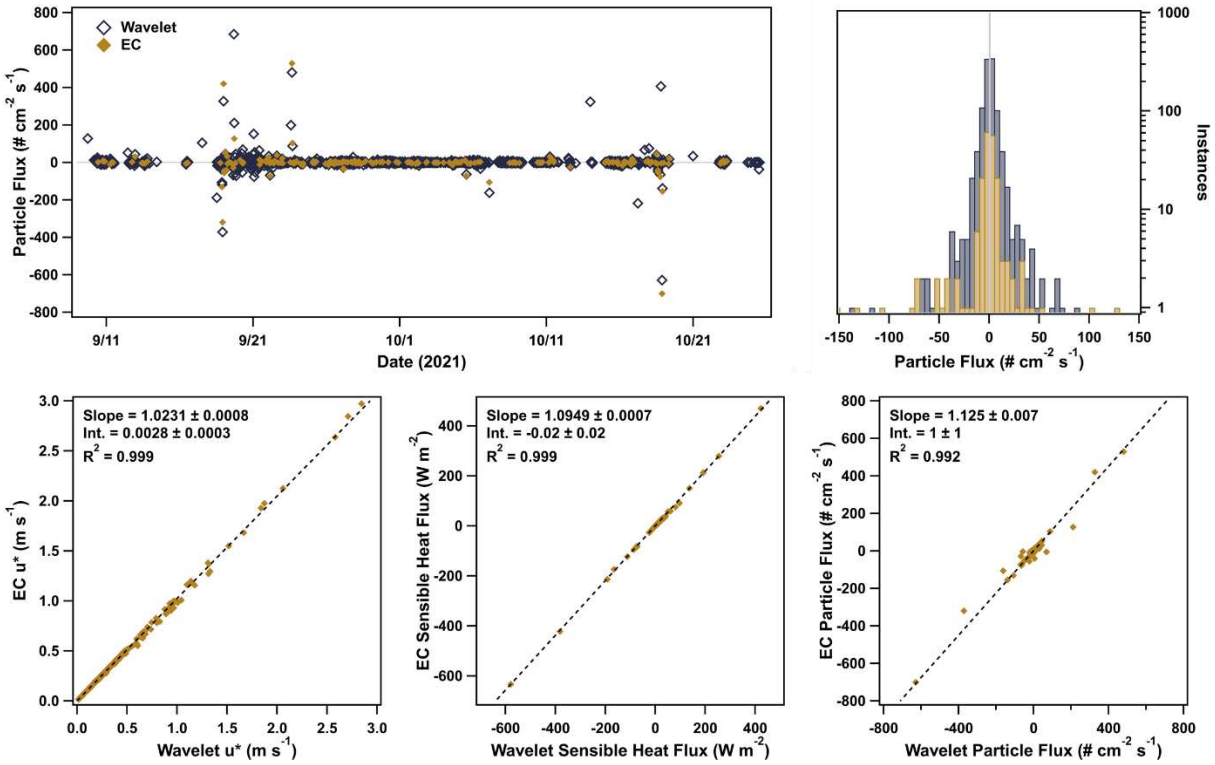

Figure 3.2: Comparison of particle flux and other parameters calculated using wavelet analysis (dark blue) and the covariance method (golden). The top left panel shows a time series comparing the calculated total particle flux, with wavelet results represented by open diamonds and eddy-covariance results represented by closed diamonds. The top right panel shows the distribution of positive and negative fluxes for both methods. The bottom panels show direct comparisons of the covariance method and wavelet method for the calculation of friction velocity (left), sensible heat flux (middle), and total particle flux (right).

Results and Discussion

Total particle and black carbon deposition

Following the convention of previous particle flux measurements in the Arctic, negative flux values were taken to indicate deposition[19,21]:

$$V_{dep} = -\frac{F_c}{\bar{c}} \tag{3.8}$$

where F_c is the flux and $\bar{c}$ is the mean concentration during the flux period. Median deposition velocities for all particles and refractory black carbon in our measured size range was $V_{dep,N}$ = 0.13 cm s^{-1} and $V_{dep,rBC}$ = 0.85 cm s^{-1}. The binned velocities correlated strongly with friction velocity (u*), and u* normalized median deposition velocities were $V_{dep,N}/u$* = 0.0056 cm s^{-1} and $V_{dep,rBC}/u$* = 0.033 cm s^{-1} (**Figure 3.3**). Deposition velocities did not have strong diel trends (**Figure 3.3**), following the breakdown in normally observed trends for parameters that follow solar heating cycles as hours of daylight were rapidly decreasing in Utqiagvik during the campaign period (**Figure 3S.2**, **3S.3**).

These velocities are somewhat elevated compared to previous observations over snow and ice surfaces[10,17–19]. For example, Nilsson and Rannik (2001) measured deposition velocities ranging from 0.026 – 0.073 cm s^{-1} over smooth ice surfaces and open leads in the high Arctic using the eddy-covariance method[19]. In contrast, our measurements agree well with the eddy-covariance results of Grönlund et al. (2002) who report median deposition velocities of 0.33 and 0.80 cm s^{-1} over a smooth snow-covered and rocky area in Dronning Maud Land, Antarctica[21]. Both of these studies used condensation particle counters that measured particles from 0.01 – 3 µm. Interestingly, while the magnitude of the measured deposition exceeded that reported by Macdonald et al. (2017), our measurement period from September to October did align with months the study identified as having higher deposition velocities compared to other winter months. Placing our measurements in line with previously observed trends in Arctic aerosol deposition.

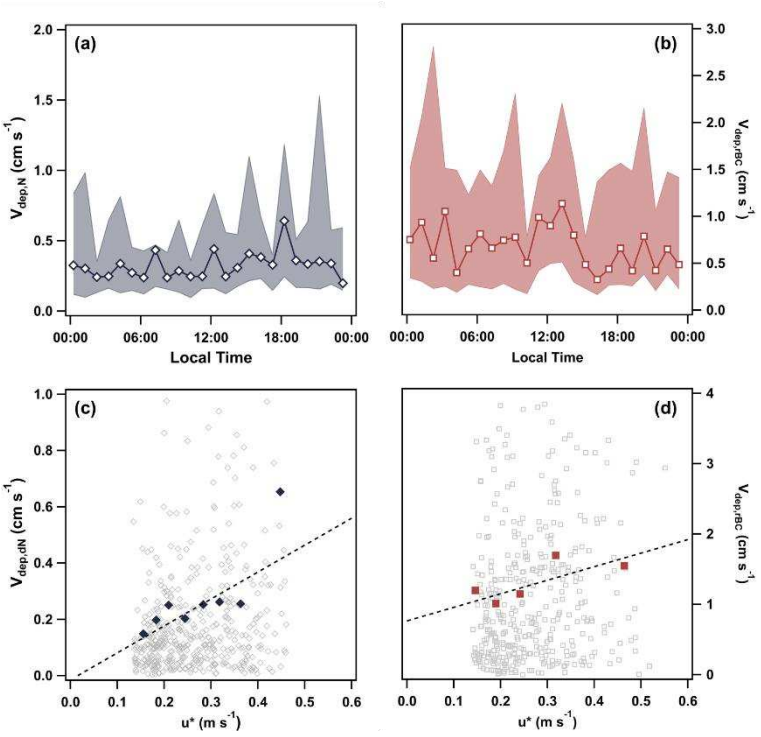

Figure 3.3: Average diel deposition velocity for (a) particles and (b) BC over the entire measured size range. And the total deposition velocity verses friction velocity (u*) for the (c) particles and (d) BC. Grey points are raw data, and colored markers are mean deposition binned by u* (each one representing 200 measurement points). Slope and intercept for the fit lines are (c) 1 ± 1 and -0.1 ± 0.3 for particles, and (d) 2 ± 7 and 1 ± 2 for BC. Both fits were weighted by the standard deviation of the binned deposition velocities.

The size resolved median dry deposition velocities range from 0.24 – 1.4 cm s^{-1} for aerosols 0.07 – 1 µm and indicate a minimum at approximately 0.13 µm. While these values were lower in October, as we transitioned to full snow cover, a significant difference between periods of no snow cover in September and full snow in October was not observed. Previous measurements, even when combined, have not highlighted a clear minimum to compare this trend against. To investigate the possible source of this increased deposition we therefore used various model parameterizations.

Comparison to current model parameterizations of dry deposition

Dry deposition velocity is frequently predicted using resistance based models that consider the loss from Brownian motion, gravitational settling, interception, and impaction. The Zhang et al. (2001) model is a widely used parameterization that is incorporated into several global models, including GLOMAP and GEOS-Chem, to describe dry deposition[35]. The model considers tundra surfaces and snow/ice covered surfaces similarly, with both modeled as flat surfaces with no contribution from interception. Improvements have been made to this parameterization; however, the focus of these changes has been other land use types[36]. When compared against our measured values, neither the original nor the reparameterization done by Emerson et al. (2020) were able to capture the size-dependent trend observed here (**Figure 3.4**)[36].

Both the Emerson et al. (2020) reparameterization and the more sophisticated model proposed by Petroff and Zhang (2010) have shown that significant improvements can be made to the prediction of size-resolved deposition by modifying the interception term[36,37]. To assess the possible influence of interception, we first incorporated the characteristic radius of collectors used by Petroff and Zhang (2010) for tundra surfaces (5 cm)[37], a variable that was previously undefined in Zhang et al. (2001)[35]. This was done without changing the calculation of collection efficiency from interception in the two models. While this did not improve model and measurement agreement in the Zhang et al. (2001) model, the Emerson et al. (2020) reparameterization did (**Figure 3.4**).

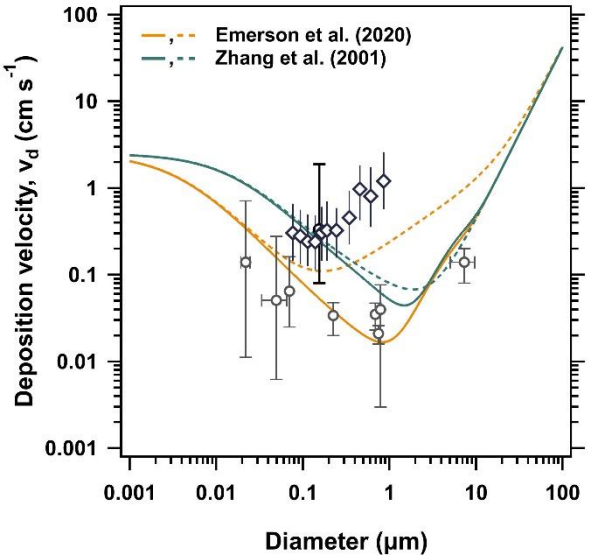

Figure 3.4: Size dependent dry deposition velocities from this study (dark blue diamonds) compared against literature values from Ibrahim et al. (1983), Duan et al. (1988), Nilsson and Rannik (2001), and Contini et al (2010) represented as grey open symbols and the data from Grönlund et al. (2002) being presented as a black open symbol that is thicker than the other literature values[17–21]. Model predictions using average u^*, windspeed, and temperature from the campaign are shown for Zhang et al. (2001) and Emerson et al. (2020). Calculations including interception through the addition of the characteristic radius of collectors variable are shown as dashed lines compared to the original parameterizations in solid lines.

The need for inclusion of interception in the model parameterization indicates that our surface, while covered in snow, cannot be modeled as a flat surface. However, compared to some of the other literature data for dry deposition in the Arctic the Emerson et al. (2021) parameterization agrees well even when interception is excluded. These measurements span from the low to high Arctic, and meteorological and environmental conditions vary widely between them. This stratification of the measurements could be a result of a transition period between rough and smooth snow cover causing changes in deposition trends. Alternatively, this could indicate that there are differences in the deposition trends between the low and high arctic. Further size-resolved measurements of dry deposition in the Arctic over longer time periods are needed to clarify this observed variation.

Conclusions

During the ArcticBCADS campaign in Utqiagvik, dry deposition velocities for total measured particles, 0.13 cm s^{-1}, and BC, 0.85 cm s^{-1}, were higher than previously reported values in Arctic regions. Size-dependent velocities were also elevated, ranging from 0.24 – 1.4 cm s^{-1} (0.07 – 1 µm) and indicated a minimum deposition at ~0.13 µm. While deposition velocities were lower in October, during full snow coverage, than September, which transitioned from no snow to full snow cover, there was not a significant difference between the two periods. Commonly used resistance models, which currently assume a tundra to be a flat surface, were unable to capture the measured trend in dry deposition. However, when interception was incorporated into the Emerson et al. (2020) parameterization, the model was able to better describe the observed trends in size-resolved dry deposition velocities.

While the magnitude of deposition reported here exceeds the majority of other reports in the Arctic, it does not fall outside the scope of other observations. Deposition velocities measured here agree well with those reported by Grönlund et al. (2002) for a snow-covered surface in Dronning Maud Land, Antarctica[21]. Additionally, our measurement period was during months (September and October) that were identified by Macdonald et al. (2017) to have higher deposition velocities compared to other winter months which indicates that our elevated velocities could be the result of the seasonal variation of

deposition in the region[10]. Additional size-resolved measurements of dry deposition in the Arctic over longer time periods are needed to fully characterize and validate this seasonal variation. These results also indicate that the smooth flat surface assumption for a snow-covered tundra is unable to characterize size-resolved deposition over the surface. The need for the inclusion of interception to improve model and measurement agreement indicates that more consideration needs to be given to the topography and microroughness of the snow-covered surfaces.

Larger deposition velocities in this region during snow-cover would cause substantial changes to estimates of aerosol processes and impacts in the low Arctic. Higher loss rates lead to shorter aerosol lifetimes. For example, if we consider dry deposition alone for a 0.1 μm particle from our measurement height of 3.7 m, with the incorporation of interception deposition rate increases by 53% which could lead to a decrease of up to 34% in lifetime. Shorter lifetimes that mean that even short-lived source events that occur regionally would be significant sources of aerosols. This could impact the addition of pollutants and nutrients to the terrestrial surfaces in the Arctic, such as nitrogen, which is often a limiting nutrient[38]. This is especially true as additional sources of aerosols in the Arctic, most notably shipping[39], become more prevalent. Additionally, this could lead to faster changes in surface albedo which would impact the radiative balance in the Arctic. Further work with global models is needed to characterize the full impact of these changes.

CHAPTER 3 – REFERENCES

(1) Serreze, M. C.; Barry, R. G. Processes and Impacts of Arctic Amplification: A Research Synthesis. *Global and Planetary Change* **2011**, *77* (1), 85–96. https://doi.org/10.1016/j.gloplacha.2011.03.004.

(2) Pithan, F.; Mauritsen, T. Arctic Amplification Dominated by Temperature Feedbacks in Contemporary Climate Models. *Nature Geosci* **2014**, *7* (3), 181–184. https://doi.org/10.1038/ngeo2071.

(3) Zelinka, M. D.; Klein, S. A.; Taylor, K. E.; Andrews, T.; Webb, M. J.; Gregory, J. M.; Forster, P. M. Contributions of Different Cloud Types to Feedbacks and Rapid Adjustments in CMIP5. *Journal of Climate* **2013**, *26* (14), 5007–5027. https://doi.org/10.1175/JCLI-D-12-00555.1.

(4) Willis, M. D.; Leaitch, W. R.; Abbatt, J. P. D. Processes Controlling the Composition and Abundance of Arctic Aerosol. *Reviews of Geophysics* **2018**, *56* (4), 621–671. https://doi.org/10.1029/2018RG000602.
(5) Lohmann, U.; Feichter, J. Global Indirect Aerosol Effects: A Review. *Atmospheric Chemistry and Physics* **2005**, *5* (3), 715–737. https://doi.org/10.5194/acp-5-715-2005.
(6) Quinn, P. K.; Bates, T. S.; Baum, E.; Doubleday, N.; Fiore, A. M.; Flanner, M.; Fridlind, A.; Garrett, T. J.; Koch, D.; Menon, S.; Shindell, D.; Stohl, A.; Warren, S. G. Short-Lived Pollutants in the Arctic: Their Climate Impact and Possible Mitigation Strategies. *Atmospheric Chemistry and Physics* **2008**, *8* (6), 1723–1735. https://doi.org/10.5194/acp-8-1723-2008.
(7) Farmer, D. K.; Boedicker, E. K.; DeBolt, H. M. Dry Deposition of Atmospheric Aerosols: Approaches, Observations, and Mechanisms. *Annu. Rev. Phys. Chem.* **2021**. https://doi.org/10.1146/annurev-physchem-090519-034936.
(8) Law, K. S.; Stohl, A. Arctic Air Pollution: Origins and Impacts. **2007**, *315* (5818), 1537–1540. https://doi.org/DOI: 10.1126/science.1137695.
(9) Sharma, S.; Ishizawa, M.; Chan, D.; Lavoué, D.; Andrews, E.; Eleftheriadis, K.; Maksyutov, S. 16-Year Simulation of Arctic Black Carbon: Transport, Source Contribution, and Sensitivity Analysis on Deposition. *Journal of Geophysical Research: Atmospheres* **2013**, *118* (2), 943–964. https://doi.org/10.1029/2012JD017774.
(10) Macdonald, K. M.; Sharma, S.; Toom, D.; Chivulescu, A.; Hanna, S.; Bertram, A. K.; Platt, A.; Elsasser, M.; Huang, L.; Tarasick, D.; Chellman, N.; McConnell, J. R.; Bozem, H.; Kunkel, D.; Lei, Y. D.; Evans, G. J.; Abbatt, J. P. D. Observations of Atmospheric Chemical Deposition to High Arctic Snow. *Atmospheric Chemistry and Physics* **2017**, *17* (9), 5775–5788. https://doi.org/10.5194/acp-17-5775-2017.
(11) Eckhardt, S.; Quennehen, B.; Olivié, D. J. L.; Berntsen, T. K.; Cherian, R.; Christensen, J. H.; Collins, W.; Crepinsek, S.; Daskalakis, N.; Flanner, M.; Herber, A.; Heyes, C.; Hodnebrog, Ø.; Huang, L.; Kanakidou, M.; Klimont, Z.; Langner, J.; Law, K. S.; Lund, M. T.; Mahmood, R.; Massling, A.; Myriokefalitakis, S.; Nielsen, I. E.; Nøjgaard, J. K.; Quaas, J.; Quinn, P. K.; Raut, J.-C.; Rumbold, S. T.; Schulz, M.; Sharma, S.; Skeie, R. B.; Skov, H.; Uttal, T.; von Salzen, K.; Stohl, A. Current Model Capabilities for Simulating Black Carbon and Sulfate Concentrations in the Arctic Atmosphere: A Multi-Model Evaluation Using a Comprehensive Measurement Data Set. *Atmospheric Chemistry and Physics* **2015**, *15* (16), 9413–9433. https://doi.org/10.5194/acp-15-9413-2015.
(12) Arnold, S. R.; Law, K. S.; Brock, C. A.; Thomas, J. L.; Starkweather, S. M.; von Salzen, K.; Stohl, A.; Sharma, S.; Lund, M. T.; Flanner, M. G.; Petäjä, T.; Tanimoto, H.; Gamble, J.; Dibb, J. E.; Melamed, M.; Johnson, N.; Fidel, M.; Tynkkynen, V.-P.; Baklanov, A.; Eckhardt, S.; Monks, S. A.; Browse, J.; Bozem, H. Arctic Air Pollution: Challenges and Opportunities for the next Decade. *Elementa: Science of the Anthropocene* **2016**, *4*, 000104. https://doi.org/10.12952/journal.elementa.000104.
(13) Shindell, D. T.; Chin, M.; Dentener, F.; Doherty, R. M.; Faluvegi, G.; Fiore, A. M.; Hess, P.; Koch, D. M.; MacKenzie, I. A.; Sanderson, M. G.; Schultz, M. G.; Schulz, M.; Stevenson, D. S.; Teich, H.; Textor, C.; Wild, O.; Bergmann, D. J.; Bey, I.; Bian, H.; Cuvelier, C.; Duncan, B. N.; Folberth, G.; Horowitz, L. W.; Jonson, J.; Kaminski, J. W.; Marmer, E.; Park, R.; Pringle, K. J.; Schroeder, S.; Szopa, S.; Takemura, T.; Zeng, G.; Keating, T. J.; Zuber, A. A Multi-Model Assessment of Pollution Transport to the Arctic. *Atmospheric Chemistry and Physics* **2008**, *8* (17), 5353–5372. https://doi.org/10.5194/acp-8-5353-2008.
(14) Lee, L. A.; Pringle, K. J.; Reddington, C. L.; Mann, G. W.; Stier, P.; Spracklen, D. V.; Pierce, J. R.; Carslaw, K. S. The Magnitude and Causes of Uncertainty in Global Model Simulations of Cloud Condensation Nuclei. *Atmospheric Chemistry and Physics* **2013**, *13* (17), 8879–8914. https://doi.org/10.5194/acp-13-8879-2013.
(15) Carslaw, K. S.; Lee, L. A.; Reddington, C. L.; Pringle, K. J.; Rap, A.; Forster, P. M.; Mann, G. W.; Spracklen, D. V.; Woodhouse, M. T.; Regayre, L. A.; Pierce, J. R. Large Contribution of Natural

Aerosols to Uncertainty in Indirect Forcing. *Nature* **2013**, *503* (7474), 67–71. https://doi.org/10.1038/nature12674.
(16) Schmale, J.; Zieger, P.; Ekman, A. M. L. Aerosols in Current and Future Arctic Climate. *Nat. Clim. Chang.* **2021**, *11* (2), 95–105. https://doi.org/10.1038/s41558-020-00969-5.
(17) Ibrahim, M.; Barrie, L. A.; Fanaki, F. An Experimental and Theoretical Investigation of the Dry Deposition of Particles to Snow, Pine Trees and Artificial Collectors. *Atmospheric Environment (1967)* **1983**, *17* (4), 781–788. https://doi.org/10.1016/0004-6981(83)90427-4.
(18) Duan, B.; Fairall, C. W.; Thomson, D. W. Eddy Correlation Measurements of the Dry Deposition of Particles in Wintertime. *J. Appl. Meteor.* **1988**, *27* (5), 642–652. https://doi.org/10.1175/1520-0450(1988)027<0642:ECMOTD>2.0.CO;2.
(19) Nilsson, E. D.; Rannik, Ü. Turbulent Aerosol Fluxes over the Arctic Ocean: 1. Dry Deposition over Sea and Pack Ice. *Journal of Geophysical Research: Atmospheres* **2001**, *106* (D23), 32125–32137. https://doi.org/10.1029/2000JD900605.
(20) Contini, D.; Donateo, A.; Belosi, F.; Grasso, F. M.; Santachiara, G.; Prodi, F. Deposition Velocity of Ultrafine Particles Measured with the Eddy-Correlation Method over the Nansen Ice Sheet (Antarctica). *Journal of Geophysical Research: Atmospheres* **2010**, *115* (D16). https://doi.org/10.1029/2009JD013600.
(21) Grönlund, A.; Nilsson, D.; Koponen, I. K.; Virkkula, A.; Hansson, M. E. Aerosol Dry Deposition Measured with Eddy-Covariance Technique at Wasa and Aboa, DronningMaud Land, Antarctica. *Annals of Glaciology* **2002**, *35*, 355–361. https://doi.org/10.3189/172756402781816519.
(22) Held, A.; Orsini, D. A.; Vaattovaara, P.; Tjernström, M.; Leck, C. Near-Surface Profiles of Aerosol Number Concentration and Temperature over the Arctic Ocean. *Atmospheric Measurement Techniques* **2011**, *4* (8), 1603–1616. https://doi.org/10.5194/amt-4-1603-2011.
(23) von Fischer, J. C.; Rhew, R. C.; Ames, G. M.; Fosdick, B. K.; von Fischer, P. E. Vegetation Height and Other Controls of Spatial Variability in Methane Emissions from the Arctic Coastal Tundra at Barrow, Alaska. *Journal of Geophysical Research: Biogeosciences* **2010**, *115* (G4). https://doi.org/10.1029/2009JG001283.
(24) Villarreal, S.; Hollister, R. D.; Johnson, D. R.; Lara, M. J.; Webber, P. J.; Tweedie, C. E. Tundra Vegetation Change near Barrow, Alaska (1972–2010). *Environ. Res. Lett.* **2012**, *7* (1), 015508. https://doi.org/10.1088/1748-9326/7/1/015508.
(25) Cai, Y.; Montague, D. C.; Mooiweer-Bryan, W.; Deshler, T. Performance Characteristics of the Ultra High Sensitivity Aerosol Spectrometer for Particles between 55 and 800nm: Laboratory and Field Studies. *Journal of Aerosol Science* **2008**, *39* (9), 759–769. https://doi.org/10.1016/j.jaerosci.2008.04.007.
(26) Schwarz, J. P.; Gao, R. S.; Fahey, D. W.; Thomson, D. S.; Watts, L. A.; Wilson, J. C.; Reeves, J. M.; Darbeheshti, M.; Baumgardner, D. G.; Kok, G. L.; Chung, S. H.; Schulz, M.; Hendricks, J.; Lauer, A.; Kärcher, B.; Slowik, J. G.; Rosenlof, K. H.; Thompson, T. L.; Langford, A. O.; Loewenstein, M.; Aikin, K. C. Single-Particle Measurements of Midlatitude Black Carbon and Light-Scattering Aerosols from the Boundary Layer to the Lower Stratosphere. *Journal of Geophysical Research: Atmospheres* **2006**, *111* (D16). https://doi.org/10.1029/2006JD007076.
(27) Stephens, M.; Turner, N.; Sandberg, J. Particle Identification by Laser-Induced Incandescence in a Solid-State Laser Cavity. *Appl. Opt., AO* **2003**, *42* (19), 3726–3736. https://doi.org/10.1364/AO.42.003726.
(28) Papale, D.; Reichstein, M.; Aubinet, M.; Canfora, E.; Bernhofer, C.; Kutsch, W.; Longdoz, B.; Rambal, S.; Valentini, R.; Vesala, T.; Yakir, D. Towards a Standardized Processing of Net Ecosystem Exchange Measured with Eddy Covariance Technique: Algorithms and Uncertainty Estimation. *Biogeosciences* **2006**, *3* (4), 571–583. https://doi.org/10.5194/bg-3-571-2006.
(29) Reichstein, M.; Falge, E.; Baldocchi, D.; Papale, D.; Aubinet, M.; Berbigier, P.; Bernhofer, C.; Buchmann, N.; Gilmanov, T.; Granier, A.; Grünwald, T.; Havránková, K.; Ilvesniemi, H.; Janous, D.; Knohl, A.; Laurila, T.; Lohila, A.; Loustau, D.; Matteucci, G.; Meyers, T.; Miglietta, F.; Ourcival, J.-M.; Pumpanen, J.; Rambal, S.; Rotenberg, E.; Sanz, M.; Tenhunen, J.; Seufert, G.;

Vaccari, F.; Vesala, T.; Yakir, D.; Valentini, R. On the Separation of Net Ecosystem Exchange into Assimilation and Ecosystem Respiration: Review and Improved Algorithm. *Global Change Biology* **2005**, *11* (9), 1424–1439. https://doi.org/10.1111/j.1365-2486.2005.001002.x.

(30) Foken, Th.; Wichura, B. Tools for Quality Assessment of Surface-Based Flux Measurements. *Agricultural and Forest Meteorology* **1996**, *78* (1), 83–105. https://doi.org/10.1016/0168-1923(95)02248-1.

(31) Schaller, C.; Göckede, M.; Foken, T. Flux Calculation of Short Turbulent Events - Comparison of Three Methods. *Atmospheric Measurement Techniques* **2017**, *10* (3), 869–880. https://doi.org/10.5194/amt-10-869-2017.

(32) Held, A. Spectral Analysis of Turbulent Aerosol Fluxes by Fourier Transform, Wavelet Analysis, and Multiresolution Decomposition. *Boundary-Layer Meteorol* **2014**, *151* (1), 79–94. https://doi.org/10.1007/s10546-013-9889-8.

(33) Torrence, C.; Compo, G. P. A Practical Guide to Wavelet Analysis. *Bulletin of the American Meteorological Society* **1998**, *79* (1), 61–78. https://doi.org/10.1175/1520-0477(1998)079<0061:APGTWA>2.0.CO;2.

(34) Conte, M.; Contini, D.; Held, A. Multiresolution Decomposition and Wavelet Analysis of Urban Aerosol Fluxes in Italy and Austria. *Atmospheric Research* **2021**, *248*, 105267. https://doi.org/10.1016/j.atmosres.2020.105267.

(35) Zhang, L.; Gong, S.; Padro, J.; Barrie, L. A Size-Segregated Particle Dry Deposition Scheme for an Atmospheric Aerosol Module. *Atmospheric Environment* **2001**, *35* (3), 549–560. https://doi.org/10.1016/S1352-2310(00)00326-5.

(36) Emerson, E. W.; Hodshire, A. L.; DeBolt, H. M.; Bilsback, K. R.; Pierce, J. R.; McMeeking, G. R.; Farmer, D. K. Revisiting Particle Dry Deposition and Its Role in Radiative Effect Estimates. *PNAS* **2020**. https://doi.org/10.1073/pnas.2014761117.

(37) Petroff, A.; Zhang, L. Development and Validation of a Size-Resolved Particle Dry Deposition Scheme for Application in Aerosol Transport Models. *Geoscientific Model Development* **2010**, *3* (2), 753–769. https://doi.org/10.5194/gmd-3-753-2010.

(38) Fowler, D.; Coyle, M.; Skiba, U.; Sutton, M. A.; Cape, J. N.; Reis, S.; Sheppard, L. J.; Jenkins, A.; Grizzetti, B.; Galloway, J. N.; Vitousek, P.; Leach, A.; Bouwman, A. F.; Butterbach-Bahl, K.; Dentener, F.; Stevenson, D.; Amann, M.; Voss, M. The Global Nitrogen Cycle in the Twenty-First Century. *Philosophical Transactions of the Royal Society B: Biological Sciences* **2013**, *368* (1621), 20130164. https://doi.org/10.1098/rstb.2013.0164.

(39) Aliabadi, A. A.; Thomas, J. L.; Herber, A. B.; Staebler, R. M.; Leaitch, W. R.; Schulz, H.; Law, K. S.; Marelle, L.; Burkart, J.; Willis, M. D.; Bozem, H.; Hoor, P. M.; Köllner, F.; Schneider, J.; Levasseur, M.; Abbatt, J. P. D. Ship Emissions Measurement in the Arctic by Plume Intercepts of the Canadian Coast Guard Icebreaker *Amundsen* from the *Polar 6* Aircraft Platform. *Atmospheric Chemistry and Physics* **2016**, *16* (12), 7899–7916. https://doi.org/10.5194/acp-16-7899-2016.

CONCLUSIONS – SCIENTIFIC IMPLICATIONS AND CONSIDERATIONS FOR FUTURE MEASUREMENTS

This dissertation used size-resolved particle measurements from three distinct environments to understand the role and underlying mechanisms behind particle dry deposition. Aerosols have significant impacts on climate and human health[1,2], and currently represent some of the largest sources of uncertainty in global models[3–5]. Constraining aerosol lifetime through the removal by dry deposition is therefore critical for understanding the potential impacts of these pollutants within an environment.

During the House Observations of Microbial and Environmental Chemistry (HOMEChem) study[6], we observed that significant spatial gradients in aerosol concentration persisted during emission periods in indoor environments. We observed more significant gradients in accumulation mode particles compared to coarse particles which is attributable to loss due to indoor air flow trapping smaller particles as they are transported[7,8]. Overall dilution and deposition are the most important factors controlling particle concentration within a house. Our observations of deposition show that widely used indoor deposition models underestimate particle loss rates for accumulation mode aerosols. Model deposition estimates improve when the mechanisms of Brownian motion, gravitational settling, interception, and impaction are used as opposed to indoor models which consider total available surface area and flow rate through a house[9]. Deposition indoors therefore behaves the same as in outdoor environments, and the fundamental processes governing deposition velocity are uniform throughout different environments.

These observations and findings have implications for indoor surface chemistry, gas uptake onto particles, and exposure assessments. However, they are complicated by the high surface-to-volume ratios of indoor environments. Further measurements of indoor spatial gradients are needed to resolve this, especially those that monitor both aerosol and gas phase species simultaneously. Coupling these measurements is critical for further evaluation of chemistry and human exposure to pollutants in built environments.

To explore how the mechanisms influencing dry deposition of particles changed in in a forested environment we utilized size-resolved particle flux measurements collected as part of the Seasonal Particles in Forests Flux studY (SPiFFY). From this data we observed a substantial increase (130 ± 60%) in the size-dependent deposition during the winter that was not observable in the total particle deposition. The largest differences in dry deposition were observed for particles less than 0.35 µm. Using the Emerson et al. (2020) reparameterization of the Zhang et al. (2001) model[10,11], we explored the possible drivers of this wintertime enhancement; focusing on scalar gradients and surface changes. The mechanism of thermophoresis – caused by gradients in temperature - is too slow to contribute to the observed seasonal differences. Additionally, our analysis shows that the addition of snow to the canopy does not cause significant changes to the deposition. Turbophoresis, caused by gradients in turbulence within the canopy, has an impact on deposition of larger particles but does not explain seasonal variation found in smaller sizes. Increasing the influence of interception explains the enhancement of deposition in the winter, which we hypothesize is a result of changes in the stomatal conditions and needle structure during the winter. Changes in plant physiology and surface microroughness across seasons therefore have significant implications for particle dry deposition in forested environments.

The final portion of this work focuses on black carbon (BC) and particle flux and dry deposition measurements made in 2021 during the Arctic Black Carbon and Aerosol Deposition Study (ArcticBCADS) in Utqiagvik, Alaska, USA. Our measured dry deposition velocities for total measured particles, 0.13 cm s^{-1}, and BC, 0.85 cm s^{-1}, were higher than previously reported values in Arctic regions but still within the scope of available observations. Current resistance models[10,11], which treat a snow-covered tundra as a flat surface, did not accurately capture the observed trends. However, incorporating interception into the prediction improved model and measurement agreement. These results show that the flat surface assumption for all snow-covered surfaces is inaccurate, and the surface topography and microroughness need to be considered even when there is snow-cover. This is in alignment with the findings of Chapter 2, where the addition of snow cover was not enough to drive observed seasonal

changes in deposition. Additionally, the range in deposition values between our observations in this work and others in the literature also indicate that deposition in the low Arctic may differ from the high Arctic, or that the transition from snow to smooth snow-cover may have significant impacts on deposition. Further measurements across latitudes in the Arctic and over longer periods would be needed to validate this.

While this work provides critical observations of dry deposition velocities of particles and BC over snow in the low Arctic, it is still only one of few available size-resolved data sets available[14–18]. In order to fully capture trends in dry deposition in the rapidly changing environment of the Arctic, long term measurements of particle dry deposition are needed across latitudes. Additionally, integrating these results into global models to assess their implications for aerosol impacts is needed to bound the role of aerosols in the Arctic.

Considering this work as a whole, we have demonstrated the importance of considering the contribution of all the mechanisms we discussed in **Figure 0.2**, as well as additional mechanisms, as they relate to different environments. For indoor environments we show that traditional mechanisms with a physical basis are more important than the high surface area indoors in driving deposition. In particular, the consideration of interception was critically important in accurately predicting size-dependent trends indoors. In a Ponderosa pine forest, we demonstrate that additional mechanisms, such as turbophoresis, begin to have a significant role in dry deposition. Additionally, we show that the contribution of previously considered mechanisms changes seasonally in forested environments. Both of these findings support the development of seasonal parameters to bound the contribution of dry deposition mechanisms. Finally, with our low arctic data we demonstrate that even over snow-covered surfaces that are typically considered as flat surfaces these mechanisms play an important role. Consideration of all possible mechanisms even over more uniform surfaces is therefore important in the understanding of dry deposition. The results of this work help bound the changes in dry deposition mechanisms across

environments and expands our understanding of deposition, providing an important step towards better constraining particle lifetime and impacts.

CONCLUSIONS – REFERENCES

(1) Lohmann, U.; Feichter, J. Global Indirect Aerosol Effects: A Review. *Atmospheric Chemistry and Physics* **2005**, *5* (3), 715–737. https://doi.org/10.5194/acp-5-715-2005.

(2) Pope III, C. A.; Dockery, D. W. Health Effects of Fine Particulate Air Pollution: Lines That Connect. *Journal of the Air & Waste Management Association* **2006**, *56* (6), 709–742. https://doi.org/10.1080/10473289.2006.10464485.

(3) Lee, L. A.; Pringle, K. J.; Reddington, C. L.; Mann, G. W.; Stier, P.; Spracklen, D. V.; Pierce, J. R.; Carslaw, K. S. The Magnitude and Causes of Uncertainty in Global Model Simulations of Cloud Condensation Nuclei. *Atmospheric Chemistry and Physics* **2013**, *13* (17), 8879–8914. https://doi.org/10.5194/acp-13-8879-2013.

(4) Carslaw, K. S.; Lee, L. A.; Reddington, C. L.; Pringle, K. J.; Rap, A.; Forster, P. M.; Mann, G. W.; Spracklen, D. V.; Woodhouse, M. T.; Regayre, L. A.; Pierce, J. R. Large Contribution of Natural Aerosols to Uncertainty in Indirect Forcing. *Nature* **2013**, *503* (7474), 67–71. https://doi.org/10.1038/nature12674.

(5) Fowler, D.; Pilegaard, K.; Sutton, M. A.; Ambus, P.; Raivonen, M.; Duyzer, J.; Simpson, D.; Fagerli, H.; Fuzzi, S.; Schjoerring, J. K.; Granier, C.; Neftel, A.; Isaksen, I. S. A.; Laj, P.; Maione, M.; Monks, P. S.; Burkhardt, J.; Daemmgen, U.; Neirynck, J.; Personne, E.; Wichink-Kruit, R.; Butterbach-Bahl, K.; Flechard, C.; Tuovinen, J. P.; Coyle, M.; Gerosa, G.; Loubet, B.; Altimir, N.; Gruenhage, L.; Ammann, C.; Cieslik, S.; Paoletti, E.; Mikkelsen, T. N.; Ro-Poulsen, H.; Cellier, P.; Cape, J. N.; Horváth, L.; Loreto, F.; Niinemets, Ü.; Palmer, P. I.; Rinne, J.; Misztal, P.; Nemitz, E.; Nilsson, D.; Pryor, S.; Gallagher, M. W.; Vesala, T.; Skiba, U.; Brüggemann, N.; Zechmeister-Boltenstern, S.; Williams, J.; O'Dowd, C.; Facchini, M. C.; de Leeuw, G.; Flossman, A.; Chaumerliac, N.; Erisman, J. W. Atmospheric Composition Change: Ecosystems–Atmosphere Interactions. *Atmospheric Environment* **2009**, *43* (33), 5193–5267. https://doi.org/10.1016/j.atmosenv.2009.07.068.

(6) Farmer, D. K.; Vance, M. E.; Abbatt, J. P. D.; Abeleira, A.; Alves, M. R.; Arata, C.; Boedicker, E.; Bourne, S.; Cardoso-Saldaña, F.; Corsi, R.; DeCarlo, P. F.; Goldstein, A. H.; Grassian, V. H.; Ruiz, L. H.; Jimenez, J. L.; Kahan, T. F.; Katz, E. F.; Mattila, J. M.; Nazaroff, W. W.; Novoselac, A.; O'Brien, R. E.; Or, V. W.; Patel, S.; Sankhyan, S.; Stevens, P. S.; Tian, Y.; Wade, M.; Wang, C.; Zhou, S.; Zhou, Y. Overview of HOMEChem: House Observations of Microbial and Environmental Chemistry. *Environ. Sci.: Processes Impacts* **2019**, *21* (8), 1280–1300. https://doi.org/10.1039/C9EM00228F.

(7) Chang, T.-J.; Hu, T.-S. Transport Mechanisms of Airborne Particulate Matters in Partitioned Indoor Environment. *Building and Environment* **2008**, *43* (5), 886–895. https://doi.org/10.1016/j.buildenv.2007.01.030.
(8) Chang, T.-J.; Kao, H.-M.; Hsieh, Y.-F. Numerical Study of the Effect of Ventilation Pattern on Coarse, Fine, and Very Fine Particulate Matter Removal in Partitioned Indoor Environment. *Journal of the Air & Waste Management Association* **2007**, *57* (2), 179–189. https://doi.org/10.1080/10473289.2007.10465311.
(9) Lai, A. C. K.; Nazaroff, W. W. Modeling Indoor Particle Deposition from Turbulent Flow onto Smooth Surfaces. *Journal of Aerosol Science* **2000**, *31* (4), 463–476. https://doi.org/10.1016/S0021-8502(99)00536-4.
(10) Emerson, E. W.; Hodshire, A. L.; DeBolt, H. M.; Bilsback, K. R.; Pierce, J. R.; McMeeking, G. R.; Farmer, D. K. Revisiting Particle Dry Deposition and Its Role in Radiative Effect Estimates. *PNAS* **2020**. https://doi.org/10.1073/pnas.2014761117.
(11) Zhang, L.; Gong, S.; Padro, J.; Barrie, L. A Size-Segregated Particle Dry Deposition Scheme for an Atmospheric Aerosol Module. *Atmospheric Environment* **2001**, *35* (3), 549–560. https://doi.org/10.1016/S1352-2310(00)00326-5.
(12) Altieri, A.; Del Caldo, L.; Manes, F. Morphology of Epicuticular Waxes in Pinus Pinea Needles in Relation to Season and Pollution-Climate. *European Journal of Forest Pathology* **1994**, *24* (2), 79–91. https://doi.org/10.1111/j.1439-0329.1994.tb01061.x.
(13) He, C.; Qiu, K.; Alahmad, A.; Pott, R. Particulate Matter Capturing Capacity of Roadside Evergreen Vegetation during the Winter Season. *Urban Forestry & Urban Greening* **2020**, *48*, 126510. https://doi.org/10.1016/j.ufug.2019.126510.
(14) Ibrahim, M.; Barrie, L. A.; Fanaki, F. An Experimental and Theoretical Investigation of the Dry Deposition of Particles to Snow, Pine Trees and Artificial Collectors. *Atmospheric Environment (1967)* **1983**, *17* (4), 781–788. https://doi.org/10.1016/0004-6981(83)90427-4.
(15) Duan, B.; Fairall, C. W.; Thomson, D. W. Eddy Correlation Measurements of the Dry Deposition of Particles in Wintertime. *J. Appl. Meteor.* **1988**, *27* (5), 642–652. https://doi.org/10.1175/1520-0450(1988)027<0642:ECMOTD>2.0.CO;2.
(16) Nilsson, E. D.; Rannik, Ü. Turbulent Aerosol Fluxes over the Arctic Ocean: 1. Dry Deposition over Sea and Pack Ice. *Journal of Geophysical Research: Atmospheres* **2001**, *106* (D23), 32125–32137. https://doi.org/10.1029/2000JD900605.
(17) Contini, D.; Donateo, A.; Belosi, F.; Grasso, F. M.; Santachiara, G.; Prodi, F. Deposition Velocity of Ultrafine Particles Measured with the Eddy-Correlation Method over the Nansen Ice Sheet (Antarctica). *Journal of Geophysical Research: Atmospheres* **2010**, *115* (D16). https://doi.org/10.1029/2009JD013600.
(18) Grönlund, A.; Nilsson, D.; Koponen, I. K.; Virkkula, A.; Hansson, M. E. Aerosol Dry Deposition Measured with Eddy-Covariance Technique at Wasa and Aboa, DronningMaud Land, Antarctica. *Annals of Glaciology* **2002**, *35*, 355–361. https://doi.org/10.3189/172756402781816519.

APPENDIX 1 - CHAPTER 1 ADDITIONAL INFORMATION

Appendix 1S: Supplemental Information for Chapter 1

Instrument diagnostics and data treatment

Instrument background intercomparisons

We conducted intercomparisons over four days of the HOMEChem campaign, at the beginning from 1 June to 3 June and then in the middle of the campaign on 23 June, during which the four POPS were co-located with each other and the UHSAS. Both of these periods correspond to background when no activities were going on in the house. The POPS were stacked together with approximately 10 to 24 cm between inlets and were placed on a counter space <1m from the UHSAS inlet. No corrections were done in response to these intercomparisons (**Figure 1S.1, 1S.3, 1S.4; Table 1S.2, 1S.4**).

Instrument intercomparisons during cooking

On 23 June, after the second round of background intercomparisons, the fourth POPS was placed bellow the UHSAS inlet in the kitchen and left there for the remainder of the campaign. Data collected from a breakfast, stir-fry, and chili cooking on 25 June was compared for the overlapping size range (0.13 – 1 µm) of the two instruments (**Table 1S.6**, **Figure 1S.7**). The POPS was shown to be responsive to the sharp changes in aerosol concentration, given that there was no delay time between the UHSAS and POPS response to cooking. Although the maximum concentration listed by the manufacturer for the POPS is 1,250 # cm^{-3} the POPS used in the comparison showed good agreement with the UHSAS at higher concentrations. While noise in the POPS measurement increased at these elevated concentrations, averaging the data (1-minute averages in the comparisons) resolved this and resulted in similar results as those obtained from the background intercomparisons.

The two optical instruments were also compared against an SMPS present during the campaign. Using the same data from 23 June data from each cooking type was compared from the overlapping size ranges (0.06 – 0.535 µm for the UHSAS and 0.134 – 0.455 for the µm POPS) (**Table 1S.6**, **Figure 1S.7**).

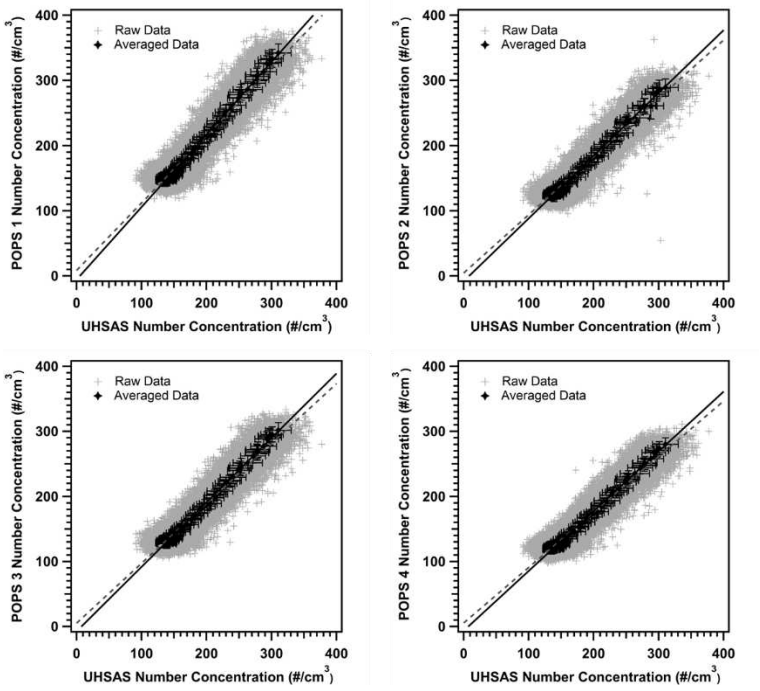

Figure 1S.1: Comparison of number concentration sub-range between the overlapping size regions of the four POPS and the UHSAS showing good correlations between the instruments. The 1-second data is in grey and the 5-minute average of the data is in black in all the plots.

Table 1S.2: Fit equations and R^2/ X^2 values for the POPS to UHSAS intercomparisons. In the table, the fit to the 1-second data is listed first and the fit to the 5-minute average is listed second in bold with a X^2 instead of an R^2 because of the presence of x and y error from the averaging.

Instruments	Slope	Int.	R^2 / $\mathbf{X^2}$
POPS 1 vs UHSAS	1.035 ± 0.002	8.7 ± 0.4	0.901
	1.11 ± 0.04	**-6 ± 8**	**1.54**
POPS 2 vs UHSAS	0.893 ± 0.002	4.5 ± 0.4	0.898
	0.96 ± 0.04	**-8 ± 7**	**1.97**
POPS 3 vs UHSAS	0.920 ± 0.002	5.4 ± 0.4	0.898
	0.99 ± 0.04	**-7 ± 7**	**1.70**
POPS 4 vs UHSAS	0.853 ± 0.002	5.5 ± 0.3	0.902
	0.92 ± 0.04	**-6 ± 6**	**1.72**

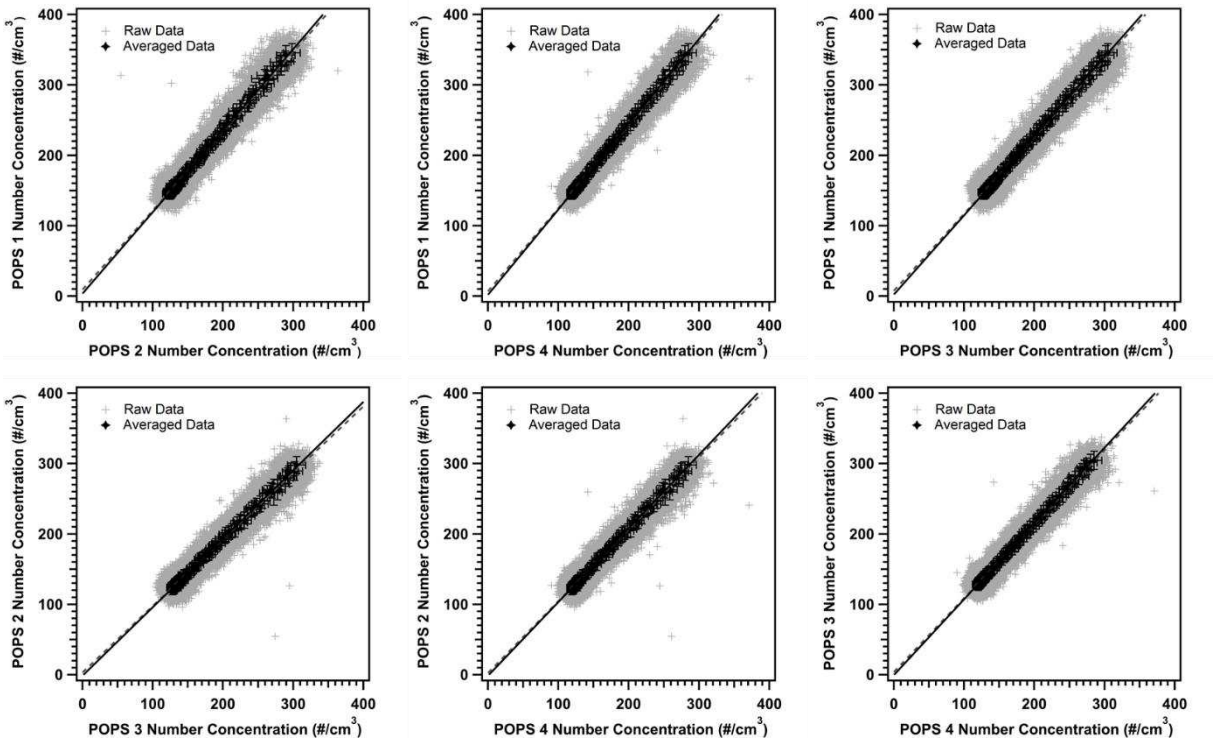

Figure 1S.3: Comparison of number concentration between the four POPS showing good correlations between the instruments during background periods (average comparison slope of 1.0694 ±0.0006).

Table 1S.4: Fit equations and R^2/ X^2 values for the POPS vs POPS intercomparisons. In the table, the fit to the 1-second data is listed first and the fit to the 5-minute average is listed second in bold with a X^2 instead of an R^2 because of the presence of x and y error from the averaging.

Instruments	Slope	Int.	R^2 / X^2
POPS 1 vs POPS 2	1.124 ± 0.001	9.3 ± 0.3	0.947
	1.16 ± 0.03	**4 ± 5**	**2.30**
POPS 1 vs POPS 3	1.095 ± 0.001	7.6 ± 0.3	0.950
	1.13 ± 0.03	**2 ± 5**	**0.568**
POPS 1 vs POPS 4	1.181 ± 0.001	6.9 ± 0.2	0.951
	1.21 ± 0.03	**2 ± 5**	**0.662**
POPS 2 vs POPS 3	0.945 ± 0.001	3.4 ± 0.2	0.945
	0.97 ± 0.03	**-1 ± 4**	**1.65**
POPS 2 vs POPS 4	1.021 ± 0.001	2.7 ± 0.2	0.948
	1.05 ± 0.03	**-1 ± 4**	**1.82**
POPS 3 vs POPS 4	1.051 ± 0.001	3.9 ± 0.2	0.950
	1.08 ± 0.03	**-1 ± 4**	**0.432**

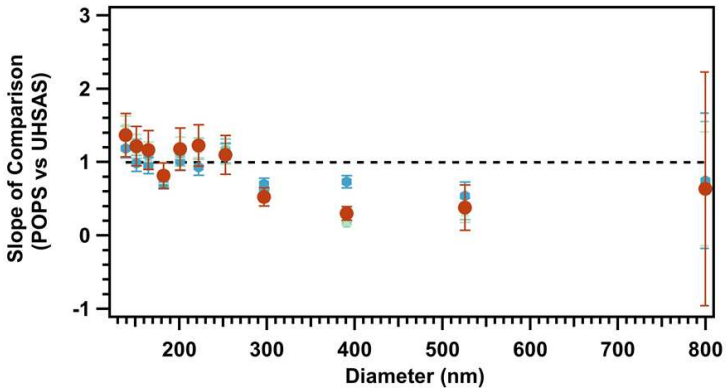

Figure 1S.5: Size-dependent comparison of number concentration between re-binned UHSAS and POPS data which shows that there is an inherent offset between the size ranges on the two instruments. The POPS slightly overestimate particles in their lower range and underestimate particles at the upper end of their range when compared to the UHSAS. Comparisons between each POPS and the UHSAS are represented by the blue points; the orange points are the average slope values from all four POPS.

Table 1S.6: Fit equations and R^2/ X^2 values for the POPS vs UHSAS vs SMPS intercomparisons during cooking. In the table, the fit to the 1-second data is listed first and the fit to the 1-minute average is listed second in bold with a X^2 instead of an R^2 because of the presence of x and y error from the averaging. Background comparison from POPS 4 vs UHSAS is included in the first column for context.

Instruments		Background	Breakfast	Stir-Fry	Chili
POPS vs UHSAS	*Slope*	0.853 ± 0.002	0.766 ± 0.007	0.803 ± 0.009	0.573 ± 0.006
		0.92 ± 0.04	**0.92 ± 0.04**	**0.87 ± 0.02**	**0.83 ± 0.08**
	Int.	5.5 ± 0.3	29 ± 2	-10 ± 20	132 ± 3
		-6 ± 6	**-10 ± 10**	**-2 ± 8**	**20 ± 30**
	R^2 / $\mathbf{X^2}$	0.902	0.928	0.854	0.740
		1.72	**2.65**	**83.8**	**9.58**
POPS vs SMPS	*Slope*		0.55 ± 0.08	0.62 ± 0.01	0.5 ± 0.1
	Int		-140 ± 50	-22 ± 9	20 ± 60
	X^2		**10.9**	**2.07**	**5.23**
UHSAS vs SMPS	*Slope*		0.43 ± 0.04	0.427 ± 0.005	0.51 ± 0.06
	Int.		-10 ± 50	260 ± 40	100 ± 200
	X^2		**1.49**	**34.8**	**22.3**

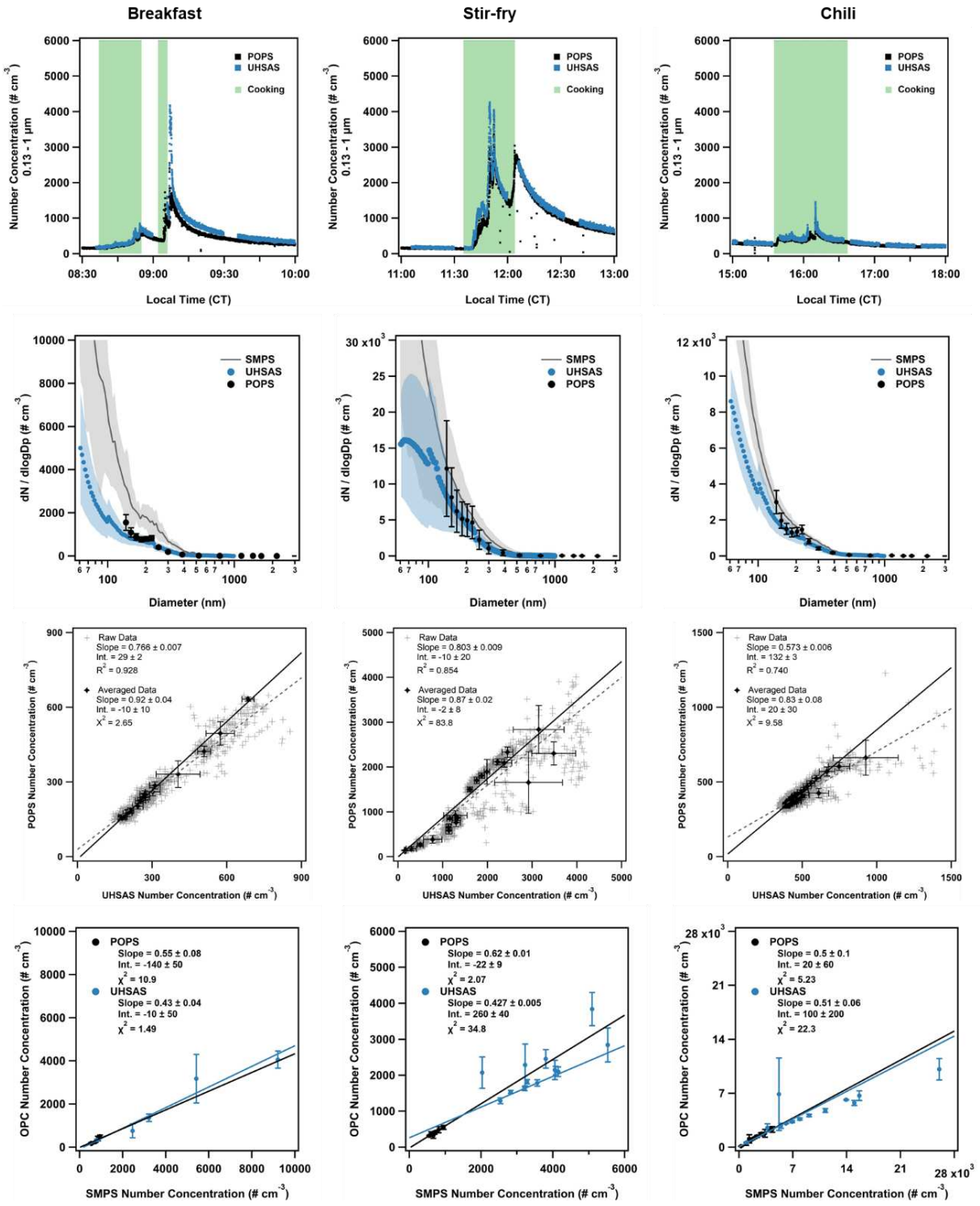
Breakfast
Stir-fry
Chili
POPS
UHSAS
Cooking
Number Concentration (# cm-3) 0.13 - 1 µm
Local Time (CT)
SMPS
dN / dlogDp (# cm-3)
Diameter (nm)
Raw Data
Slope = 0.766 ± 0.007
Int. = 29 ± 2
R2 = 0.928
Averaged Data
Slope = 0.92 ± 0.04
Int. = -10 ± 10
X2 = 2.65
Slope = 0.803 ± 0.009
Int. = -10 ± 20
R2 = 0.854
Slope = 0.87 ± 0.02
Int. = -2 ± 8
X2 = 83.8
Slope = 0.573 ± 0.006
Int. = 132 ± 3
R2 = 0.740
Slope = 0.83 ± 0.08
Int. = 20 ± 30
X2 = 9.58
POPS Number Concentration (# cm-3)
UHSAS Number Concentration (# cm-3)
Slope = 0.55 ± 0.08
Int. = -140 ± 50
X2 = 10.9
Slope = 0.43 ± 0.04
Int. = -10 ± 50
X2 = 1.49
Slope = 0.62 ± 0.01
Int. = -22 ± 9
X2 = 2.07
Slope = 0.427 ± 0.005
Int. = 260 ± 40
X2 = 34.8
Slope = 0.5 ± 0.1
Int. = 20 ± 60
X2 = 5.23
Slope = 0.51 ± 0.06
Int. = 100 ± 200
X2 = 22.3
OPC Number Concentration (# cm-3)
SMPS Number Concentration (# cm-3)

Figure 1S.7: A sub-plot of each cooking event that had enough data to be used for intercomparisons (breakfast, stir-fry, and chili) are presented on the **top row** followed by distribution comparisons in the **second row,** intercomparison plots between the POPS and UHSAS data in the **third row**, and intercomparison plots between the optical particle counters (OPC) and the SMPS in the **fourth row**. The events are in order of the time they were done during the experiment day from left to right in the plots. In the POPS vs UHSAS intercomparison plots raw 1-second data is presented as grey, with the dashed line being the raw intercomparison line, and 1-minute averaged data is presented in black, with the solid line being the intercomparison line. In the OPC vs SMPS the black traces are for the POPS and the blue traces are for the UHSAS.

The comparisons indicate that average number distributions measured by the instruments are comparable, which validates the use of these optical instruments for the size dependent analysis presented. There was disagreement in the smallest sizes of the UHSAS distribution, however, this data was not used in the spatial analysis presented. Additionally, deposition of particles < 100 nm is not presented because of saturation (discussed in the next section) therefore excluding the size region that had the largest difference from the SMPS's number distribution. The comparisons do indicate that the optical instruments underestimate total particle number concentrations during the cooking events. This does not impact this work because the focus here is not on characterizing the total cooking emissions.

Saturation of optical instruments at high concentrations

At high aerosol concentrations, optical instruments will saturate causing the instruments to undercount particles. We present a brief analysis of those saturation levels through comparison of the aerosol number concentration of the two instruments to the SMPS that was present during the HOMEChem study (**Figure 1S.8**). The analysis uses the end of the day decay period from the two Thanksgiving experiments conducted during the campaign (2018/06/18 and 2018/06/27) because it was a period during which the aerosol concentration decayed naturally (no intentional venting) from an extremely elevated level back to background while the house was unoccupied. For the POPS analysis, data from POPS 1 in the kitchen were used. The comparison shows that the POPS consistently overestimates compared to the SMPS and a saturation level for the instrument cannot be identified. The UHSAS agrees well with the SMPS for concentrations below ~3000 particles cm^{-3} and saturation is a significant problem at concentrations above ~10,000 particles cm^{-3}. This saturation is only affecting the second detector of the USHAS, which measures particles < 240 nm in diameter. For this analysis saturation could lead to slight suppression in the number size distribution below 240 nm, however, saturation does not affect the volume estimations since particles from the first detector (> 240 nm) are what dominate this measurement. Additionally, since saturation leads to underestimation of concentration for particles < 240 nm the measured loss rate of

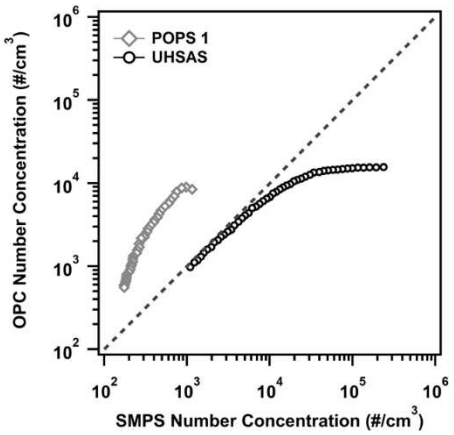

Figure 1S.8: Total concentration from both optical particle counters (OPC) – the UHSAS and POPS – plotted against the total concentration of the SMPS for the size regions that overlapped between the instruments (60 – 530 nm for the UHSAS and SMPS, and 130 – 530 nm for the POPS and SMPS).

these aerosols is also suppressed. Periods where saturation was affecting the data are identified accordingly in this analysis.

Data treatment and density assumption

Both instruments assume spherical particles in all number to area, volume, and mass conversions. All the mass measurements reported in the supplementary text used an assumed density of 1.2 g cm^{-3}, which was selected because of the high organic content of the observed cooking-derived particles.[1] Total mass is not the focus of this work and mass measurement approximations are reported only to provide context. We recognize that for cooking aerosols this density is likely an overestimation and for background periods this density is a slight underestimation. Patel et al. (2020) provides a detailed description of aerosol density during the HOMEChem campaign using Aerosol Mass Spectrometer (AMS) data that was available. Patel et al. (2020) report that aerosol density fluctuated between ~1.0 g cm^{-3} during cooking and ~1.5 g cm^{-3} during non-cooking periods. Given this range, we take 1.2 g cm^{-3} as a density for all the data to provide mass estimations of measured aerosols, unless otherwise stated. Unit density (1.0 g cm^{-3}) is used in the model simulations since it involved only cooking aerosol.

Summary of the Lai and Nazaroff Indoor Deposition Model

Tables 1S.9 – 1S.11 summarize the variables and equations used by the Lai and Nazaroff (2000) to calculate deposition velocity and loss rate of indoor aerosols. The information presented is a recreation of the equation summary tables presented in the original paper.

Summary of the Emerson Outdoor Deposition Model

Tables 1S.12 and 1S.13 summarize the variables and equations used by Emerson et al. (2020) to calculate deposition velocity and loss rate of aerosols, as well as the variables we selected to represent the indoor environment. These calculations are a modification of the Zhang et al. (2001) model.

Experimental days and background conditions during HOMEChem

When no activities are performed indoors and all external doors and windows are closed, penetration of outdoor particles into the building is the most significant source of indoor particles. Out of the three main

Table 1S.9: Variables used in the Lai and Nazaroff (2000) model.

Variable	Definition	Set Value
d_p	Particle diameter	
$\boldsymbol{u^*}$	Friction velocity	1 m/s
$\boldsymbol{\rho_p}$	Particle density	1000 kg m^{-3}
v_s	Gravitational settling velocity	
v	Kinematic viscosity of air	
D	Brownian diffusivity of the particle	
$\mathbf{A_v}$ †	Area of vertical surfaces	250 m^2
$\mathbf{A_u}$ †	Area of upward-facing surfaces	111 m^2
$\mathbf{A_d}$ †	Area of downward-facing surfaces	111 m^2
V †	Volume of the room	250 m^3

† These values are from the house measurements listed in the HOMEChem overview paper [31].

Table 1S.10: Equations used in the Lai and Nazaroff (2000) model.

Parameters	Equation
Integral †	$I = \left[3.64\, Sc^{2/3}\,(a-b) + 39\right]$ $a = \frac{1}{2}\ln\left[\frac{\left(10.92\, Sc^{-1/3} + 4.3\right)^3}{Sc^{-1} + 0.0609}\right] + \sqrt{3}\,\tan^{-1}\left[\frac{8.6 - 10.92\, Sc^{-1/3}}{\sqrt{3}\,10.92\, Sc^{-1/3}}\right]$ $b = \frac{1}{2}\ln\left[\frac{\left(10.92\, Sc^{-1/3} + r^{+}\right)^3}{Sc^{-1} + 7.669\times10^{-4}\,(r^{+})^3}\right] + \sqrt{3}\,\tan^{-1}\left[\frac{2\,r^{+} - 10.92\, Sc^{-1/3}}{\sqrt{3}\,10.92\, Sc^{-1/3}}\right]$
Schmidt number (*Sc*)	$Sc = v\, D^{-1}$
r^{+}(m)	$r^{+} = d_p\, u^{*}(2v)^{-1}$
Deposition velocity, vertical surface (m s^{-1})	$v_{dv} = \frac{u^{*}}{I}$
Deposition velocity, upward horizontal surface (m s^{-1})	$v_{du} = \frac{v_s}{1 - exp\left(-\frac{u_s I}{u^{*}}\right)}$
Deposition velocity, downward horizontal surface (m s^{-1})	$v_{dd} = \frac{v_s}{exp\left(\frac{u_s I}{u^{*}}\right) - 1}$
First-order loss coefficient for deposition, rectangular cavity (s^{-1})	$\beta = \frac{v_{dv}A_v + v_{du}A_u + v_{dd}A_d}{V}$

† Evaluated using the approximation that Brownian diffusivity is negligible compared to the eddy diffusivity. This approximation is valid for diameters larger than 0.01 µm. For smaller particles, a numeric integration is required (see Table S9).

Table 1S.11: Numeric integration of the integral (I), done by Lai and Nazaroff (2000).

Particle Diameter, d_p (μm)	Integral, I (–)
0.001	29.1
0.0015	49.1
0.002	71.0
0.003	120.3
0.004	174.9
0.005	234.2
0.006	297.4
0.007	364.0
0.008	432.7
0.009	504.5
0.01	579.3

Table 1S.12: Variables used by Emerson et al. (2020). The constants in this table are bolded and the value they were set to for the indoor environment are in the last column of the table.

Variable	Definition	Set Value
d_p	Particle diameter	
$\boldsymbol{u^*}$	Friction velocity	0.02 m s^{-1}
ν	Kinematic viscosity of air	
D	Brownian diffusivity of the particle	
C	Cunningham slip correction factor	
$\boldsymbol{u_H}$	Windspeed	0.1 m s^{-1}
$\boldsymbol{\rho_p}$	Particle density	1000 kg m^{-3}
$\boldsymbol{z_r}$	Hight of deposition measurement	2 m
LUC**	Land use category	1
SSC**	Seasonal select category	1
z_0 †	Roughness length	0.8 m
A †	Characteristic radius of collectors	2.0 mm
$\boldsymbol{\varepsilon_0}$	Empirical constant for surface resistance	3
γ †, ‡	Brownian constant	0.56
$\boldsymbol{C_B}$ ‡	Empirical constant for Brownian	0.3
α †	Impaction constant	1.0
$\boldsymbol{\beta}$ ‡	Empirical constant for impaction	0.6
$\boldsymbol{C_{Im}}$ ‡	Empirical constant for impaction	0.1
$\boldsymbol{\upsilon}$ ‡	Empirical constant for interception	1
$\boldsymbol{C_{In}}$	Empirical constant for interception	2.5

**The LUC and SSC follow the numbering system used in Zhang et al. (2001), which parameterized 15 land use categories and 5 seasonal categories.

†These parameters are dependent on the LUC and the SSC. The value tables for these parameters are listed in Zhang et al. (2001), the values listed here are the ones associated with the LUC and SSC that were used in this analysis.

‡ These parameters were altered from the Emerson et al. (2020) model to better represent the indoor data.

Table 1S.13: Summary of main equations used in the Emerson et al. (2020) model.

Parameters	Equation
Deposition velocity (m s^{-1}, V_d)	$V_d = V_g + \frac{1}{(R_a + R_s)}$
Gravitational settling velocity (m s^{-1}, V_g)	$V_g = \frac{\rho_p \, {d_p}^2 \, g \, C}{18 \, \eta}$
Aerodynamic resistance above the canopy (s m^{-1}, R_a)**	$R_a = \frac{\ln\left(\frac{z_r}{z_0}\right) - \psi_H}{\kappa \, u^*}$
Surface resistance (s m^{-1}, R_S)	$R_s = \frac{1}{\varepsilon_0 \, u^* \, (E_b + E_{im} + E_{in}) R_1}$
Collection efficiency from Brownian diffusion (E_b)	$E_b = C_B Sc^{-\gamma}$
Collection efficiency from impaction (E_{im})	$E_{im} = C_{Im} \left(\frac{St}{\alpha + St}\right)^{\beta}$
Collection efficiency from interception (E_{in})	$E_{in} = C_{In} \left(\frac{d_p}{A}\right)^{\upsilon}$
Bounce correction factor (R_1)	$R_1 = exp(-St^{0.5})$
Schmidt number (Sc)	$Sc = \upsilon \, D^{-1}$
Stokes number (St)	$St = \frac{V_g \, u^*}{g \, A}$

**For the indoor environment this term is used to represent the conditions of the air above the sample inlet. The stability function (ψ) was set to zero for the indoor environment.

indoor events simulated during the HOMEChem campaign (i.e. cooking, cleaning, and human occupancy), cooking produced the largest concentration of submicron particles (**Figure 1S.14**).

During background periods, the UHSAS (60 – 1000 nm) measured an indoor concentration of 175.2 ± 0.5 particles cm^{-3} (~1.4 ± 0.3 μg m^{-3}) during the day and 100.2 ± 0.4 particles cm^{-3} (~ 0.8 ± 0.2 μg m^{-3}) at night. Particle concentrations and size distributions were homogeneous (concentration within 18%) throughout the house, and no inherent gradient was observed between rooms (**Figure 1S.15**). Trends in indoor particle concentration mirrored those observed outdoors (**Figure 1S.15**). Both the indoor and outdoor size distributions were bimodal with similar modes but differences in overall magnitude (**Figure 1S.15**). This similarly indicates that the indoor particle concentrations during background periods are dominated by infiltration of outdoor particles, consistent with previous findings.[6–11]

Particle infiltration can be characterized by the ratio between indoor and outdoor (I/O ratio) particle concentrations when the house is closed. This I/O ratio is 0.5 ± 0.1 for number concentration (0.6 ± 0.9 for mass concentration) of submicron particles (**Figure 1S.15**). The I/O ratio varies according to particle size, with ultrafine (< 100 nm) and coarse (> 1 μm) mode particles penetrating least effectively and accumulation mode particles (100 nm – 1 μm) entering most freely with the peak in I/O around 150 nm (**Figure 1S.15**). This trend is the result of diffusion losses due to Brownian motion dominating small particles and gravitational settling forces, impaction, and interception dominating larger particles, causing both modes to deposit in the ventilation system and be removed when moving through the building envelope. For submicron particles, the average I/O ratio is 0.74 ± 0.02. Size-dependent I/O ratios published by Zhao et al. (2019) and Hussein et al. (2005) both showed the same trend with peaks in I/O at 100 – 200 nm. In the context of this work, the I/O ratio represents a general relationship that can be used to investigate the dominating sources of particles indoors.

Aerosol concentrations and distributions during cooking

During all cooking events, particle number concentration indoors increased to at least ten times the indoor background concentration, and at least six times higher than the measured outdoor concentration. Stir-fry

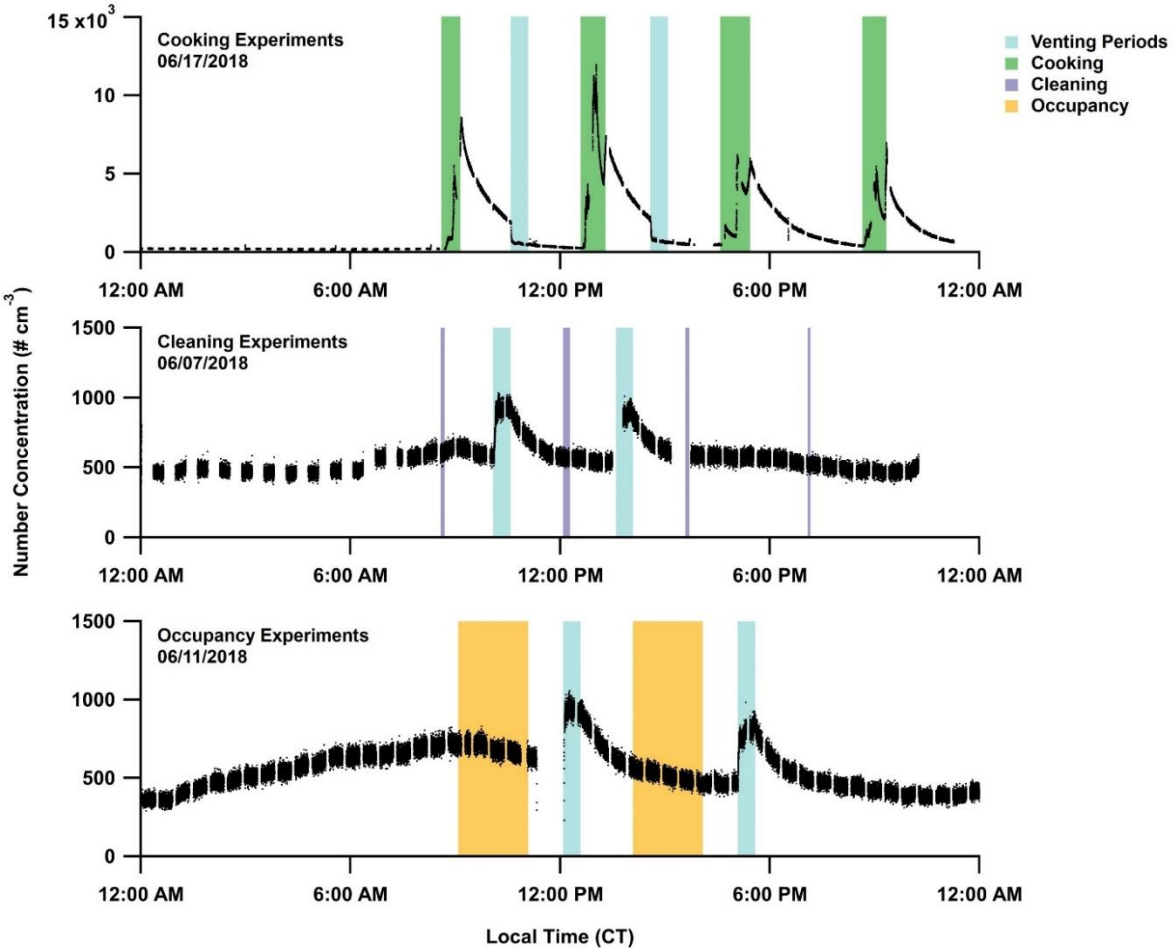

Figure 1S.14: Time-series of three full sequential days when cooking (top), cleaning (middle), and human occupancy (bottom) experiments were done in the house. Cooking had the largest number of particles reported, while cleaning and human occupancy did not show a substantial increase above the background concentration for the particle range sampled (60 – 1000 nm).

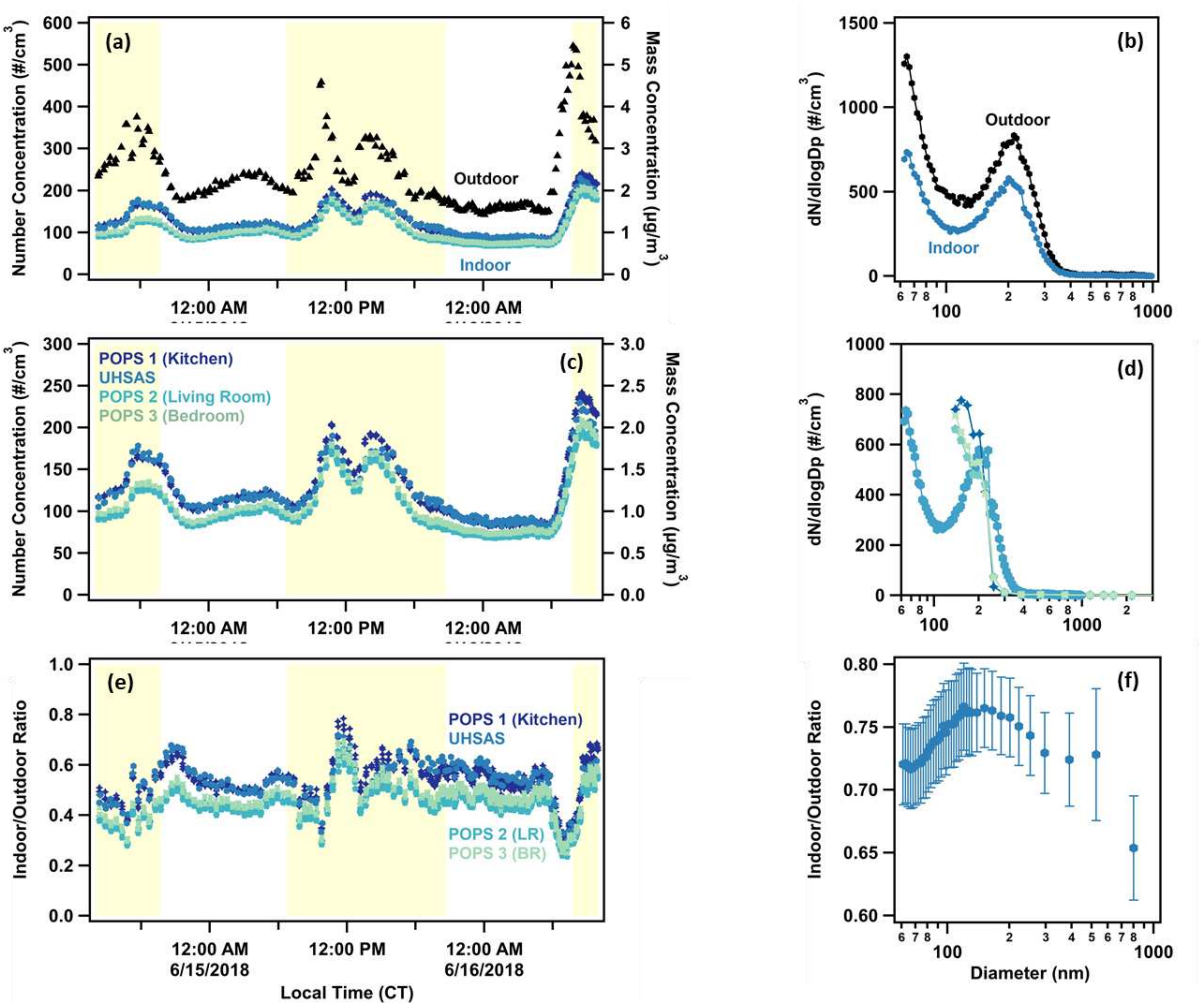

Figure 1S.15: (a) Indoor and outdoor aerosol concentrations during a background period. (b) Size distribution of aerosols indoors and outdoors during background. (c) During background periods there were no significant gradients present throughout the house, even during the daytime periods (highlighted regions) when aerosol concentration spiked. (d) The distribution was also consistent across the house during these periods. (e) Ratio of indoor to outdoor aerosol concentration at all four sampling points. (f) Size-dependent indoor to outdoor aerosol concentration ratio.

events resulted in peak number concentrations, measured by the UHSAS, of approximately 5200 ± 300 particles cm^{-3} (25 ± 2 µg m^{-3}), breakfast events had concentrations of 10800 ± 600 particles cm^{-3} (19.9 ± 0.9 µg m^{-3}), and chili cooking events had an average peak concentration of 5000 ± 300 particles cm^{-3} (14.4 ± 0.6 µg m^{-3}). Toasting bread produced the largest peak number concentration of particles at 12400 ± 500 particles cm^{-3} (16.8 ± 0.8 µg m^{-3}). All the cooking events produced high concentrations of fine and ultra-fine particles, with an average count median diameter of 110 ± 10 nm for all cooking (**Table 1S.16, Figure 1S.17**). Median diameters were relatively consistent through emission periods except for some stir-fry events, which exhibited a change in their distribution during emission periods (**Figure 1S.18, Table 1S.19, Figure 1S.20**).

Loss of cooking aerosol

Measured loss rate for cooking aerosols

Size-dependent loss rate coefficients are shown for different cooking methods and for different cooking events (**Figure 1S.21**). Additionally, loss rate coefficients for each of the instruments and sampling positions is shown in **Figure 1S.22** and average deposition velocity is shown in **Figure 1S.23**.

Deposition velocity model comparisons

Comparison of the Lai and Nazaroff (2000) indoor model and the Emerson et al. (2020) outdoor model to the measured deposition velocities from this study – accumulation mode – and from Tian et al. (2020) - coarse mode – are in **Figure 1S.24**.[3,4,14] We analyzed the sensitivity of the Lai and Nazaroff (2000) model to friction velocity (**Figure 1S.25**) and to changes to surface area caused by the addition of furniture (**Figure 1S.26**).[15] The measurements and model results from Lai and Nazaroff (2000) were also compared against the deposition velocities measured by Thatcher et al. (2002), the results are shown in **Figure 1S.27**.[3,16]

Table 1S.16: Median diameters of aerosol distributions observed by the UHSAS during HOMEChem cooking events

Cooking Event	CMD (nm)	SMD (nm)	VMD (nm)
Breakfast	98 ± 7	126 ± 9	140 ± 10
Toast	99 ± 6	123 ± 8	136 ± 7
Stir-fry**	110 ± 10	180 ± 20	230 ± 20
Chili	101 ± 9	140 ± 10	170 ± 20
Total Cooking	110 ± 10	150 ± 20	180 ± 20

**This represents an overall average distribution during the stir-fry cooking events, however, some of the stir-fry events had a shift in the distribution during the event that resulted in different CMD values.

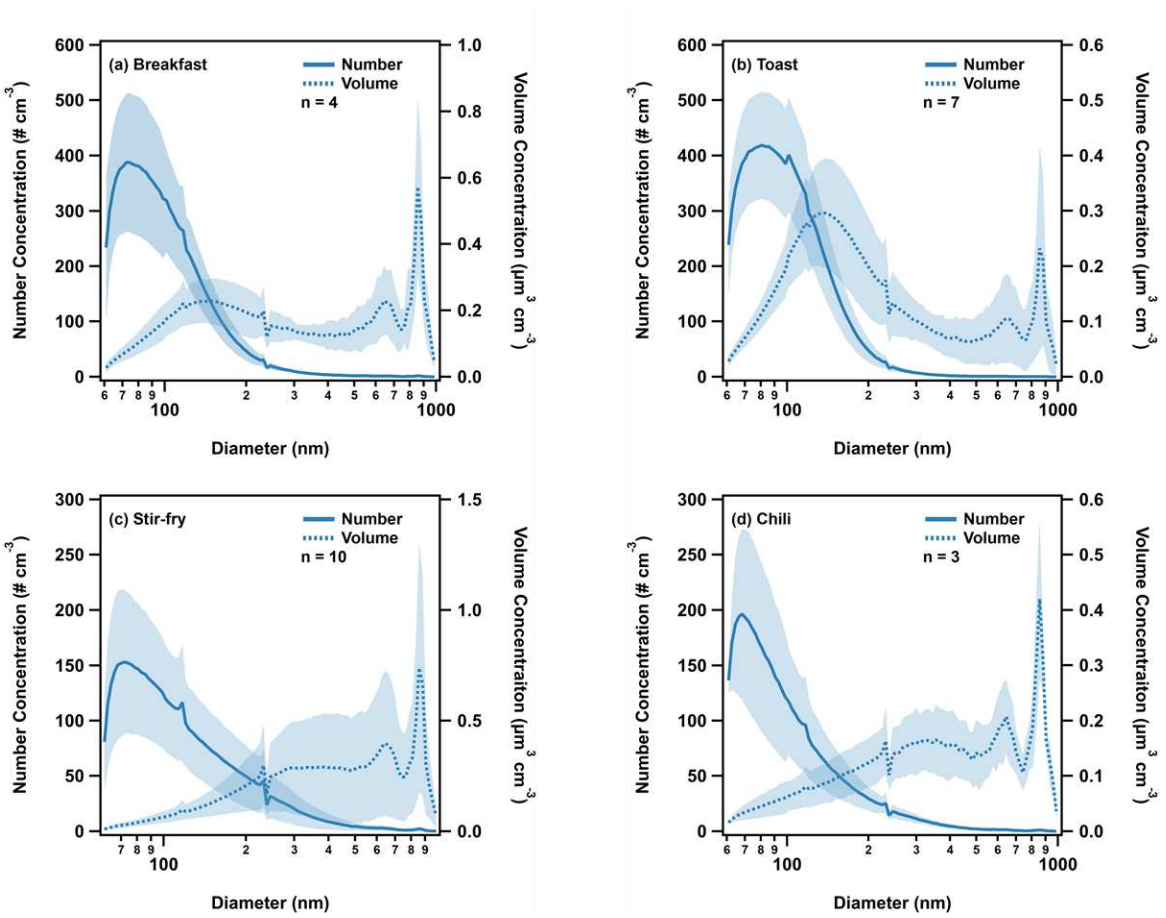

Figure 1S.17: Average distributions for the different cooking events: (a) breakfast, (b) toast, (c) stir-fry, and (d) chili. Each plot has number distribution (dN) on the left, represented by the solid trace, and volume distribution (dV) on the right, represented by the dashed trace. The shaded region on the plots represents the standard deviation of the distributions. The seam at 240 nm is an artifact of the two-detector system on the UHSAS, and this point represents the switching point between the two instruments. In these distributions, both the breakfast and the toast sub 240 nm number concentrations are likely underestimated as a result of saturation.

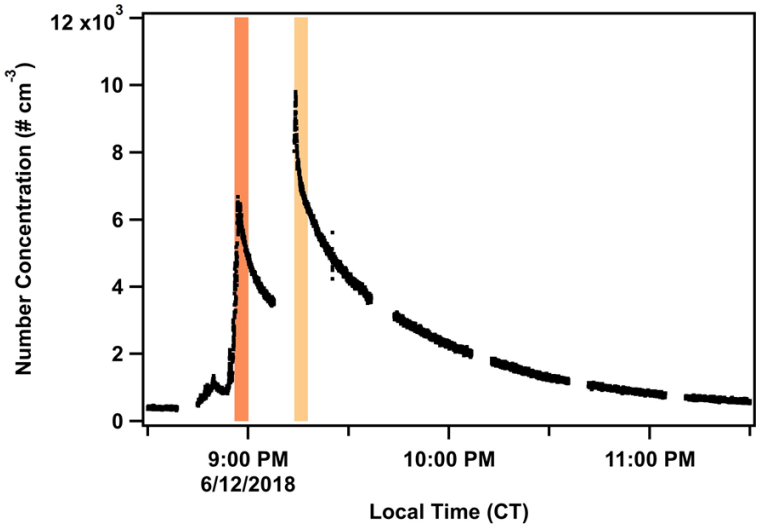

Figure 1S.18: Time series of total number concentration (dN) from the UHSAS showing the typical trend observed during stir-fry events, with each shaded region representing new additions of oil and sauce to the cooking. In six of the observed stir-fry experiments, the aerosol size distributions between these two peaks changed substantially. This stir-fry event from 12th June was one of the stir-fry experiments that exhibited this change in emission.

Table 1S.19: Median diameters of aerosol distributions observed for the different periods during a stir-fry event and the overall median diameter of the event

Stir-fry Period	CMD (nm)	SMD (nm)	VMD (nm)
First Peak	110 ± 10	160 ± 20	200 ± 20
Second Peak	134 ± 6	222 ± 9	290 ± 10
Total Stir-Fry	110 ± 10	180 ± 20	230 ± 20

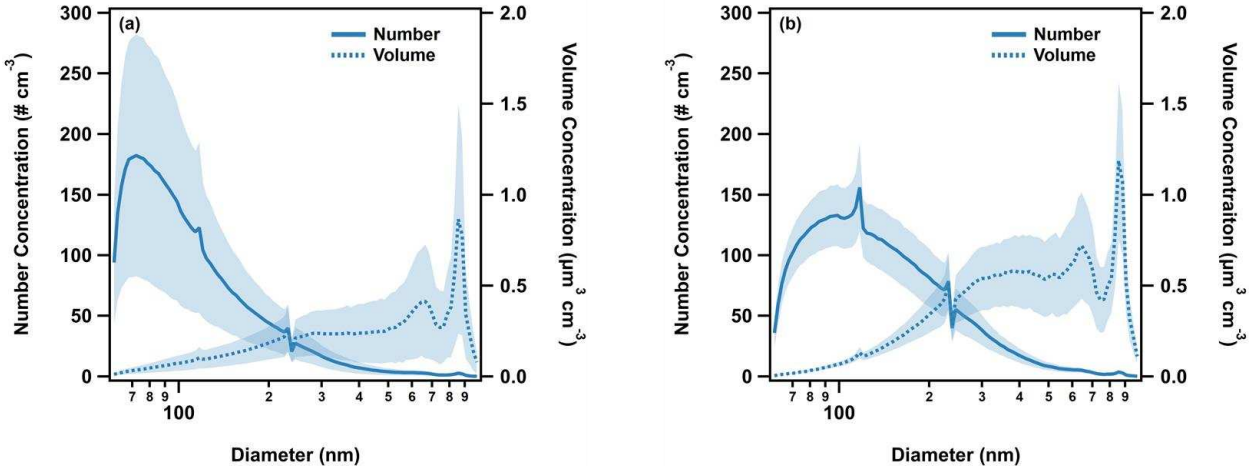

Figure 1S.20: Average distributions for the two peaks during a stir-fry event: (a) first peak and (b) second peak. Both plots have number distribution on the left, the solid trace, and volume distribution on the right, the dashed trace. The shaded region on the plots represents the standard deviation of the distributions. The seam at 240 nm is an artifact of the two-detector system on the UHSAS, and this point represents the switching point between the two instruments.

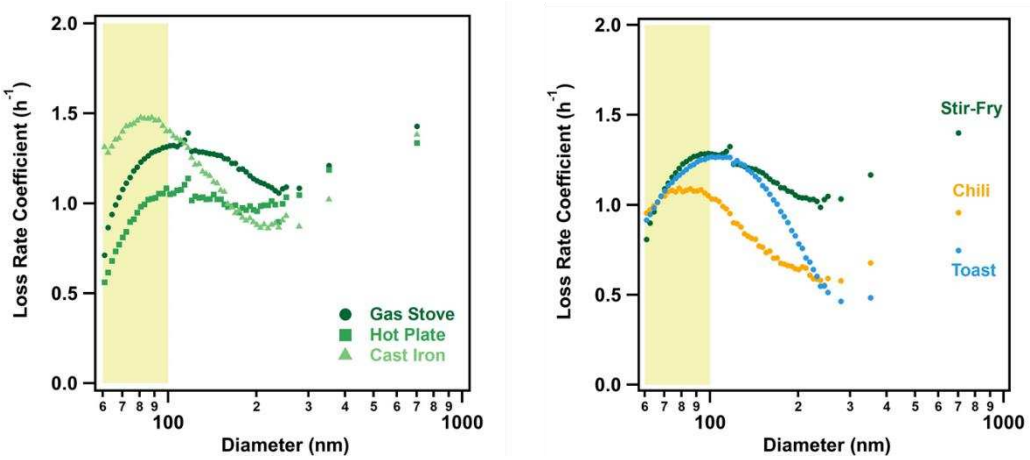

Figure 1S.21: Measured loss rates for the different stir-fry types (left) and the different types of cooking events (right). The size-dependent loss rates for the three types of stir-fries and the different cooking events were not substantially different from each other. The highlighted region of both plots represents the data below 100 nm that was heavily affected by saturation of one of the UHSAS detectors, leading to suppressed concentration peaks and loss rates.

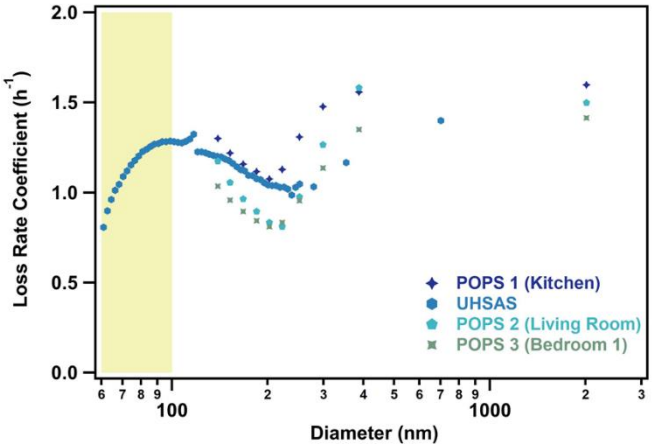

Figure 1S.22: Measured loss rates at the four measurement points throughout the house. The highlighted region in the figure represents data that was heavily affected by UHSAS saturation, leading to suppressed concentration peaks and loss rates. No significant variation was observed between rooms for the aerosol loss rate.

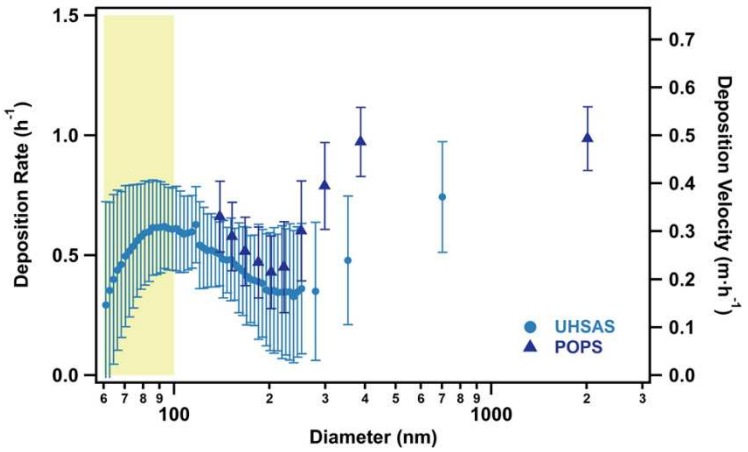

Figure 1S.23: Total average deposition rate and deposition velocity for all HOMEChem cooking events from the UHSAS and the POPS. Error bars represent the standard deviation of the measured deposition across the different experiments. The highlighted region in the figure represents data that was heavily affected by UHSAS saturation, leading to suppressed deposition rates. Data in this region is omitted from the modeled deposition analysis.

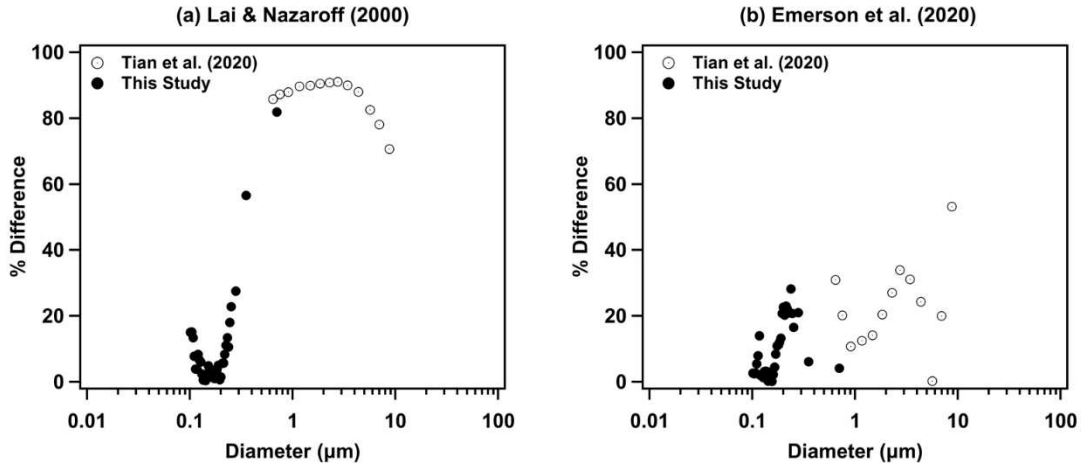

Figure 1S.24: Percent difference between the modeled and measured deposition velocities and rates for the **(a)** Lai and Nazaroff (2000) indoor model and **(b)** Emerson et al. (2020) outdoor model.[3,4] These residuals were calculated for the UHSAS data and the deposition rate values from Tian et al. (2020).[14]

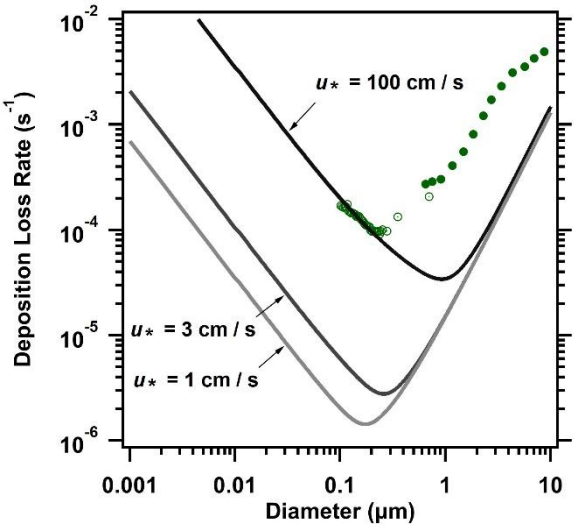

Figure 1S.25: Deposition loss rates produced by different friction velocities in the Lai and Nazaroff (2000) model.[3] Green points represent the UHSAS data (open circles) and the deposition rate data presented in Tian et al. (2020) (closed circles) from the HOMEChem study.[14]

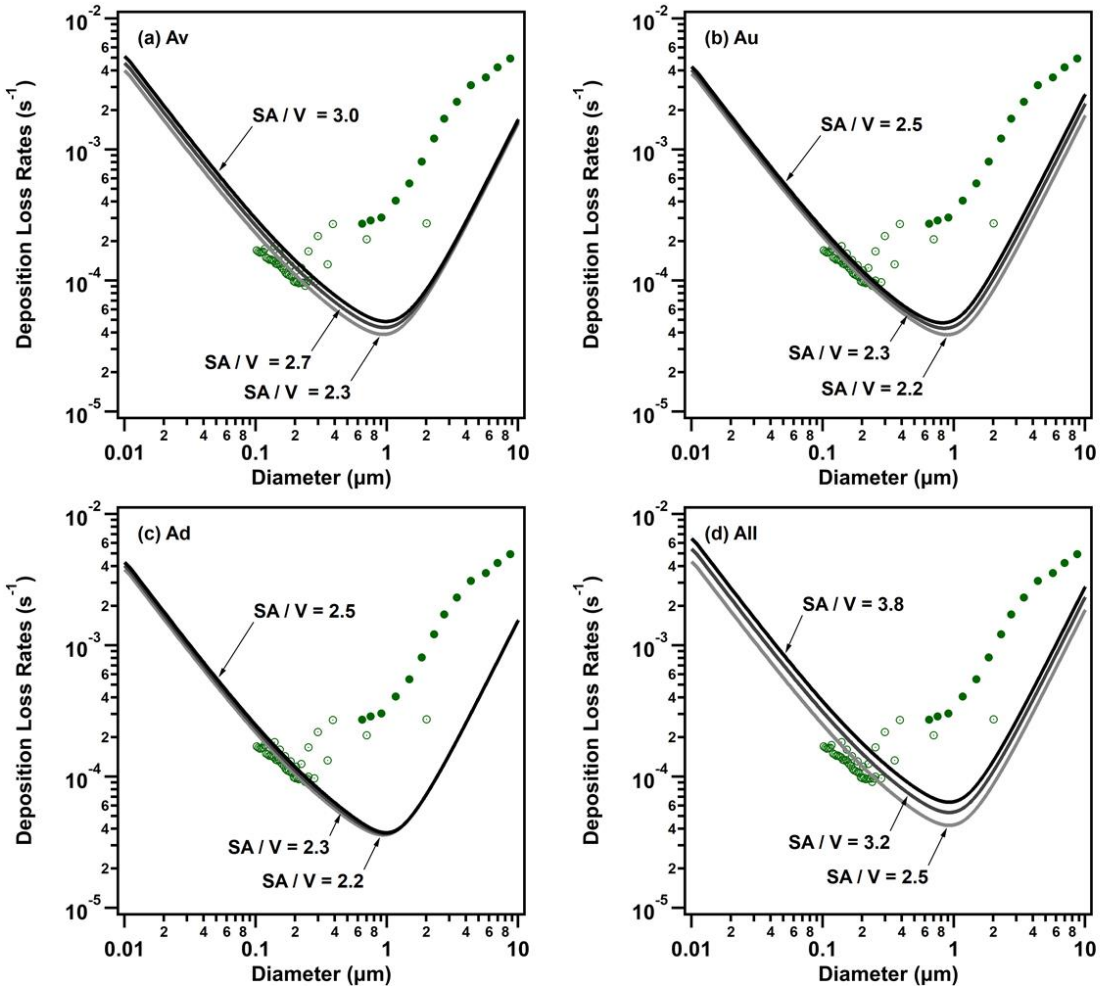

Figure 1S.26: Constraint of the surface-area-to-volume ratio (SA/V) in the Lai and Nazaroff (2000) model.[3] Surface area was increased by 20% (light grey line), 50% (grey line), and 80% (black line) for the **(a)** vertical surfaces, **(b)** upward-facing surfaces, **(c)** downward-facing surfaces, and **(d)** all surfaces. In all cases volume was decreased by 10% from the reported volume for the test house. This manipulation was based on the work of Manuja et al. (2019), where it was reported that on average the contents of a room result in a 50% increase in the total surface area and a 10% decrease in the total volume.[15] None of these variations in the surface-area-to-volume ratio had a significant impact on the agreement between the observed deposition rates and those produced by the model. Green points represent the UHSAS data (open circles) and the deposition rate data presented in Tian et al. (2020) (closed circles) from the HOMEChem study.[14]

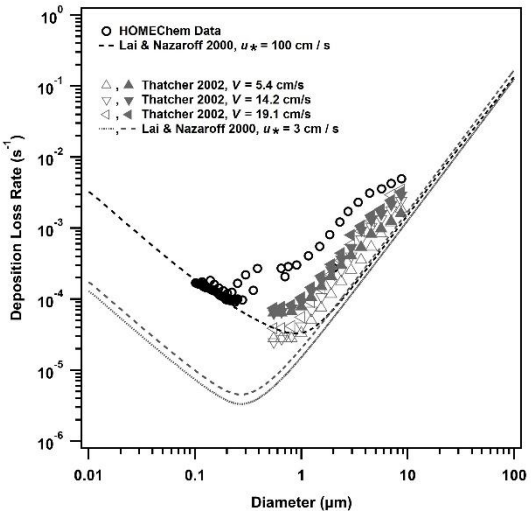

Figure 1S.27: Comparison between the values and model parameters found in Thatcher et al. (2002) (open markers are bare room and closed markers are for a furnished room)and the values obtained during HOEMChem. The HOMEChem deposition measurements lie within the range of variability for indoor measurements that Thatcher et al. (2002) explored and found similar underestimation of deposition from the Lai and Nazaroff (2000) model[3,16]. All model runs assume unit density (1.0 g cm^{-3}) in this figure.

Coagulation during cooking

Concentration maps used to show possible coagulation events are presented in **Figure 1S.28**.

The equations used to model possible coagulation, and the results of these calculations are shown in **Table 1S.29** and **Figure 1S.30**.

Observed gradients in aerosol concentration during cooking

Data used to construct **Figure 1.4** are shown here in **Table 1S.31** and **Table 1S.32**.

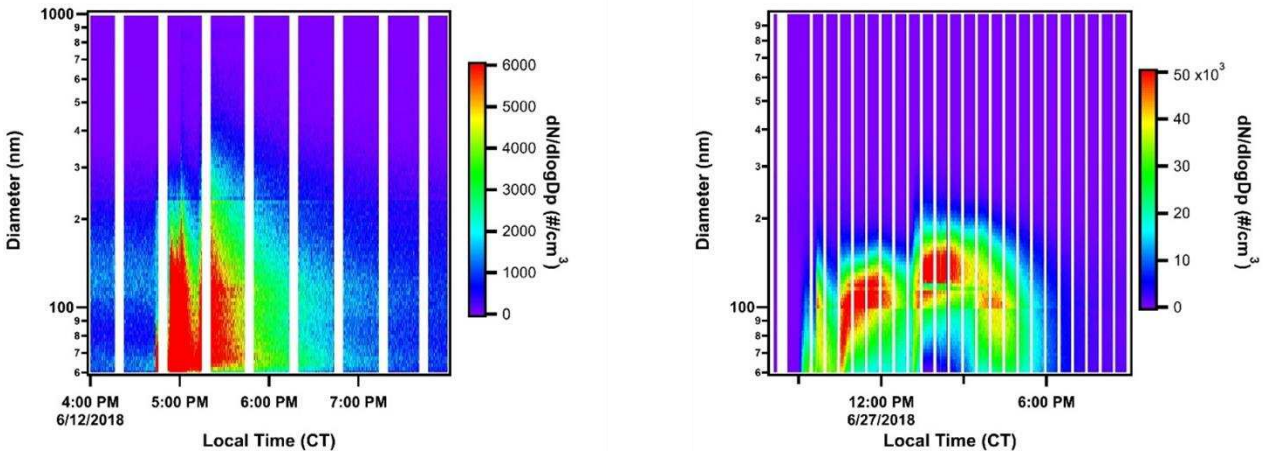

Figure 1S.28: Concentration map for a typical stir-fry event (left) and one of the Thanksgiving Day experiments (right). Coagulation was not a major loss mechanism for particles produced during pulsed events, however, when concentration was high for an extended period, like it was during Thanksgiving, coagulation was observed.

Table 1S.29: Major equations used in coagulation calculations, following Fuchs form of the Brownian coagulation coefficient.[17]

Parameters	Equation
Diffusivity (m^2 s^{-1}, D_i)*	$D = \frac{k_B T\, C_C}{3\,\pi\,\mu\, d_{p,i}}$
Mean thermal speed of the particle (m s^{-1}, $\bar{c}_i$)**	$\bar{c}_\mathrm{i} = \left(\frac{8\, k_B\, T}{\pi\, m_i}\right)^{1/2}$
Mean free path (m, l_i)	$l_i = \frac{8\, D_i}{\pi\, \bar{c}_\mathrm{i}}$
Gravitational constant (m, g_i)	$g_i = \frac{1}{3\, d_{p,i}\, l_i}\left[\left(d_{p,i} + l_i\right)^3 - \left({d_{p,i}}^2 + {l_i}^2\right)^{3/2}\right] - d_{p,i}$
Coagulation coefficient (m^3 s^{-1}, $K_{i,j}$)	$K_{1,2} = 2\pi(D_1 + D_2)\left(d_{p,1} + d_{p,2}\right)\left(\frac{d_{p,1} + d_{p,2}}{d_{p,1} + d_{p,2} + 2(g_1^2 + g_2^2)^{1/2}} + \frac{8\,(D_1 + D_2)}{(\bar{c}_1^2 + \bar{c}_2^2)^{1/2}\left(d_{p,1} + d_{p,2}\right)}\right)^{-1}$

* The variable C_c is the Cunningham slip correction factor and μ is the viscosity of air.
** The variable m_i is the mass of particle i.

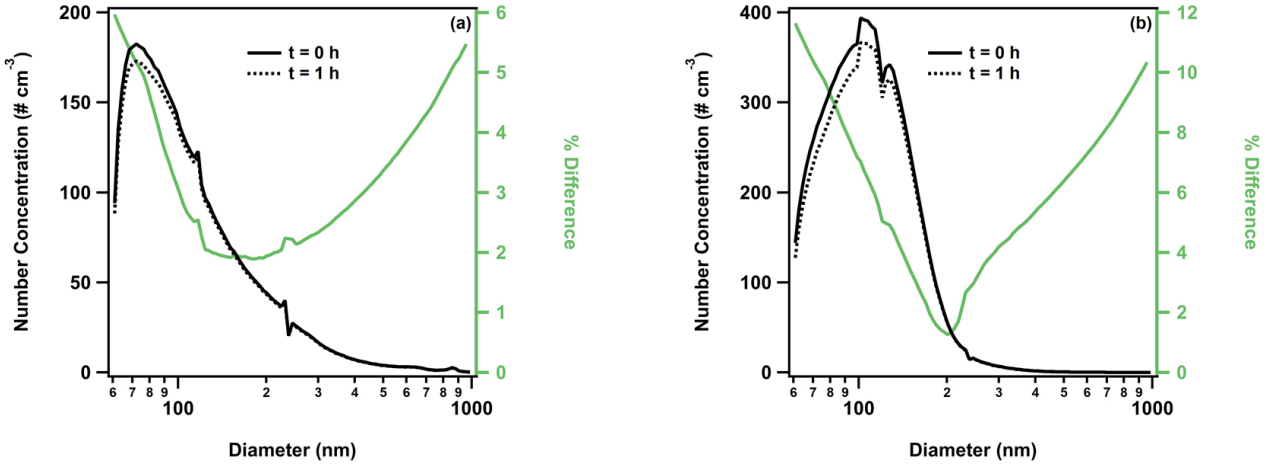

Figure 1S.30: Results of theoretical calculations for the impact of coagulation on **(a)** stir-fry (total starting concentration of 5197 # cm^{-3}) and **(b)** Thanksgiving Day experiments (total starting concentration of 11813 # cm^{-3}). In both panels, the average distribution for the experiments is represented as the solid black line (t = 0), and the predicted distribution after having coagulation as the only loss process for 1 hour is the dashed black line. Percent difference between the two distributions, on the right axis, is displayed in green.

Table 1S.31: Statistical data (maximum, 75th percentile, median, 25th percentile, and minimum) for the percent differences between the kitchen and the living room during cooking. Absent numbers in the larger bins are a result of excluding data where concentration was less than 1 # cm^{-3}.

Mean Diameter (µm)	Maximum	75th	Median	25th	Minimum
139.32	89.25	65.78	44.16	31.16	16.64
152.41	88.29	68.49	54.92	38.98	33.61
167.49	84.87	75.10	52.01	42.40	36.79
184.50	84.29	73.85	46.59	39.65	32.05
202.54	83.38	66.15	48.23	39.21	34.83
222.08	80.54	44.90	37.50	27.54	18.27
251.77	72.47	30.31	18.35	12.43	3.92
298.54	109.89	73.37	59.06	22.75	8.29
387.26	74.71	35.42	27.70	6.32	1.08
522.99	47.29	38.59	26.91	8.45	0.38
764.72	70.03	44.90	24.21	21.05	1.19
1132.40	121.47	75.811	42.03	17.33	5.41
1399.59	77.92	58.14	30.75	20.52	17.91
1627.42	81.90	81.90	43.70	5.50	5.50
2157.74	-	-	-	-	-
3002.62	-	-	-	-	-

Table 1S.32: Statistical data (maximum, 75th percentile, median, 25th percentile, and minimum) for the percent differences between the kitchen and the bedroom during cooking. Absent numbers in the larger bins are a result of excluding data where concentration was less than 1 # cm^{-3}.

Mean Diameter (µm)	Maximum	75th	Median	25th	Minimum
139.32	93.56	82.43	71.16	56.83	39.92
152.41	96.46	86.45	70.95	62.87	43.45
167.49	97.61	82.03	72.49	63.75	42.02
184.50	97.34	74.38	69.03	61.17	34.42
202.54	96.43	72.59	63.72	57.26	31.12
222.08	95.42	72.25	59.95	53.28	32.10
251.77	91.87	60.92	36.41	20.66	4.50
298.54	86.64	54.14	39.32	22.94	1.29
387.26	90.26	66.60	56.00	35.06	7.01
522.99	85.65	67.93	60.28	47.95	1.29
764.72	72.58	60.73	49.74	34.01	10.99
1132.40	76.85	58.64	50.77	34.36	8.66
1399.59	77.19	56.53	29.61	14.55	5.74
1627.42	74.08	74.08	38.84	3.61	3.61
2157.74	-	-	-	-	-
3002.62	-	-	-	-	-

Appendix 1S: References

(1) Turpin, B. J.; Lim, H.-J. Species Contributions to PM2.5 Mass Concentrations: Revisiting Common Assumptions for Estimating Organic Mass. *Aerosol Science and Technology* **2001**, *35* (1), 602–610. https://doi.org/10.1080/02786820119445.

(2) Patel, S.; Sankhyan, S.; Boedicker, E. K.; DeCarlo, P. F.; Farmer, D. K.; Goldstein, A. H.; Katz, E. F.; Nazaroff, W. W.; Tian, Y.; Vanhanen, J.; Vance, M. E. Indoor Particulate Matter during HOMEChem: Concentrations, Size Distributions, and Exposures. *Environ. Sci. Technol.* **2020**, *54* (12), 7107–7116. https://doi.org/10.1021/acs.est.0c00740.

(3) Lai, A. C. K.; Nazaroff, W. W. Modeling Indoor Particle Deposition from Turbulent Flow onto Smooth Surfaces. *Journal of Aerosol Science* **2000**, *31* (4), 463–476. https://doi.org/10.1016/S0021-8502(99)00536-4.

(4) Emerson, E. W.; Hodshire, A. L.; DeBolt, H. M.; Bilsback, K. R.; Pierce, J. R.; McMeeking, G. R.; Farmer, D. K. Revisiting Particle Dry Deposition and Its Role in Radiative Effect Estimates. *PNAS* **2020**. https://doi.org/10.1073/pnas.2014761117.

(5) Zhang, L.; Gong, S.; Padro, J.; Barrie, L. A Size-Segregated Particle Dry Deposition Scheme for an Atmospheric Aerosol Module. *Atmospheric Environment* **2001**, *35* (3), 549–560. https://doi.org/10.1016/S1352-2310(00)00326-5.

(6) Meng, Q. Y.; Spector, D.; Colome, S.; Turpin, B. Determinants of Indoor and Personal Exposure to PM2.5 of Indoor and Outdoor Origin during the RIOPA Study. *Atmospheric Environment* **2009**, *43* (36), 5750–5758. https://doi.org/10.1016/j.atmosenv.2009.07.066.

(7) Abt, E.; Suh, H. H.; Allen, G.; Koutrakis, P. Characterization of Indoor Particle Sources: A Study Conducted in the Metropolitan Boston Area. *Environmental Health Perspectives* **2000**, *108* (1), 35–44. https://doi.org/10.2307/3454293.

(8) Kearney, J.; Wallace, L.; MacNeill, M.; Xu, X.; VanRyswyk, K.; You, H.; Kulka, R.; Wheeler, A. J. Residential Indoor and Outdoor Ultrafine Particles in Windsor, Ontario. *Atmospheric Environment* **2011**, *45* (40), 7583–7593. https://doi.org/10.1016/j.atmosenv.2010.11.002.

(9) Kearney, J.; Wallace, L.; MacNeill, M.; Héroux, M.-E.; Kindzierski, W.; Wheeler, A. Residential Infiltration of Fine and Ultrafine Particles in Edmonton. *Atmospheric Environment* **2014**, *94*, 793–805. https://doi.org/10.1016/j.atmosenv.2014.05.020.

(10) Long, C. M.; Suh, H. H.; Catalano, P. J.; Koutrakis, P. Using Time- and Size-Resolved Particulate Data To Quantify Indoor Penetration and Deposition Behavior. *Environ. Sci. Technol.* **2001**, *35* (10), 2089–2099. https://doi.org/10.1021/es001477d.

(11) Allen, R.; Larson, T.; Sheppard, L.; Wallace, L.; Liu, L.-J. S. Use of Real-Time Light Scattering Data To Estimate the Contribution of Infiltrated and Indoor-Generated Particles to Indoor Air. *Environ. Sci. Technol.* **2003**, *37* (16), 3484–3492. https://doi.org/10.1021/es021007e.

(12) Zhao, J.; Birmili, W.; Wehner, B.; Daniels, A.; Weinhold, K.; Wang, L.; Merkel, M.; Kecorius, S.; Tuch, T.; Franck, U.; Hussein, T.; Wiedensohler, A. Particle Mass Concentrations and Number Size Distributions in 40 Homes in Germany: Indoor-to-Outdoor Relationships, Diurnal and Seasonal Variation. *Aerosol Air Qual. Res.* **2019**, *20* (3), 576–589. https://doi.org/10.4209/aaqr.2019.09.0444.

(13) Hussein, T.; Hämeri, K.; Heikkinen, M. S. A.; Kulmala, M. Indoor and Outdoor Particle Size Characterization at a Family House in Espoo–Finland. *Atmospheric Environment* **2005**, *39* (20), 3697–3709. https://doi.org/10.1016/j.atmosenv.2005.03.011.

(14) Tian, Y.; Arata, C.; Boedicker, E.; Lunderberg, D. M.; Patel, S.; Sankhyan, S.; Kristensen, K.; Misztal, P. K.; Farmer, D. K.; Vance, M.; Novoselac, A.; Nazaroff, W. W.; Goldstein, A. H. Indoor Emissions of Total and Fluorescent Supermicron Particles during HOMEChem. *Indoor Air* **2020**. https://doi-org.ezproxy2.library.colostate.edu/10.1111/ina.12731.

(15) Manuja, A.; Ritchie, J.; Buch, K.; Wu, Y.; Eichler, C. M. A.; Little, J. C.; Marr, L. C. Total Surface Area in Indoor Environments. *Environ. Sci.: Processes Impacts* **2019**, *21* (8), 1384–1392. https://doi.org/10.1039/C9EM00157C.

(16) Thatcher, T. L.; Lai, A. C. K.; Moreno-Jackson, R.; Sextro, R. G.; Nazaroff, W. W. Effects of Room Furnishings and Air Speed on Particle Deposition Rates Indoors. *Atmospheric Environment* **2002**, *36* (11), 1811–1819. https://doi.org/10.1016/S1352-2310(02)00157-7.
(17) Seinfeld, J. H.; Pandis, S. N. *Atmospheric Chemistry and Physics: From Air Pollution to Climate Change*, 3rd ed.; John Wiley & Sons, Inc.: New York, NY, 1998.

APPENDIX 2 – CHAPTER 2 ADDITIONAL INFORMATION

Appendix 2A: Outline of Deposition Model Frameworks and Parameterizations

We used two main models to explore the roles and possible seasonal changes of deposition mechanisms. The first was a resistance model developed by Emerson et al. (2020), which is based on the models presented by Zhang et al. (2001) and Slinn (1982).[1–3] This model considered four main deposition mechanisms: Brownian motion, gravitational settling, interception, and impaction. Deposition velocity in the Emerson et al. (2020) model is defined using the gravitational settling velocity (V_g), the aerodynamic resistance (R_a), and the surface resistance (R_s).[1]

$$V_d(d_p) = V_g(d_p) + \frac{1}{R_a + R_s} \tag{2A.1}$$

$$V_g(d_p) = \frac{d_p^2 \, \rho_p \, g \, C_c}{18 \, \eta} \tag{2A.2}$$

$$R_a = \frac{\ln\left(\frac{z_r}{z_0}\right) - \psi_H}{\kappa \, u^*} \tag{A3}$$

$$R_s = \frac{1}{\varepsilon_0 \, u^* \, (E_b + E_{im} + E_{in}) \, R_1} \tag{A4}$$

$$R_1 = e^{-St^{1/2}} \tag{2A.5}$$

$$E_b = C_b Sc^{-2/3} \tag{2A.6}$$

$$E_{im} = C_{im} \left(\frac{St}{\alpha + St}\right)^{\beta} \tag{2A.7}$$

$$E_{in} = C_{in} \left(\frac{d_p}{A}\right)^{\upsilon} \tag{A8}$$

In these equations d_p is the particle diameter, ρ_p is the density of the particle, g is the gravitational acceleration, C_c is the Cunningham slip correction factor, η is the kinematic viscosity of air, z_r is measurement height, z_0 is the roughness length, ψ_H is the stability function, St is the stokes number, and Sc is the Schmidt number. The set variables are C_b = 0.2, C_{im} = 0.4, β = 1.7, C_{in} = 2.5, and υ = 0.8 while the variables α and A are land use dependent and can be found in the original Zhang et al. (2001) publication.

The second model that we explored was from Katul et al. (2010), who presented a multi-layer model that considered the mechanisms of Brownian motion, gravitational settling, impaction, and turbophoresis.[4] This model defined the quasi-laminar boundary layer resistance, or surface resistance, according to the equations outlined by Seinfeld and Pandis (1998) and added an additional term describing turbophoresis.[5]

$$R_s = \frac{1}{\sqrt{-\overline{\overline{u\prime w\prime(z)}}}\left(\theta Sc^{-2/3} + 10^{-3/St_t} + V_t\right)} \tag{2A.9}$$

Here $\overline{u'w'(z)}$ is the vertical momentum flux or turbulent stress, θ describes the ratio of the viscous and drag coefficient of the leaf, St_t is the turbulent Stokes number, and V_t is the turbophoretic velocity.

$$\theta = \frac{\pi}{2}\left(\frac{c_v}{c_d}\right) \tag{2A.10}$$

$$St_t(z) = \frac{V_g\left(-\overline{u\prime w\prime(z)}\right)}{g\,\eta} \tag{2A.11}$$

$$V_t(z) = \frac{\tau_p}{1+\frac{\tau_p}{\tau(z)}}\left(\frac{\sigma_w^2(z)}{\pi\, b\, \eta}\right) \tag{2A.12}$$

$$\tau_p = \frac{d_p^2\,\rho_p\,C_c}{18\,\eta} \tag{2A.13}$$

$$\tau = \frac{K_t}{\sigma_w^2} \tag{2A.14}$$

$$K_t = \frac{-\overline{u\prime w\prime}}{\left|\frac{\delta\overline{U}}{\delta z}\right|} \tag{2A.15}$$

The variable notation follows those described above. The additional variables are τ_p which is the particle relaxation time, τ is the Lagrangian turbulent timescale, σ_w is the standard deviation of the vertical velocity, and b which is the thickness of the viscous sublayer for the vertical velocity variance. Katul et al. (2010) used b = 25 m and defined an acceptable range for the value as $5 < b < 50$ m.[4] For the calculation of the Lagrangian turbulent timescale, K_t is the eddy viscosity of the flow and is calculated using the vertical momentum flux and the mean longitudinal velocity ($\overline{U}$). These terms are either in relation to or integrated over the height of the canopy (z). It should be noted that for all equations outlined here, some of the variable notation has been changed from the original papers in order to have consistent references in this work.

Appendix 2A: References

(1) Emerson, E. W.; Hodshire, A. L.; DeBolt, H. M.; Bilsback, K. R.; Pierce, J. R.; McMeeking, G. R.; Farmer, D. K. Revisiting Particle Dry Deposition and Its Role in Radiative Effect Estimates. *PNAS* **2020**. https://doi.org/10.1073/pnas.2014761117.

(2) Zhang, L.; Gong, S.; Padro, J.; Barrie, L. A Size-Segregated Particle Dry Deposition Scheme for an Atmospheric Aerosol Module. *Atmospheric Environment* **2001**, *35* (3), 549–560. https://doi.org/10.1016/S1352-2310(00)00326-5.

(3) Slinn, W. G. N. Predictions for Particle Deposition to Vegetative Canopies. *Atmospheric Environment (1967)* **1982**, *16* (7), 1785–1794. https://doi.org/10.1016/0004-6981(82)90271-2.

(4) Katul, G. G.; Grönholm, T.; Launiainen, S.; Vesala, T. Predicting the Dry Deposition of Aerosol-Sized Particles Using Layer-Resolved Canopy and Pipe Flow Analogy Models: Role of Turbophoresis. *Journal of Geophysical Research: Atmospheres* **2010**, *115* (D12). https://doi.org/10.1029/2009JD012853.

(5) Seinfeld, J. H.; Pandis, S. N. Dry Deposition. In *Atmospheric Chemistry and Physics: From Air Pollution to Climate Change*; John Wiley & Sons, Inc.: New York, NY, 1998.

Appendix 2B: Equations and Results for Leaf Level Energy Balance and Thermophoretic Settling Velocity

Both real time data and parameters derived from other literature were used to create the leaf level energy balance equation used in this work. Real time measurements of photosynthetically active radiation (*PAR*), air temperature (T_{air}), wind speed (*WS*), and relative humidity (*RH*) were used [45]. The PAR was converted into short-wave radiation (*SWR*) using the following conversion from Thimijan and Heins (1983):

$$SWR = \left(\frac{PAR}{4.57}\right) \tag{2B.1}$$

An average stomatal conductance of 0.08 ± 0.05 mol m^{-2} s^{-1} was derived from reported literature values [76–87]. Defined parameters and constants used in the model are listed in **Tables 2B.1** and **2B.2**. The following series of equations were used to form the leaf level energy balance and predict temperature gradients between the air and collecting surface.

Saturation vapor pressure (kPa):

$$e_{sat} = a\, e^{\frac{b\, T_{air}}{(T_{air}+z)}} \tag{2B.2}$$

Water Vapor Pressure of the air (kPa):

$$e_a = e_{sat}\left(\frac{RH}{100}\right) \tag{2B.3}$$

Slope of the e_{sat}/T curve (kPa °C^{-1}):

$$s = \frac{e_{sat}\, b\, c}{(T_{air}+z)^2} \tag{2B.4}$$

Water vapor pressure deficit of the air (kPa):

$$VPD = e_{sat} - e_a \tag{2B.5}$$

Absorbed short-wave radiation (W m^{-2}):

$$SWR_{abs} = a_{SWR} \cos(i)\, SWR \quad (2B.6)$$

Incoming long-wave radiation (W m^{-2}):

$$LWR_{in} = 1.31 \left(\frac{10\, e_a}{T_{air}}\right)^{1/7} \sigma_{SB}\, (T_{air} + 273.15)^4 \quad (2B.7)$$

Isothermal outgoing long-wave radiation (W m^{-2}):

$$LWR_{out,i} = \varepsilon\, \sigma_{SB}\, (T_{air} + 273.15)^4 \quad (2B.8)$$

Isothermal net radiation (W m^{-2}):

$$R_{ni} = SWR_{abs} + LWR_{in} - LWR_{out,i} \quad (2B.9)$$

Leaf boundary-layer resistance (s m^{-1}):

$$r_{bl} = \frac{1}{\left(1.5\, g_x \frac{(WS)^{jx}}{d^{1-jx}}\right)} \quad (2B.10)$$

Radiative resistance (s m^{-1}):

$$r_r = \frac{\rho_{air}\, C_p}{4\, \varepsilon\, \sigma_{SB}\, (T_{air}+273.15)^3} \quad (2B.11)$$

Boundary-layer & radiative resistance (s m^{-1}):

$$r_{blr} = \frac{1}{(r_{bl}^{-1} + r_r^{-1})} \quad (2B.12)$$

Modified psychrometric constant (kPa K^{-1}):

$$y_m = y \left(\frac{r_{st}}{r_{blr}}\right) \quad (2B.13)$$

Leaf-to-air temperature difference (C):

$$\Delta T = \left(\frac{y_m\, R_{ni}\, r_{blr}}{\rho_{air}\, C_p - VPD}\right) \frac{1}{(s + y_m)} \quad (2B.14)$$

Leaf temperature (C):

$$T_{leaf} = T_{air} + \Delta T \quad (2B.15)$$

The resulting diel modeled gradients for the winter measurement period are shown in **Figure 2B.1**.

Thermophoretic settling velocity was calculated according to the following equations outlined by Salthammer et al. (2011) and Hinds (1999). The velocity was calculated as:

$$V_{TH} = \frac{3\,\nu\,C_c\,H\,\Delta T}{2\,\rho_{air}\,T_{air}} \quad (2B.16)$$

using the viscosity of air (ν), Cunningham slip correction (C_c), temperature gradient between the collecting surface and air (ΔT), density of air (ρ_{air}), and temperature of air (T_{air}). The H term was separately calculated by:

$$H = \frac{1}{1+6\left(\frac{\lambda}{D_a}\right)} \times \frac{\left(\frac{k_a}{k_p}\right)+4.4\left(\frac{\lambda}{D_a}\right)}{1+\,2\left(\frac{k_a}{k_p}\right)+8.8\left(\frac{\lambda}{D_a}\right)} \quad (2B.17)$$

using the mean free path (λ), aerodynamic diameter of the particle (D_a), the thermal conductivity of air (k_a), and the thermal conductivity of the particles (k_p). The behavior of the thermophoretic settling velocity as the magnitude of the temperature gradient changes and the thermal conductivity of the particles change is shown in **Figure 2B.2**, along with the results of its integration into the Emerson et al. (2020) model.

Table 2B.1: Leaf level parameters defined for the energy balance.

Parameter	Units	Value
Angle from horizontal (*i*)	degrees	0 – 90
Absorptance to SWR ($\boldsymbol{a_{SWR}}$)	%	0.4 – 0.6
Emissivity (ε)	none	0.96 – 0.98
Characteristic dimension (*d*)	mm	1 *
Shape factor of the leaf (shape)	none	2 **
Stomatal resistance ($\boldsymbol{r_{st}}$)	s m^{-1}	11.76***

*Defined for a pine needle
**Shape = 2 indicates a cylindrical shape
***Value obtained through synthesis of various reported values in the literature for ponderosa pines under normal, unstressed conditions.

Table 2B.2: Constants used in the formulation of the leaf level energy balance, defined in the order in which they appear in Table S3.

Constant	Units	Value
Coefficient in e_{sat} equation (*a*)	kPa	0.61121
Coefficient in e_{sat} equation (*b*)	none	17.502
Coefficient in e_{sat} equation (*z*)	°C	240.97
Stefan-Boltzman constant (σ_{SB})	W m^{-2} K^{-4}	5.67 x 10^{-8}
Coefficient in r_{bl} equation for a flat leaf shape (g_{flat})	m	0.00662
Coefficient in r_{bl} equation for a cylinder leaf shape (g_{cyl})	m	0.00403
Coefficient in r_{bl} equation for a sphere leaf shape (g_{sph})	m	0.00571
Coefficient in r_{bl} equation for a flat leaf shape (j_{flat})	none	0.5
Coefficient in r_{bl} equation for a cylinder leaf shape (j_{cyl})	none	0.6
Coefficient in r_{bl} equation for a sphere leaf shape (j_{sph})	none	0.6
Density of air (ρ_{air})	kg m^{-3}	1.292
Heat capacity of air (C_p)	J kg^{-1} K^{-1}	1010
Psychrometric constant (y)	kPa K^{-1}	0.066
Latent heat of vaporization (L)	J g^{-1}	2500

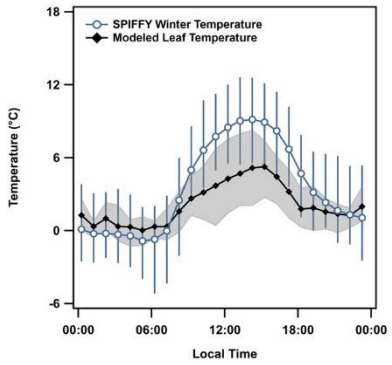

Figure 2B.1: Diel average measured air temperature and modeled leaf temperature. With the interquartile range for the measured data shown in bars and the interquartile range for the modeled data shown in shading

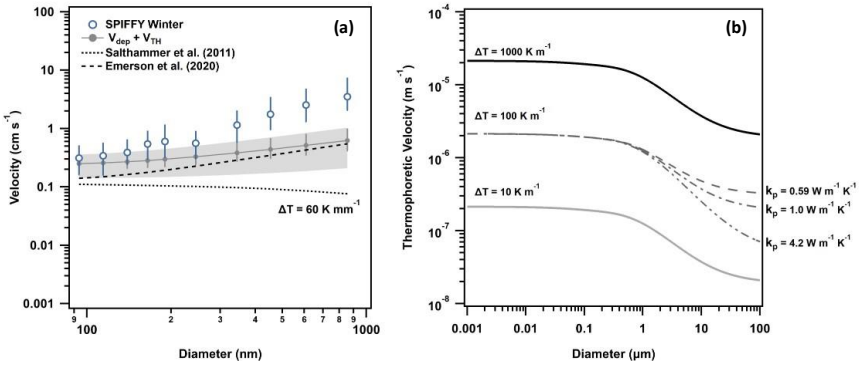

Figure 2B.2: (**a**) Integration of the thermophoretic velocity into the Emerson et al. (2020) model. The total modeled velocity is shown in grey with shading representing the standard deviation and bars representing the interquartile range. (**b**) Thermophoretic settling velocity as a function of particle diameter for three different gradient values: ΔT = 10, 100, and 1000 K m^{-1}. Additionally, the velocity at ΔT = 100 K m^{-1} was varied by particle thermal conductivity and results are shown for k_p = 0.59, 1.0, and 4.2 W m^{-1} K^{-1}.

Appendix 2B: References

(1) Frank, J. M.; Fornwalt, P. J.; Asherin, L. A.; Alton, S. K. *Manitou Experimental Forest Hourly Meteorology Data*, 3rd ed.; Forest Service Research Data Archive: Fort Collins, CO, 2021.

(2) Thimijan, R. W.; Heins, R. D. Photometric, Radiometric, and Quantum Light Units of Measure: A Review of Procedures for Interconversion. *HortScience* **1983**, *18* (6), 818–822.

(3) Harley, P.; Eller, A.; Guenther, A.; Monson, R. K. Observations and Models of Emissions of Volatile Terpenoid Compounds from Needles of Ponderosa Pine Trees Growing in Situ: Control by Light, Temperature and Stomatal Conductance. *Oecologia* **2014**, *176* (1), 35–55. https://doi.org/10.1007/s00442-014-3008-5.

(4) Calder, W. J.; Lifferth, G.; Moritz, M. A.; Clair, S. B. S. Physiological Effects of Smoke Exposure on Deciduous and Conifer Tree Species. *International Journal of Forestry Research* **2010**, *2010*, e438930. https://doi.org/10.1155/2010/438930.

(5) McDowell, N. G.; White, S.; Pockman, W. T. Transpiration and Stomatal Conductance across a Steep Climate Gradient in the Southern Rocky Mountains. *Ecohydrology* **2008**, *1* (3), 193–204. https://doi.org/10.1002/eco.20.

(6) Sala, A.; Peters, G. D.; McIntyre, L. R.; Harrington, M. G. Physiological Responses of Ponderosa Pine in Western Montana to Thinning, Prescribed Fire and Burning Season. *Tree Physiology* **2005**, *25* (3), 339–348. https://doi.org/10.1093/treephys/25.3.339.

(7) Domec, J.-C.; Warren, J. M.; Meinzer, F. C.; Brooks, J. R.; Coulombe, R. Native Root Xylem Embolism and Stomatal Closure in Stands of Douglas-Fir and Ponderosa Pine: Mitigation by Hydraulic Redistribution. *Oecologia* **2004**, *141* (1), 7–16. https://doi.org/10.1007/s00442-004-1621-4.

(8) Skov, K. R.; Kolb, T. E.; Wallin, K. F. Tree Size and Drought Affect Ponderosa Pine Physiological Response to Thinning and Burning Treatments. *Forest Science* **2004**, *50* (1), 81–91. https://doi.org/10.1093/forestscience/50.1.81.

(9) Hubbard, R. M.; Bond, B. J.; Ryan, M. G. Evidence That Hydraulic Conductance Limits Photosynthesis in Old Pinus Ponderosa Trees. *Tree Physiol* **1999**, *19* (3), 165–172. https://doi.org/10.1093/treephys/19.3.165.

(10) Hubbard, R. M.; Ryan, M. G.; Stiller, V.; Sperry, J. S. Stomatal Conductance and Photosynthesis Vary Linearly with Plant Hydraulic Conductance in Ponderosa Pine. *Plant, Cell & Environment* **2001**, *24* (1), 113–121. https://doi.org/10.1046/j.1365-3040.2001.00660.x.

(11) Panek, J. A.; Goldstein, A. H. Response of Stomatal Conductance to Drought in Ponderosa Pine: Implications for Carbon and Ozone Uptake. *Tree Physiology* **2001**, *21* (5), 337–344. https://doi.org/10.1093/treephys/21.5.337.

(12) Ryan, M. G.; Bond, B. J.; Law, B. E.; Hubbard, R. M.; Woodruff, D.; Cienciala, E.; Kucera, J. Transpiration and Whole-Tree Conductance in Ponderosa Pine Trees of Different Heights. *Oecologia* **2000**, *124* (4), 553–560. https://doi.org/10.1007/s004420000403.

(13) Zhang, J. W.; Feng, Z.; Cregg, B. M.; Schumann, C. M. Carbon Isotopic Composition, Gas Exchange, and Growth of Three Populations of Ponderosa Pine Differing in Drought Tolerance. *Tree Physiology* **1997**, *17* (7), 461–466. https://doi.org/10.1093/treephys/17.7.461.

(14) Monson, R. K.; Grant, M. C. Experimental Studies of Ponderosa Pine. Iii. Differences in Photosynthesis, Stomatal Conductance, and Water-Use Efficiency Between Two Genetic Lines. *American Journal of Botany* **1989**, *76* (7), 1041–1047. https://doi.org/10.1002/j.1537-2197.1989.tb15085.x.

(15) Salthammer, T.; Fauck, C.; Schripp, T.; Meinlschmidt, P.; Willenborg, S.; Moriske, H.-J. Effect of Particle Concentration and Semi-Volatile Organic Compounds on the Phenomenon of 'Black Magic Dust' in Dwellings. *Building and Environment* **2011**, *46* (10), 1880–1890. https://doi.org/10.1016/j.buildenv.2011.03.008.

(16) Hinds, W. C. *Aerosol Technology: Properties, Behavior, and Measurement of Airborne Particles*, 2nd ed.; John Wiley & Sons, Inc.: New York, NY, 1999.
(17) Emerson, E. W.; Hodshire, A. L.; DeBolt, H. M.; Bilsback, K. R.; Pierce, J. R.; McMeeking, G. R.; Farmer, D. K. Revisiting Particle Dry Deposition and Its Role in Radiative Effect Estimates. *PNAS* **2020**. https://doi.org/10.1073/pnas.2014761117.

Appendix 2S: Supplemental Information for Chapter 2

Site Set-up and Meteorological Parameters During the Campaign Periods

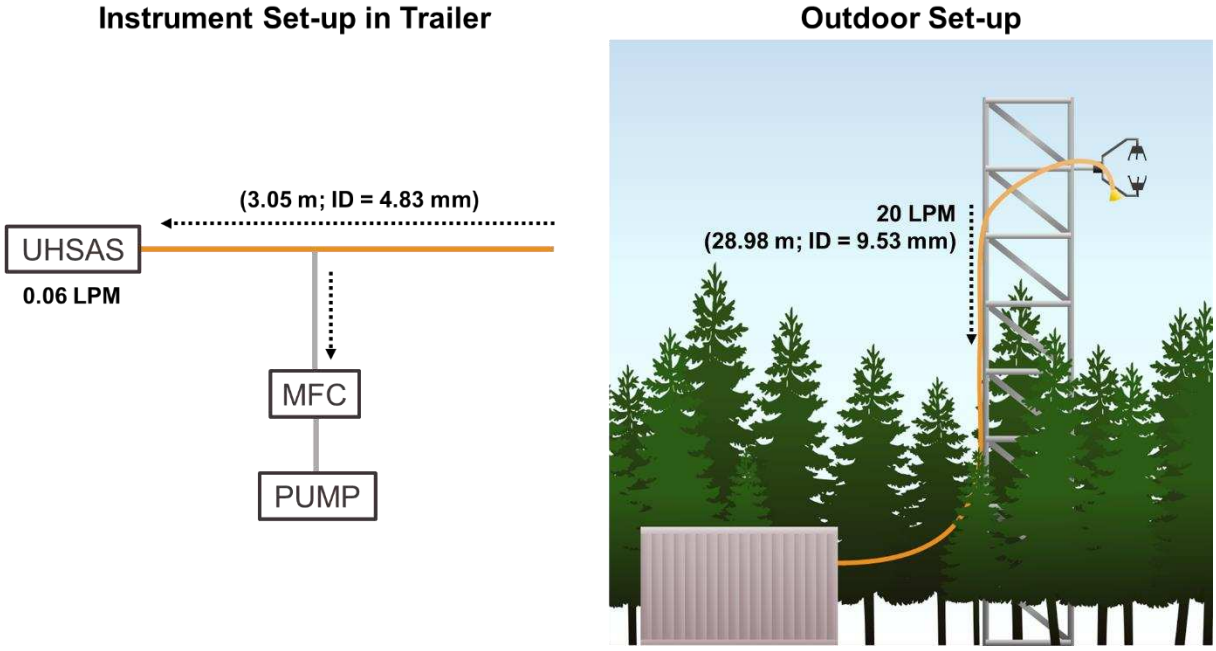

Figure 2S.1: Schematic of the instrument set up at the Manitou Experimental Forest Observatory.

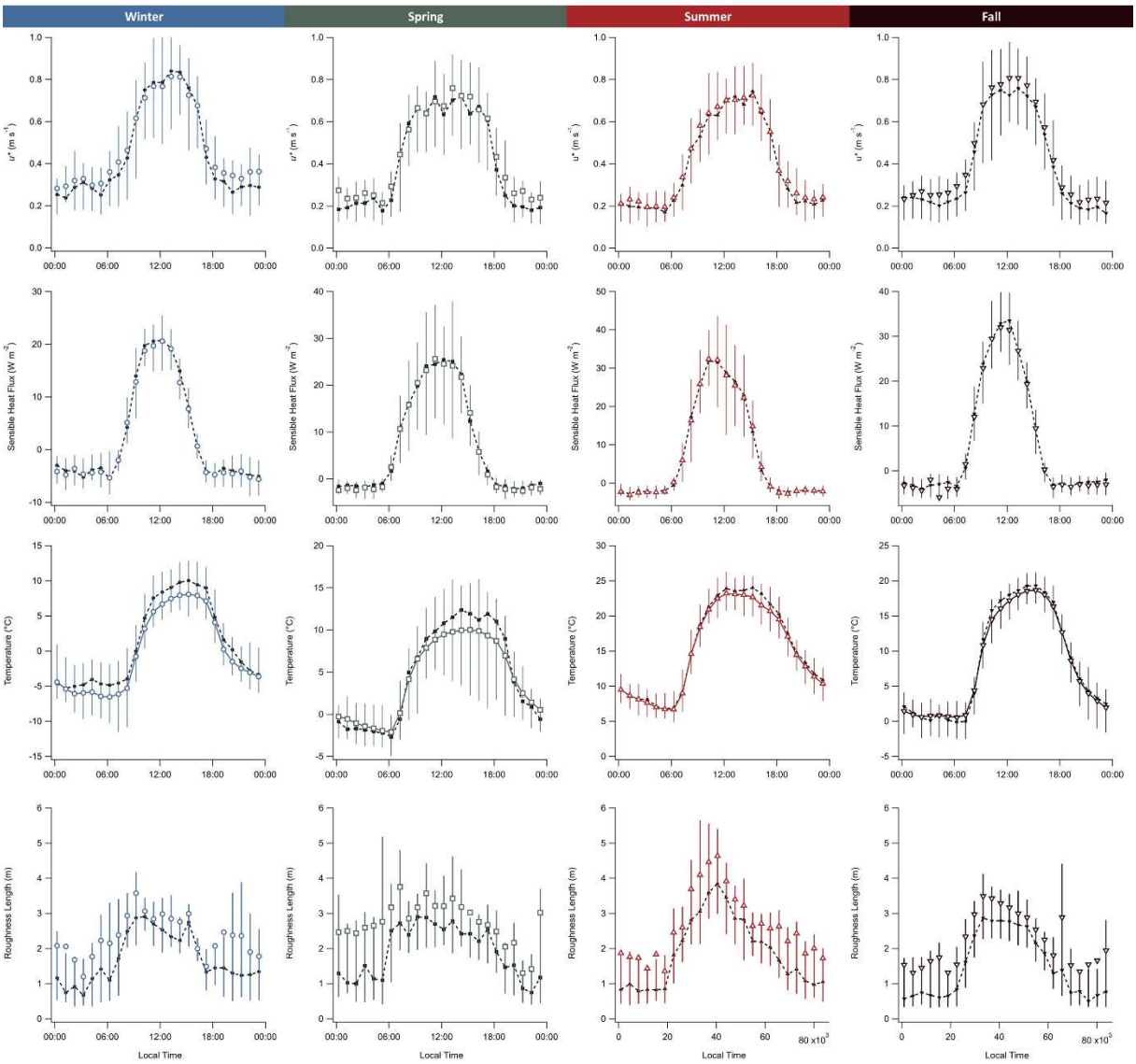

Figure 2S.2: Average diel cycle for friction velocity (u^*), sensible heat flux (H), air temperature, and roughness length of each season. Open points are means, while the error bars represent the 25th and 75th percentiles, and the solid points represent the medians.

Results from eddy-covariance analysis and derived relationships between model variables

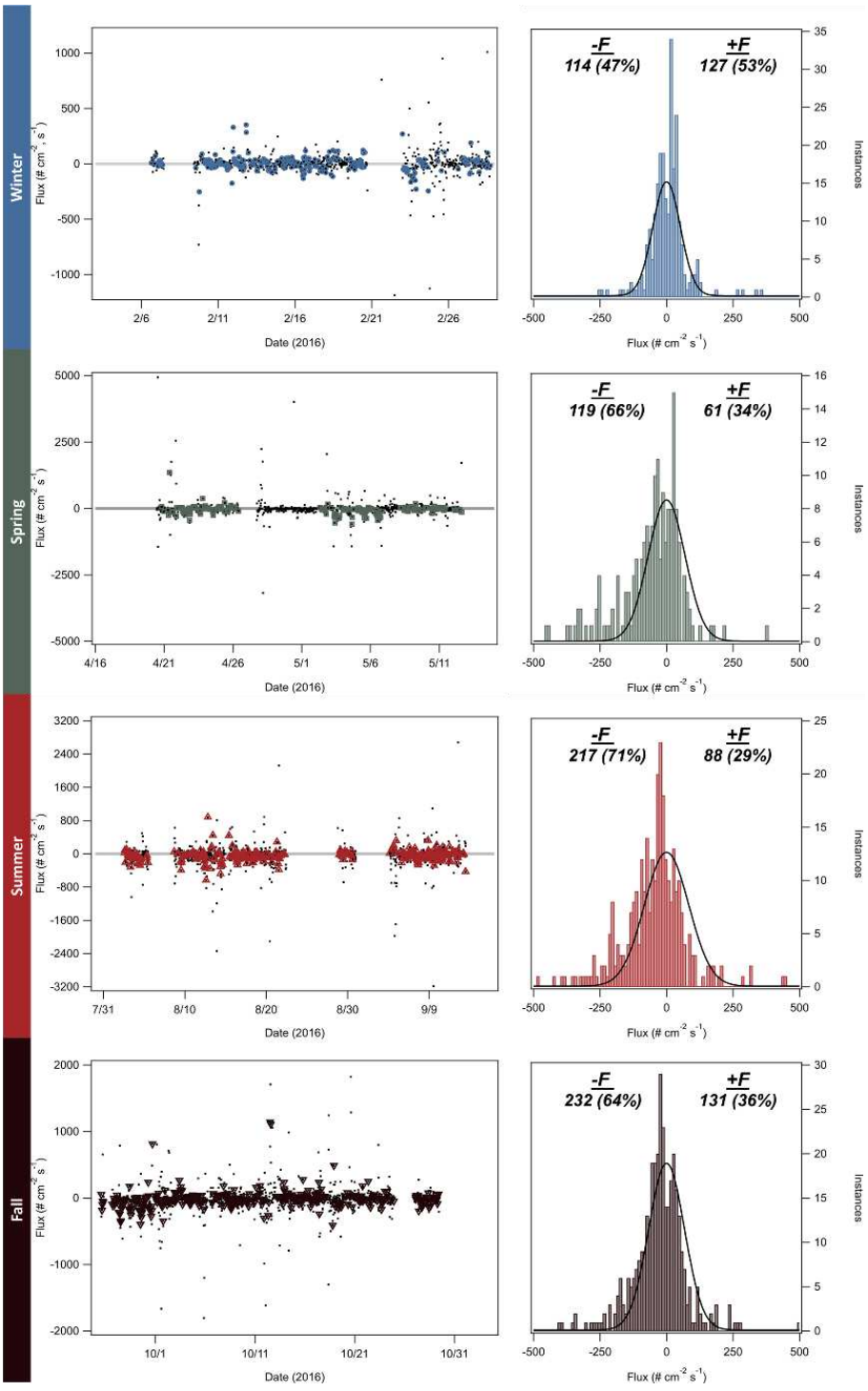

Figure 2S.3: Graphical results of flux QC filtering (left) along with a histogram of flux instances (right). In the timeseries of QC filtering the black points are all available flux periods and the colored markers are the periods that passed all QC parameters. The histogram for each season shows visually unequal distributions of flux instances about zero (number of positive and negative fluxes are also provided). In addition to visual investigation, a Kolmogorov-Smirnov test on the data from all seasons resulted in the rejection of the hypothesis that the data was taken from a normal distribution. Indicating that the positive and negative fluxes can be treated separately as source emissions and deposition.

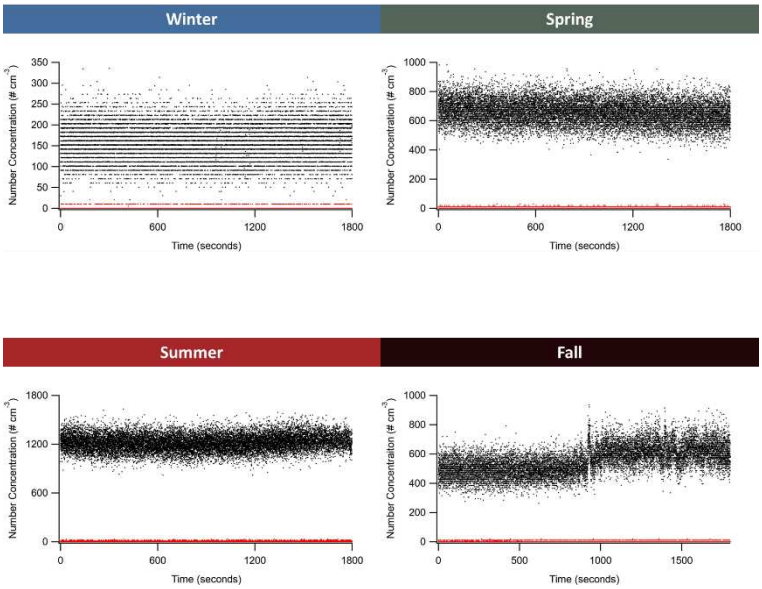

Figure 2S.4: Calculation of the SNR for each seasonal measurement period. With the black data representing the 30 minutes of data before a system filter and the red data representing the data from the adjacent 30-minute filtering period.

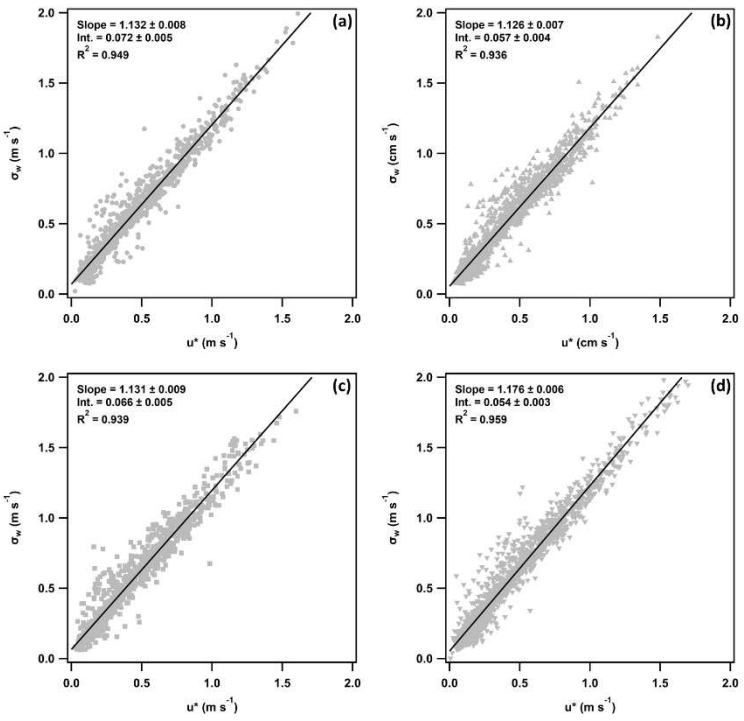

Figure 2S.5: Relationship between the standard deviation of the vertical velocity (σ_w) and friction velocity (u*) for the (a) winter, (b) spring, (c) summer, and (d) fall.

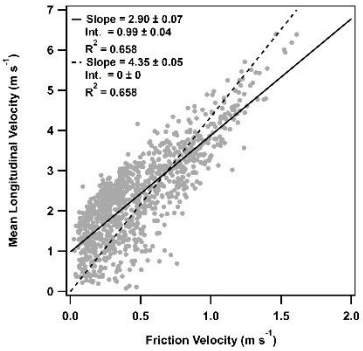

Figure 2S.6: Relationship of the mean longitudinal velocity ($\overline{U}$) to the friction velocity (u*) for the winter SPiFFY data.

Seasonal trends in flux, exchange velocity, and concentration and variation in particle size distributions

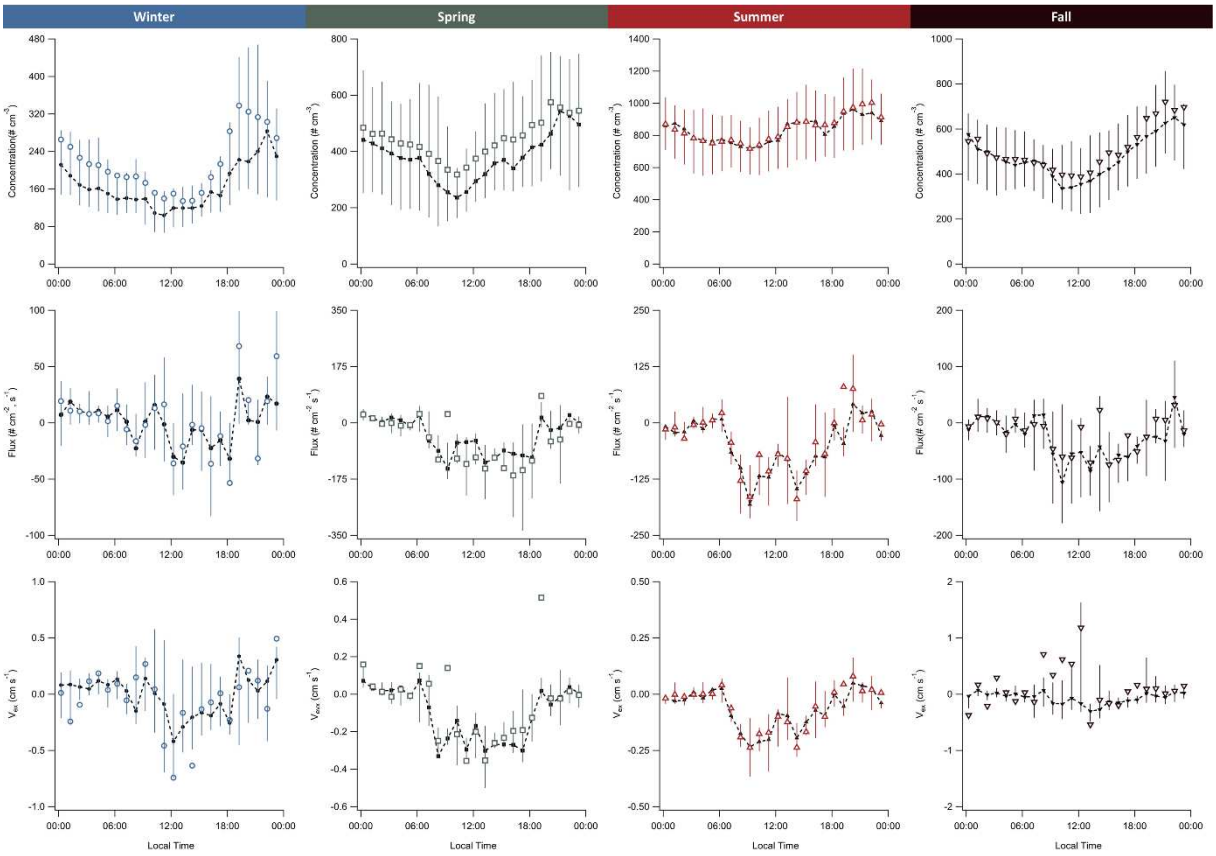

Figure 2S.7: Diel trends of number concentration, flux, and exchange velocity (V_{ex}) for each season. Open points are means, while the error bars represent the 25th and 75th percentiles, and the solid points represent the medians.

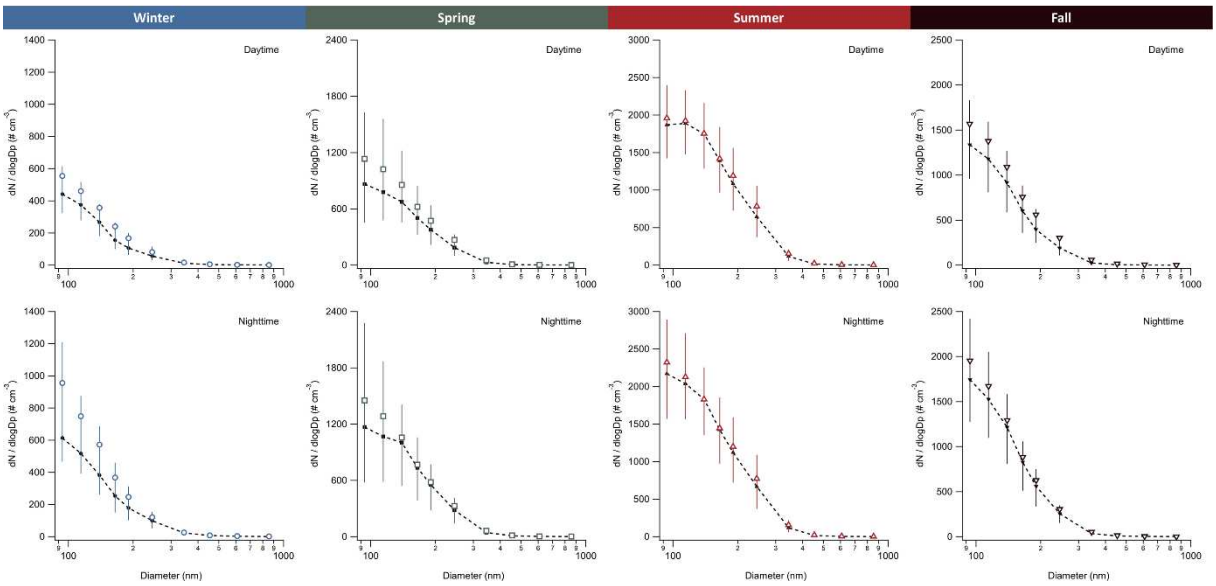

Figure 2S.8: Daytime (top row) and nighttime (bottom row) particle size distributions for each seasonal period. These periods were defined using average reported sunrise and sunset times. Open points are means, while the error bars represent the 25th and 75th percentiles, and the solid points represent the medians.

Table 2S.9: Count median diameters (CMD), as well as surface median diameters (SMD), volume median diameters (VMD), and the geometric standard deviation (GSD) for the daytime and nighttime particle distributions of each season.

Diameter Type	Period	Winter	Spring	Summer	Fall
CMD	Daytime	129 ± 8	140 ± 20	140 ± 10	130 ± 10
	Nighttime	129 ± 7	140 ± 20	140 ± 10	128 ± 7
SMD	Daytime	160 ± 20	170 ± 30	180 ± 20	160 ± 20
	Nighttime	160 ± 20	170 ± 30	180 ± 20	160 ± 10
VMD	Daytime	180 ± 20	190 ± 30	200 ± 30	170 ± 20
	Nighttime	180 ± 20	200 ± 40	200 ± 30	170 ± 20
GSD	Daytime	1.38 ± 0.04	1.38 ± 0.04	1.42 ± 0.05	1.37 ± 0.04
	Nighttime	1.39 ± 0.05	1.39 ± 0.05	1.42 ± 0.06	1.37 ± 0.04

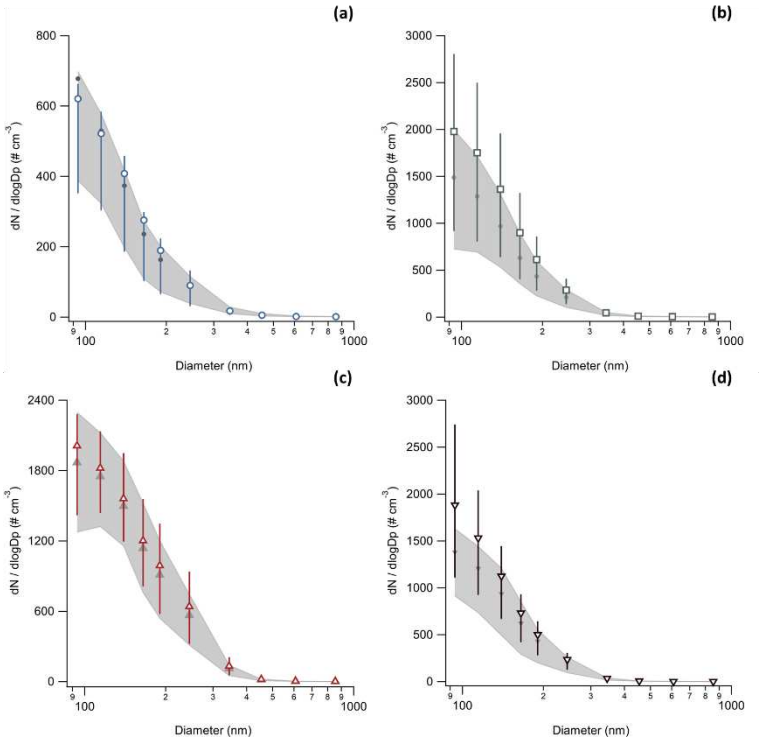

Figure 2S.10: Comparison of particle size-distributions between periods of positive and negative flux measurements for the (**a**) winter, (**b**) spring, (**c**) summer, and (**d**) fall. In each figure the grey points and shading represent the mean concentration and the 25th and 75th percentiles for periods where a positive flux was observed, while the colored points and lines represent the mean concentration and the 25th and 75th percentiles for periods where a negative flux was observed.

Table 2S.11: Count median diameters (CMD), surface median diameters (SMD), volume median diameters (VMD), and the geometric standard deviation (GSD) for particle distributions during positive and negative particle flux measurement periods.

Diameter Type	Flux Type	Winter	Spring	Summer	Fall
CMD	+ Flux	128 ± 8	129 ± 6	140 ± 10	129 ± 8
	- Flux	129 ± 9	129 ± 4	140 ± 10	128 ± 7
SMD	+ Flux	160 ± 20	160 ± 10	180 ± 20	160 ± 20
	- Flux	160 ± 20	157 ± 9	180 ± 20	160 ± 10
VMD	+ Flux	180 ± 20	180 ± 10	200 ± 30	180 ± 20
	- Flux	180 ± 20	170 ± 10	200 ± 30	170 ± 20
GSD	+ Flux	1.38 ± 0.05	1.37 ± 0.03	1.40 ± 0.04	1.37 ± 0.04
	- Flux	1.38 ± 0.04	1.37 ± 0.03	1.40 ± 0.04	1.36 ± 0.03

Section S4: Seasonal trends in deposition velocity and model comparisons

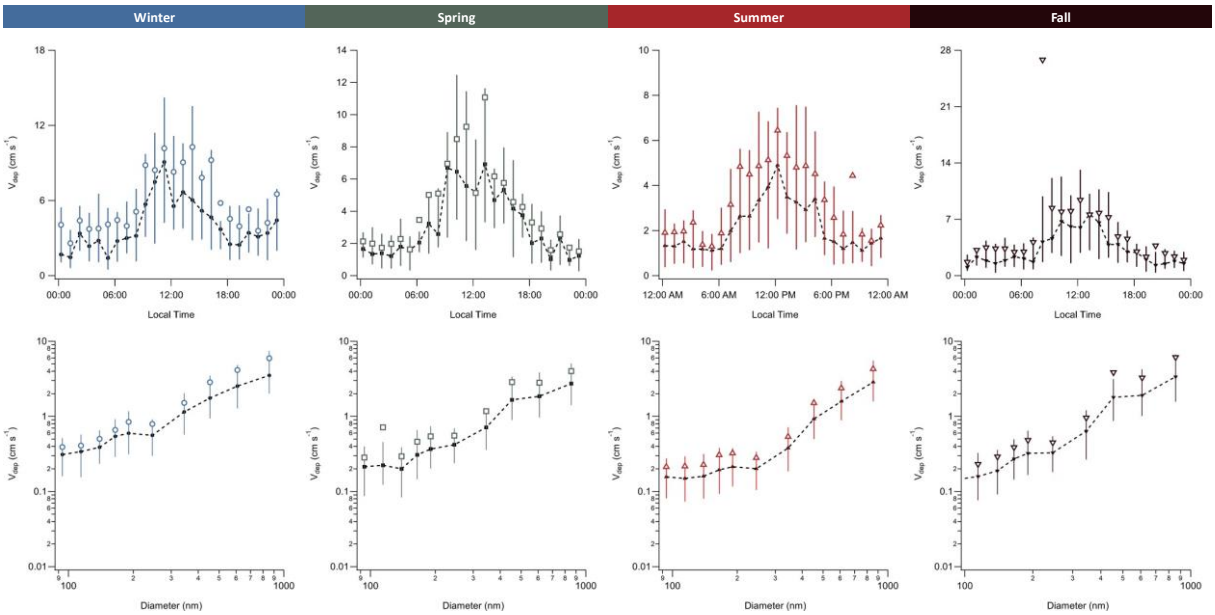

Figure 2S.12: Seasonal total (top row) size-dependent (bottom row) deposition velocities for the winter, spring, summer, and fall. Open points are means, while the error bars represent the 25th and 75th percentiles, and the solid points represent the medians.

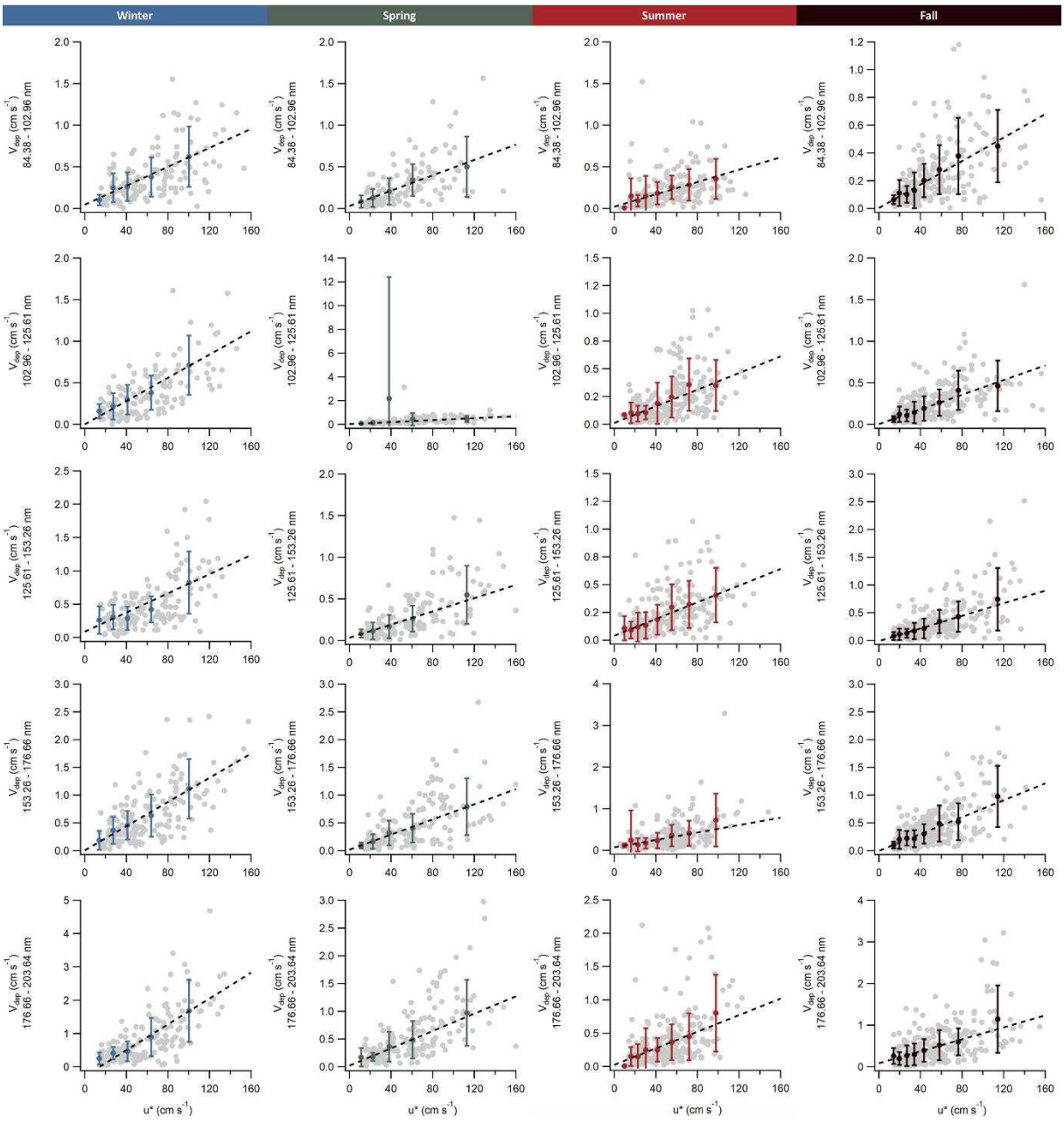
Winter
Spring
Summer
Fall
V_{dep} (cm s^{-1}) 84.38 - 102.96 nm
V_{dep} (cm s^{-1}) 102.96 - 125.61 nm
V_{dep} (cm s^{-1}) 125.61 - 153.26 nm
V_{dep} (cm s^{-1}) 153.26 - 176.66 nm
V_{dep} (cm s^{-1}) 176.66 - 203.64 nm
u* (cm s^{-1})

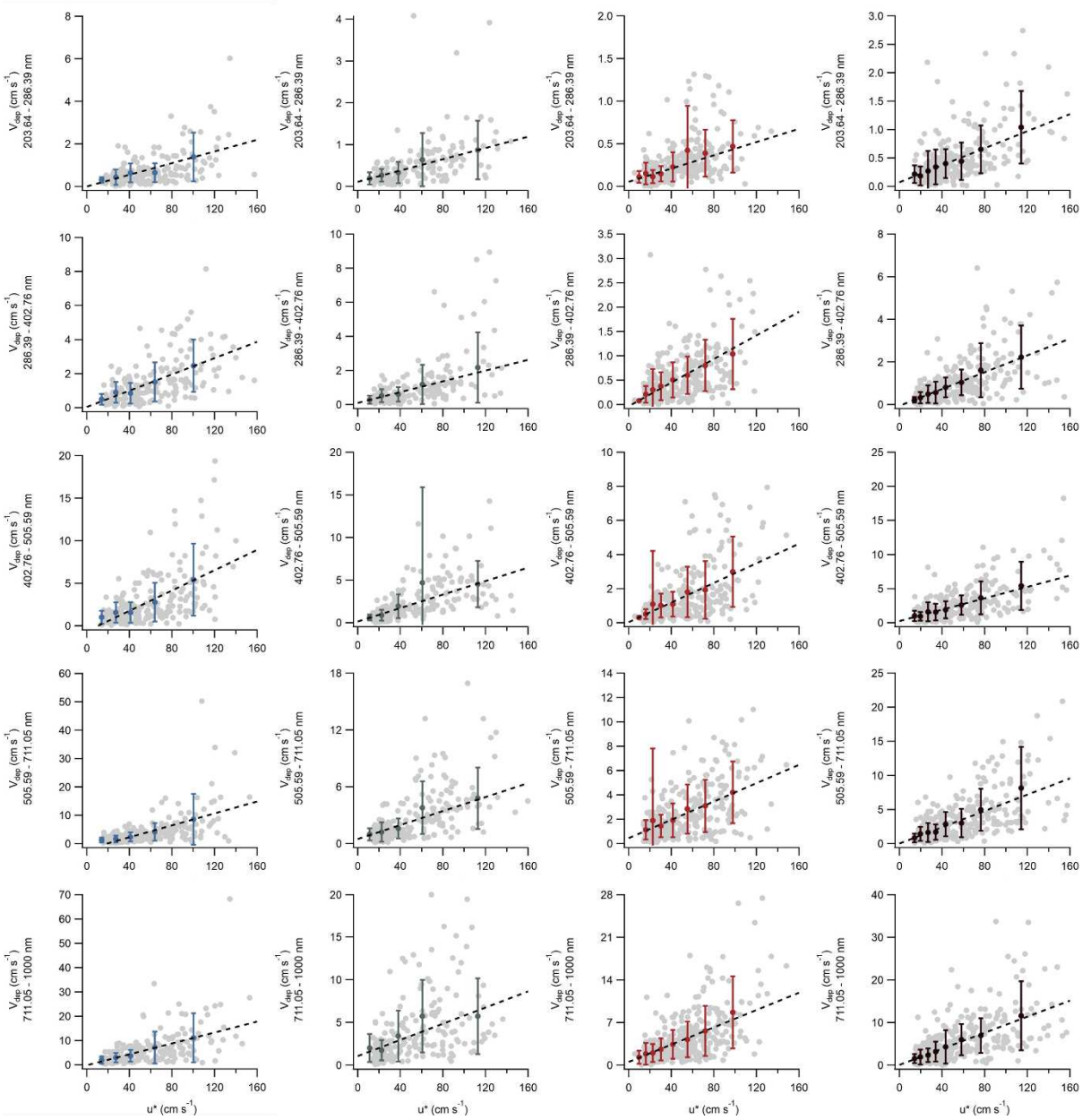

Figure 2S.13: Seasonal size-dependent deposition velocities compared to friction velocity (u^*) for the winter, spring, summer, and fall. Grey points represent raw data and colored points represent data binned by u^*, with each point representing 200 measurement periods (periods removed during quality control are included in count but not comparison).

Table 2S.14: Linear fits to the size-dependent deposition velocities versus friction velocity (u^*) for the winter, spring, summer, and fall.

Size range (nm)		Winter	Spring	Summer	Fall
84.38 – 102.96	Slope :	0.01 ± 0.07	0.005 ± 0.003	0.004 ± 0.002	0.004 ± 0.002
	Int. :	1 ± 6	0.03 ± 0.08	0.1 ± 0.1	0.01 ± 0.05
	R^2 :	0.693	0.861	0.888	0.799
102.96 – 125.61	Slope :	0.01 ± 0.07	0.004 ± 0.002	0.004 ± 0.002	0.004 ± 0.002
	Int. :	-1 ± 6	0.03 ± 0.06	0.01 ± 0.08	0.01 ± 0.05
	R^2 :	0.836	0.042	0.826	0.802
125.61 – 153.26	Slope :	0.01 ± 0.04	0.004 ± 0.002	0.004 ± 0.002	0.006 ± 0.003
	Int. :	1 ± 4	0.03 ± 0.06	0.04 ± 0.07	-0.01 ± 0.08
	R^2 :	0.827	0.688	0.856	0.637
153.26 – 176.66	Slope :	0.01 ± 0.04	0.007 ± 0.003	0.004 ± 0.003	0.008 ± 0.003
	Int. :	1 ± 3	0.02 ± 0.07	0.07 ± 0.06	-0.01 ± 0.08
	R^2 :	0.862	0.804	0.496	0.675
176.66 – 203.64	Slope :	0.02 ± 0.04	0.008 ± 0.005	0.006 ± 0.004	0.007 ± 0.004
	Int. :	-1 ± 3	0.1 ± 0.1	0.1 ± 0.2	0.1 ± 0.2
	R^2 :	0.798	0.819	0.633	0.578
203.64 – 286.39	Slope :	0.01 ± 0.03	0.007 ± 0.006	0.004 ± 0.003	0.007 ± 0.004
	Int. :	-1 ± 2	0.1 ± 0.2	0.05 ± 0.07	0.1 ± 0.2
	R^2 :	0.720	0.786	0.628	0.748
286.39 – 402.76	Slope :	0.02 ± 0.02	0.02 ± 0.01	0.012 ± 0.004	0.020 ± 0.008
	Int. :	1 ± 1	0.1 ± 0.3	-0.04 ± 0.04	-0.1 ± 0.2
	R^2 :	0.774	0.580	0.936	0.707
402.76 – 505.59	Slope :	0.060 ± 0.008	0.04 ± 0.02	0.03 ± 0.01	0.04 ± 0.02
	Int. :	-0.6 ± 0.7	0.1 ± 0.5	0.1 ± 0.2	0.2 ± 0.7
	R^2 :	0.841	0.518	0.759	0.722
505.59 – 711.05	Slope :	0.105 ± 0.006	0.04 ± 0.03	0.04 ± 0.02	0.06 ± 0.03
	Int. :	-2.0 ± 0.5	0.5 ± 0.7	1 ± 1	-0.1 ± 0.8
	R^2 :	0.833	0.720	0.839	0.579
711.05 - 1000	Slope :	0.112 ± 0.004	0.05 ± 0.04	0.07 ± 0.04	0.09 ± 0.04
	Int. :	-0.2 ± 0.3	1 ± 1	1 ± 1	1 ± 1
	R^2 :	0.673	0.775	0.696	0.728

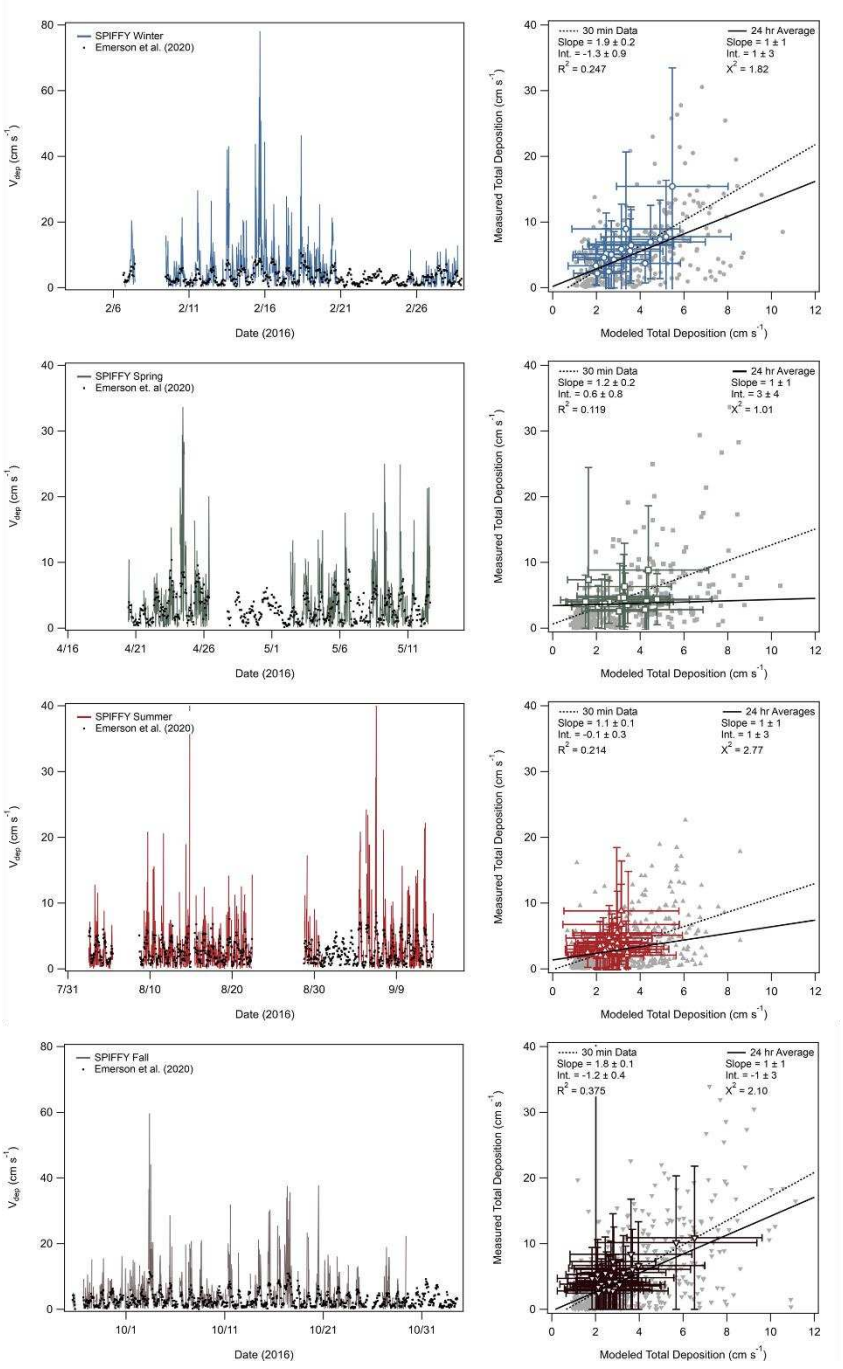

Figure 2S.15: Comparison of total measured deposition velocity versus the output of the Emerson et al. (2020) model for total deposition. Timeseries comparisons are shown on the left while linear fits of the measured versus modeled deposition velocity are presented on the right for the 30-minute raw data and 24-hour averages. The 24-hour averages obscure the comparison between the measured and modeled values.

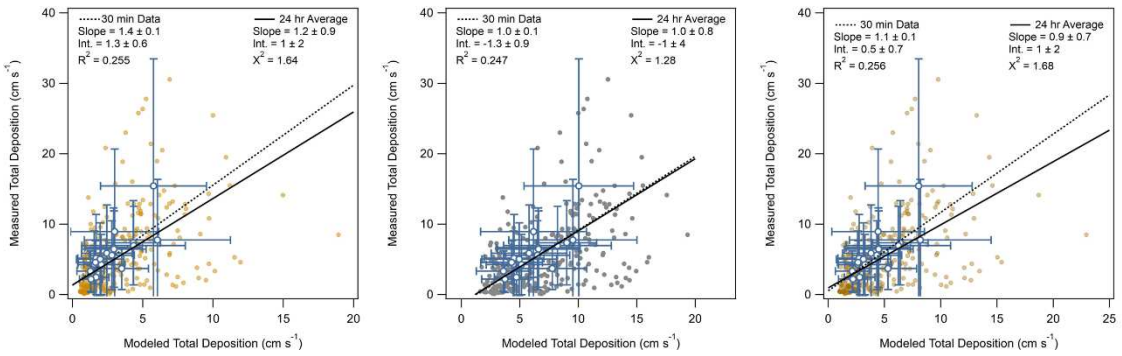

Figure 2S.16: Comparison of total measured deposition velocity versus (left) the output of the Emerson et al. (2020) model with the turbophoresis term from form Katul et al. (2010) incorporated and (middle) the output of the Emerson et al. (2020) model with an altered interception term increasing its influence during the wintertime. The comparison of total measured deposition velocity versus (right) the output of the Emerson et al. (2020) model with the turbophoresis term from form Katul et al. (2010) and the interception term scaled up is also shown.

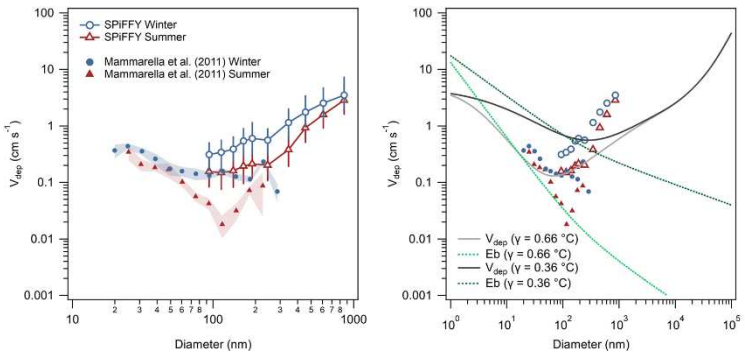

Figure 2S.17: Comparison of SPiFFY winter and summer data to the seasonal data from Mammarella et al. (2011) (left), and the incorporation of the suppressed γ value measured by Mammarella et al. (2011) into the Emerson et al. (2020) model (right). This change significantly changes the predicted size-dependent deposition velocity. The shift in the minimum created by the change is not supported by other deposition velocity measurements and does nothing to improve model and measurement agreements in the SPiFFY data.

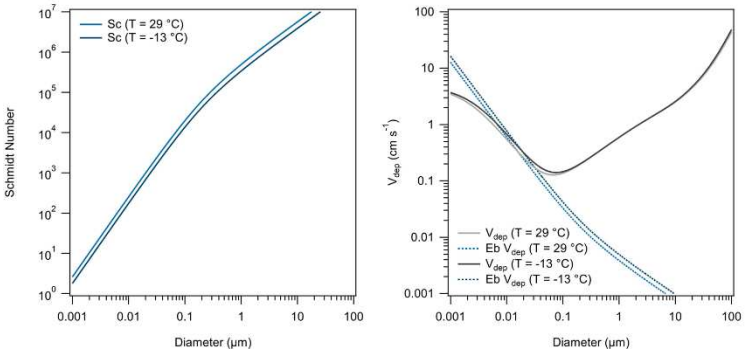

Figure 2S.18: Temperature dependence of the Schmidt number (left) and its effect on the Brownian collection efficiency and deposition velocity (right). These temperatures span the range of the highest and lowest reported temperatures during the SPiFFY campaign.

Appendix 2S: References

Emerson, E. W., Hodshire, A. L., DeBolt, H. M., Bilsback, K. R., Pierce, J. R., McMeeking, G. R., and Farmer, D. K.: Revisiting particle dry deposition and its role in radiative effect estimates, PNAS, https://doi.org/10.1073/pnas.2014761117, 2020.

Katul, G. G., Grönholm, T., Launiainen, S., and Vesala, T.: Predicting the dry deposition of aerosol-sized particles using layer-resolved canopy and pipe flow analogy models: Role of turbophoresis, 115, https://doi.org/10.1029/2009JD012853, 2010.

Mammarella, I., Rannik, Ü., Aalto, P., Keronen, P., Vesala, T., and Kulmala, M.: Long-term aerosol particle flux observations. Part II: Particle size statistics and deposition velocities, Atmospheric Environment, 45, 3794–3805, https://doi.org/10.1016/j.atmosenv.2011.04.022, 2011.

Appendix 3S: Supplemental Information for Chapter 3

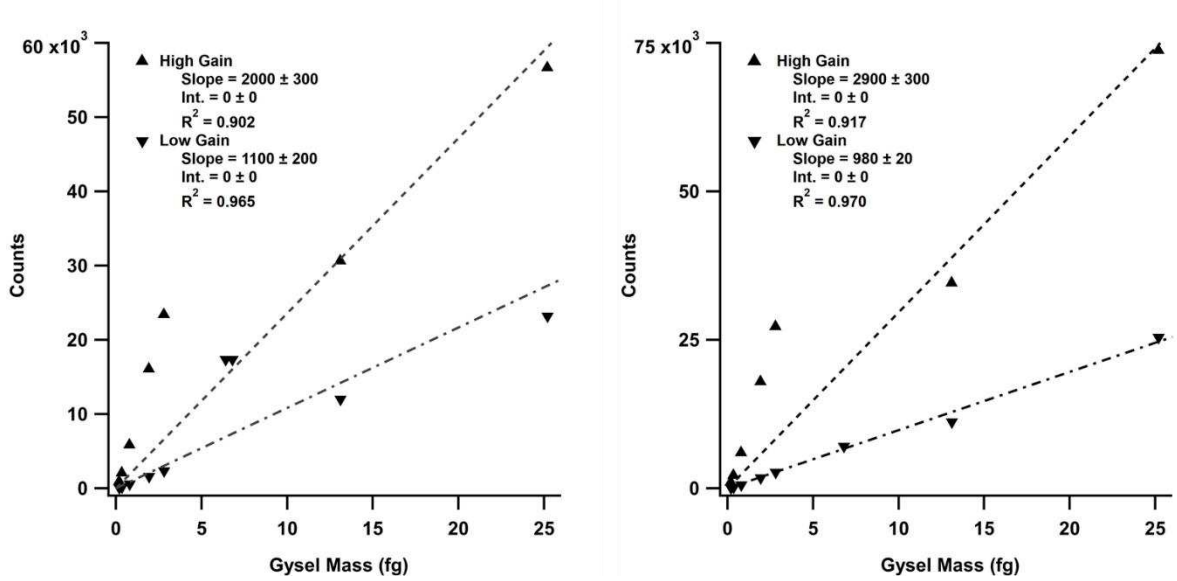

Figure 3S.1: Results of high and low gain calibrations for black carbon on the SP2 done on 14 September (left) and 27 October (right) 2021.

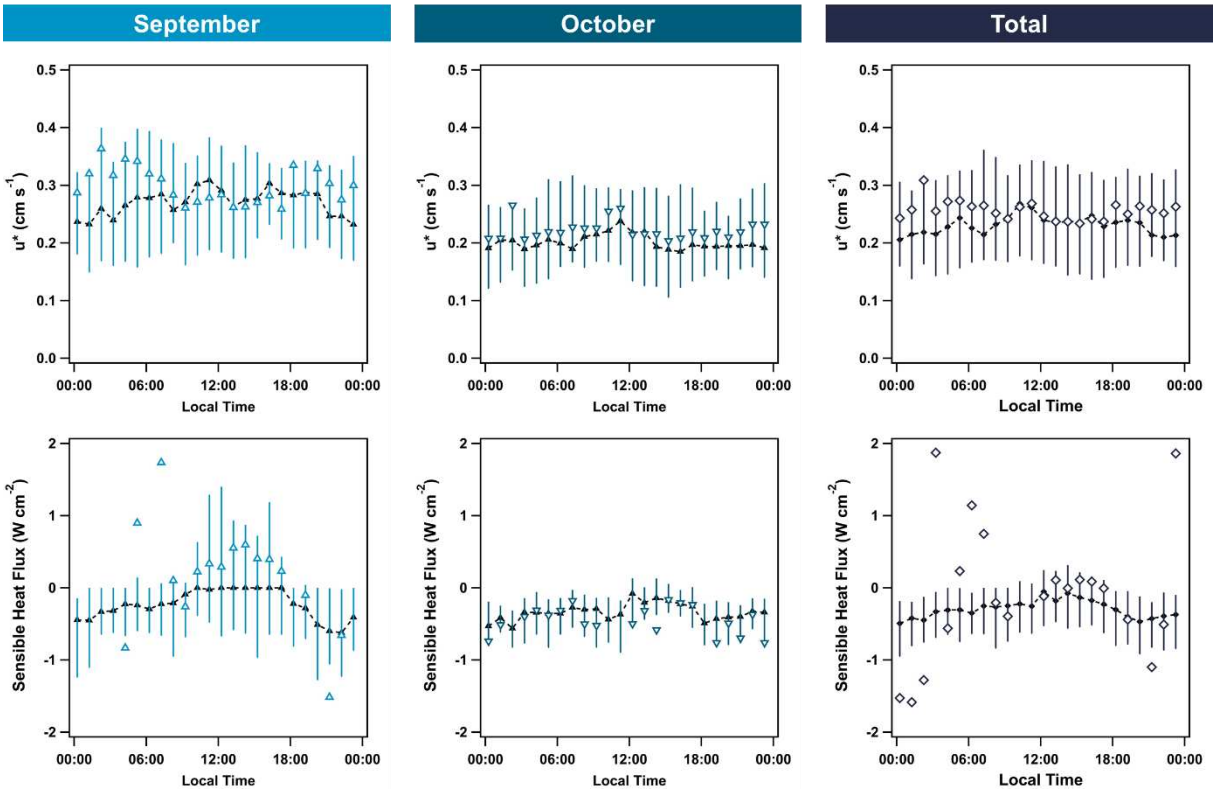

Figure 3S.2: Diel cycles of friction velocity (u*) and sensible heat flux for September (left), October (middle), and the total campaign (right). Medians are in black, means are open-colored markers, and the bars represent the interquartile range.

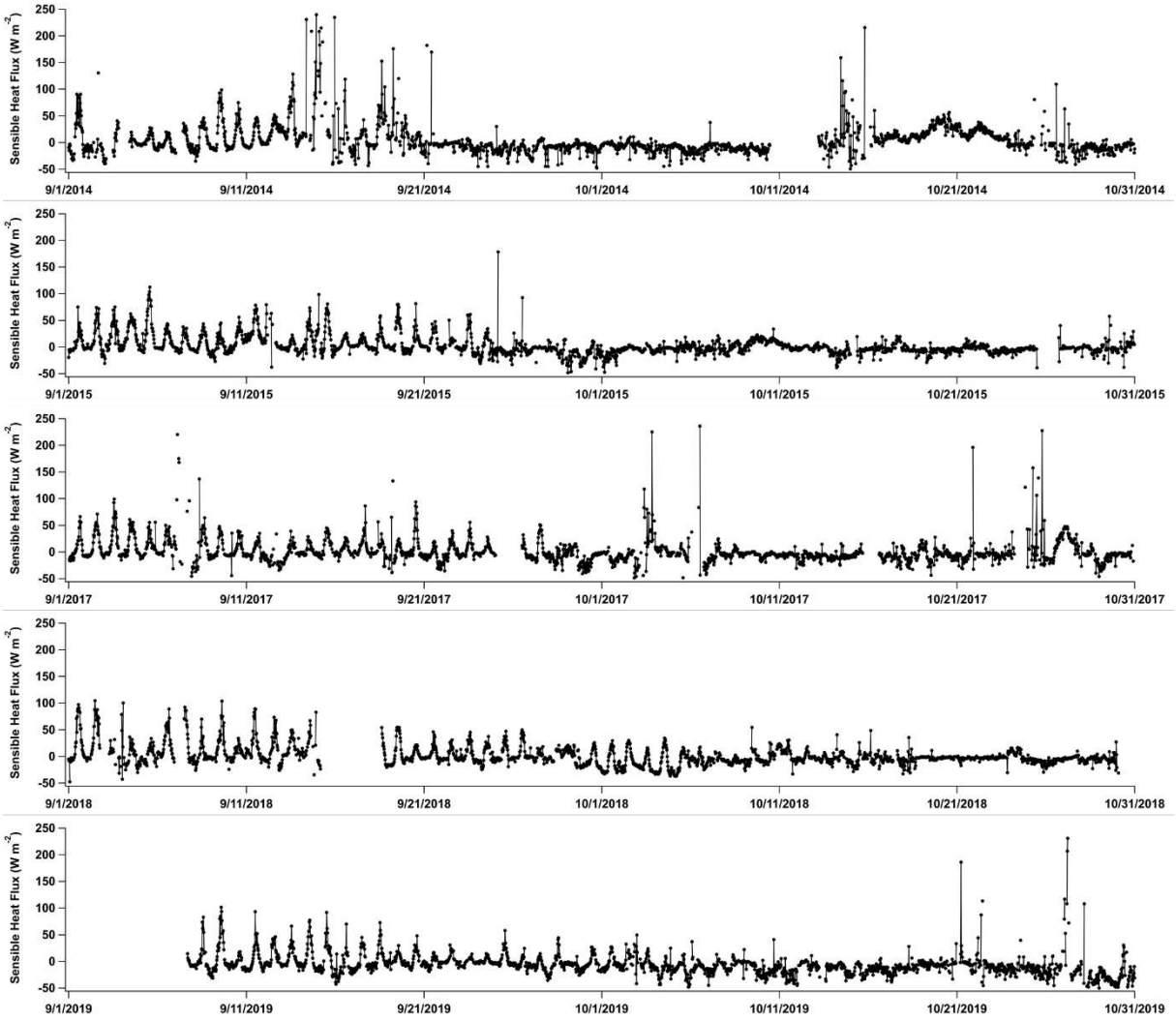

Figure 3S.3: Ameriflux sensible heat flux reported for September and October of 2014-2019 showing a break down in the diel trend during these months that can explain the trends we see in the data from this work.